UNIVERSITY OF SOUTHAMPTON

Faculty of Engineering and the Environment

School of Aeronautics, Astronautics and Computational Engineering

Numerical Investigation of Landing Gear Noise

by

Wen Liu

Thesis for the degree of Doctor of Philosophy

August 2011

ABSTRACT

Noise generated by aircraft landing gears is a major contributor to the overall airframe noise of a commercial aircraft during landing approach. Because of the complex geometry of landing gears, the prediction of landing gear noise has been very difficult and currently relies on empirical tools, which have limited reliability and flexibility on the applications of unconventional gear architectures. The aim of this research is to develop an efficient and accurate numerical method to investigate the generation and far field radiation of the landing gear noise. In this thesis a hybrid approach is developed that combines near field flow computations with an integral radiation model to enable the far field signal to be evaluated without the need to directly resolve the propagation of the acoustic waves. The recent advances in the CAA methods are implemented with high-order finite difference compact schemes and a characteristics-based multi-block interface treatment. Aerodynamic noise from a generic two-wheel landing gear model, provided by Airbus LAGOON (landing gear noise database for CAA validation) program, is predicted by using the hybrid approach and compared with the LAGOON database. The unsteady flow field is computed by using a compressible Navier-Stokes solver based on high-order finite difference schemes. The calculated time history of surface data is used in a FW-H solver to predict the far field noise levels. Both aerodynamic and aeroacoustic results are compared with wind tunnel measurements in good agreement. Individual contributions from three components, i.e. wheels, axle and strut of the landing gear model are also investigated to identify the major noise source component. It is found that strong flow-body interaction noise is generated by the flow separated from tire rim impinging on the axle. Based on the same landing gear model, the comparison study using conventional CFD solver FLUENT is performed with a second-order Navier-Stokes finite volume solver to compute the unsteady near field flow and the built-in FW-H solver to calculate the far field sound propagation. The comparison suggests that although conventional CFD method can obtain good time-averaged aerodynamic results, its ability of predicting sound radiation is limited by the inherent low-order numerical discretizations. The aerodynamic noise from the isolated undercarriage wheel with detailed hub configuration is also investigated using

FLUENT. The asymmetric phenomenon in the mean flow is discovered in the wake region of the wheel, which contributes to a positive lift force for the wheel. It is predicted that the isolated wheel radiates relatively strong noise to the sides with several strong tonal noise.

Contents

List of figures

List of tables

DECLARATION OF AUTHORSHIP

I, Wen Liu

declare that the thesis entitled

Numerical Investigation of Landing Gear Noise

and the work presented in the thesis are both my own, and have been generated by me as the result of my own original research. I confirm that:

- this work was done wholly or mainly while in candidature for a research degree at this University;
- where any part of this thesis has previously been submitted for a degree or any other qualification at this University or any other institution, this has been clearly stated;
- where I have consulted the published work of others, this is always clearly attributed;
- where I have quoted from the work of others, the source is always given. With the exception of such quotations, this thesis is entirely my own work;
- I have acknowledged all main sources of help;
- where the thesis is based on work done by myself jointly with others, I have made clear exactly what was done by others and what I have contributed myself;
- none of this work has been published before submission, or [delete as appropriate] parts of this work have been published as: [please list references]

Signed: ……..

Date:…….

Acknowledgements

Foremost, I would like to express my sincere gratitude to my supervisors Dr. Jae Wook Kim and Professor Xin Zhang for the continuous supports of my PhD study and research. Their knowledge, guidance and patience helped me in all the time of research and writing up this thesis.

I would also like to acknowledge the colleagues and friends in the Airbus Noise Technology Center (ANTC) at the University of Southampton for their invaluable support. Many thanks go to Ed Peers, David Angland, Kondwani Kanjere, Xiaoxian Chen for helping develop the high-order code in this research. Thanks to Koen Van Mierlo for sharing his experience in mesh generation with highly complex geometries.

Last but not the least, I'd like to thank the supercomputing services provided by the University of Southampton (IRIDIS3 cluster) and the Microsoft Institute of High Performance Computing (Spitfire cluster), without which this research would not be accomplished.

Definitions and abbreviations

Greek Symbols

γ	Ratio of specific heat coefficients
$\delta(\ )$	Dirac delta function
$\lambda_{\hat{A}}$	Eigenvalues of flux Jacobian matrix $\hat{A}$
$\lambda_{\hat{B}}$	Eigenvalues of flux Jacobian matrix $\hat{B}$
$\lambda_{\hat{C}}$	Eigenvalues of flux Jacobian matrix $\hat{C}$
μ	Molecular viscosity
ν	Kinematic viscosity
$\tilde{\nu}$	Working variable for turbulent viscosity
ρ	Fluid density
τ_{ij}	Viscous stress tensor
σ_{ij}	Reynolds stress tensor
τ	Pseudo-time
ξ, η, ζ	Generalized coordinates

Alphanumeric Symbols

a_0	Sound speed
$\hat{A}, \hat{B}, \hat{C}$	Flux Jacobian matrices
C_d	Coefficient of drag
C_l	Coefficient of lift
e_t	Total energy
E, F, G, Q	Inviscid fluxes of Navier-Stokes equations
$\hat{E}, \hat{F}, \hat{G}, \hat{Q}$	Generalized inviscid fluxes
f	Frequency
$H(\ )$	Heaviside function
I	Identity matrix
J	Coordinates transformation Jacobian

M	Mach number
p	Static pressure
p_{ij}	Compressible stress tensor
P_r	Prandtl number
Re	Reynolds number
t	Time
T	Temperature
T_{ij}	Lighthill stress tensor
u_i , u , v , w	Cartesian velocity components $(u_1, u_2, u_3) = (u, v, w)$
x_i , x , y , z	Cartesian coordinates $(x_1, x_2, x_3) = (x, y, z)$
y^+	Sub-layer scaled distance

Subscripts

$(\ )_\infty$	Freestream value
$(\ )_V$	Viscous value
$(\ )_t$	Turbulent value
$(\ )'$	Perturbation value
$(\bar{\ })$	Reynolds-averaged value

Abbreviations

2D	Two-dimensional
3D	Three-dimensional
APE	Acoustic perturbation equations
CAA	Computational aeroacoustic
CFD	Computational fluid dynamics
CFL	Courant-Friedrichs-Levy
DES	Detached eddy simulation
DNS	Direct numerical simulation
DRP	Dispersion-relation-preserving
FFT	Fast Fourier transform
FW-H	Ffowcs Williams and Hawkings

LDDRK	Low-dissipation and low-dispersion Runge-Kutta
LEE	Linearized Euler equations
LES	Large eddy simulation
NS	Navier-Stokes
RANS	Reynolds-averaged Navier-Stokes
RK	Runge-Kutta
S-A	Spalart-Allmaras
SPL	Sound pressure level, with a reference pressure of 20 μ Pa
URANS	Unsteady Reynolds-averaged Navier-Stokes

Chapter 1
Introduction

The purpose of this chapter is to place the research presented in this thesis into context with an examination of the relevant literature. The aims of the research are stated at the end of the chapter.

1.1. Overview

Aircraft noise is the sound pollution produced by aircrafts during various phases of the flight, especially during the takeoff and approach phases. Recently, it has become a significant environmental issue because of the rapid growth in air traffic and its increasing impact on the surrounding communities, which motivates us to better understand, predict and finally reduce the aircraft noise. Figure 1.1 shows a wide-body commercial aircraft passing close to houses near London Heathrow airport, one of the busiest airports all over the world. The nearby residents are continuously disturbed by the frequent air traffic until midnight everyday. The political consequence of the aircraft noise impact was the publication of the European visions 2020 [1] with the requirement, among others, to "reduce subjective noise impact by half" (i.e., minus 10 dB per operation by 2020 relative to the year 2000 technology). The financial consequences for the airlines, that noisier aircrafts have to pay higher taxes, actually drive the efforts of building quieter aircrafts. Hence both social and financial motivations exist for the PhD thesis research.

Figure 1.1: A Boeing 747-400 passes close to houses near London Heathrow airport.

Aircraft noise generally originates from two sources: the engine related noise such as fan noise and combustion noise, and the airframe noise arising from the airflow around the aircraft exposed surfaces. The engine noise dominates during the flight takeoff procedure. However during the approach and landing procedure, when the engines are often at idle, the airframe noise is comparable to, or sometimes greater than the engine noise [2]. The relative importance of various noise sources is shown in Figure 1.2.

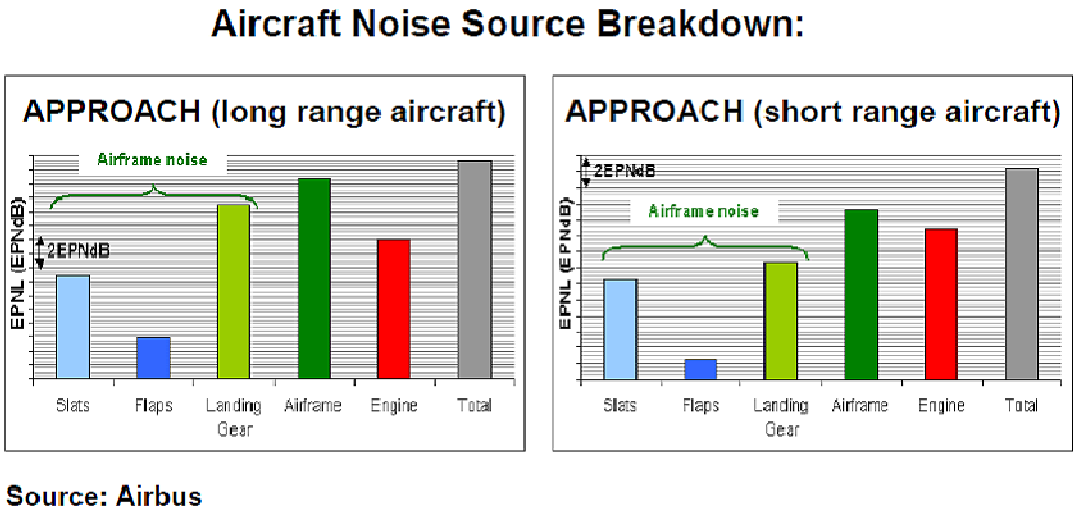

Figure 1.2: Aircraft noise sources.

For single aisle or short range aircraft the noise from high-lift devices is quite close to that from landing gears. However, on long range aircraft, such as wide-body

aircrafts, the airframe noise tends to be dominated by the landing gear noise [3]. Because of the multi-element geometry of aircraft landing gears, the flows around these aircraft components are rather complex and have complicated contributions to the airframe noise. As a result, the prediction of noise from such flows has been difficult and currently relies on empirical tools. These tools require heavy calibrations with existing test data; therefore have limited reliability on predicting noise from unconventional gear architectures at the design stage. Computational simulation for landing gear noise prediction would be a general method in principle, which could be applied to any novel landing gear architecture, because they do not need to be calibrated against existing test results. In the last decade, simulations of landing gear have evolved from heavily simplified geometries [4] to realistic detailed landing gear configurations requiring large computational grids [5]. Unstructured grid methodology has been gaining popularity in the CFD community in recent years with an advantage in terms of grid generation [6]. However, the large amount of grids (tens of millions of points) required by the unstructured methodology and corresponding low-order finite volume flow solver makes it rather expensive to perform aeroacoustic calculations on complex geometries. Structured grid methodology with high-order finite difference CAA solver could be another option with the advantages of: flexibility of grid refinement and accuracy in wave characteristics with limited number of grids. It should be mentioned that the structured grid methodology is currently impractical when going to much more realistic landing gear configurations, for which generating multi-block structured grid could become a nightmare. Considering the simplified geometry in this thesis, the computational simulations of the landing gear noise prediction have been performed with a fully structured grid and the high-order finite difference flow solver, to understand the mechanism of the landing gear noise generation. The radiated noise is compared to the experimental data to validate the current CFD/CAA tools.

1.2. Research Objectives

The primary objective of this research is to assess the application of the SotonCAA code with high-order finite difference schemes to realistic nose landing gear geometry, and investigate the generation and far field radiation of the landing gear noise. This involves the construction of a quality fully structured landing gear grid for the finite difference

CFD/CAA solver and the practices of CFD simulation combined with FW-H calculation to predict the far field noise radiation. The primary geometry for this research is the LAGOON baseline geometry. This is a two wheel simplified nose landing gear with a cylindrical main strut and cylindrical axle. The validation will be made by comparison to experimental data, which was provided by ONERA in its aerodynamic and anechoic wind tunnels [7]. The second-order conventional flow solver FLUENT will be compared to the high-order SotonCAA code, which will provide a direct assessment of the performance of the high-order SotonCAA code against the conventional code. Comparisons will be made on the same grid with grid induced differences removed.

The second objective is to explore the mechanism of landing gear noise generation using numerical tools. Both the full landing gear geometry and an isolated wheel, which is the primary gear component of the landing gear, are under investigation. The wheel geometry for simulation is the CADWIE isolated wheel [8], containing a cavity and some fine details within the hub. The CADWIE wheel is selected as the initial geometry for the practice of using hybrid CFD/FW-H methodology to predict far field noise, which is based on the conventional flow solver FLUENT.

1.3. Structure of Thesis

The rest of the thesis is organized as follows:

In Chapter 2, an extensive literature review has been conducted with relevance to the current research topic. This covers fundamental aerodynamics and aeroacoustics theories. Previous landing gear noise studies in experiment, prediction and computation are also discussed.

In Chapter 3, the details of the high-order SotonCAA code is presented, including the high-order finite difference N-S equation solver and the radiation model for sound propagation.

In Chapter 4, the landing gear noise prediction using high-order SotonCAA code is presented. The aerodynamic and acoustic results are discussed and compared with available experimental data, for the validation of current numerical method. The noise generation mechanism is investigated by the study of the noise contribution from landing gear components.

In Chapter 5, the comparison study of the landing gear noise prediction is performed using the conventional CFD tool FLUENT. The abilities in the far field noise predictions are compared between FLUENT and SotonCAA.

In Chapter 6, the isolated landing gear wheel is simulated using FLUENT to investigate the noise generation and radiation from the major component of the landing gear.

Finally in Chapter 7, the main results obtained are summarized and future works are proposed.

Chapter 2
Literature Review

This chapter first outlines necessary mathematical theories related to the landing gear noise generation and radiation, covering basic aerodynamics and aeroacoustics, which are the foundation stones in understanding noise source existence and distributions. After that an extensive review of the landing gear noise research is presented.

2.1. Aerodynamics

Landing gear related airframe noise is the aerodynamic noise arising from the airflow around the aircraft exposed surfaces. This noise-generating airflow is governed by the Navier-Stokes equations (N-S), which are based on the fundamental physical principles of the conservation laws of mass, momentum and energy. The conservation of mass is expressed mathematically in the continuity equation (using summation convention)

$$\frac{\partial \rho}{\partial t} + \frac{\partial \rho u_i}{\partial x_i} = 0 . \tag{2.1}$$

The conservation of momentum is written as

$$\frac{\partial \rho u_i}{\partial t} + \frac{\partial \rho u_i u_j}{\partial x_i} = -\frac{\partial p}{\partial x_i} + \frac{\partial \tau_{ij}}{x_j} + F_i . \tag{2.2}$$

In addition, we assume a Newtonian fluid that obeys Stokes's hypothesis. Therefore, the viscous stress tensor is

$$\tau_{ij} = \mu(-\frac{2}{3}\frac{\partial u_k}{\partial x_k}\delta_{ij} + \frac{\partial u_i}{\partial x_j} + \frac{\partial u_j}{\partial x_i}) . \tag{2.3}$$

Many flows are characterized by two critical non-dimensional parameters: the Mach number $M = U/a_0$ which provides a measure of compressibility of the flow, and the Reynolds number $\mathrm{Re} = UL/\nu$ which represents a ratio of inertial forces to viscous forces. In these parameters, U is a velocity scale in the flow and L is a length scale. In a typical aerodynamic flow past a body, the Reynolds number is estimated with the free-stream velocity and the body reference length.

Reynolds numbers are often used to help characterize different flow types. Laminar flow occurs at low Reynolds numbers when viscous forces are dominant, and is characterized by smooth, constant fluid motions; while turbulent flow occurs at high Reynolds numbers and is dominated by inertial forces, which tend to produce random eddies, vortices and other flow fluctuations. In a turbulent flow, there is a range of scales of the time varying fluid motions. The size of the largest scale of fluid motion is determined by the overall geometry of the flow. The size of the smallest scales is related to the Reynolds number. As Reynolds number increases, increasing smaller scales of the flow are visible. A large Reynolds number indicates that viscous forces are not strong enough at large scales of the flow, to dissipate their motions dominated by inertial forces. The kinematic energy must be transported progressively from large scales to smaller scales until that the scale is small enough for viscosity to become of the same order of inertia, where the dissipation of energy by viscous action finally takes place. Therefore, since the largest eddies are dictated by the flow geometry and the smallest scales are related to the viscosity, the Reynolds number can be also understood as the ratio of the largest scales of the turbulent motion to the smallest ones. From the computational point of view, large Reynolds number requires large number of grid points in order to capture small scales of flow features, which sometimes can be unaffordable for direct numerical simulations (DNS).

Turbulent flows not only involve a wide range of flow scales but also evolve significantly with random motions. Due to the high uncertainty in the turbulent flow field, an averaging process is introduced as the Reynolds-averaged Navier-Stokes (RANS) equations. The quantities within the N-S equations are decomposed into their mean and fluctuating components. This decomposition results in an extra Reynolds stress term which is a product of the fluctuating velocity field. The momentum equation is written as

$$\frac{\partial \rho \overline{u_i u_j}}{\partial x_j} = -\frac{\partial \bar{p}}{\partial x_i} + \frac{\partial (\bar{\tau}_{ij} + \bar{\sigma}_{ij})}{\partial x_j}, \tag{2.4}$$

where $\bar{\sigma}_{ij} = \rho \overline{u_i' u_j'}$ is the Reynolds stress tensor.

To close the equations, the Reynolds stress tensor is estimated by the combination of the mean flow variables and the turbulent viscosity μ_t as follows,

$$\bar{\sigma}_{ij} = 2\mu_t S_{ij} - \frac{2}{3}\rho k \delta_{ij} \tag{2.5}$$

where S_{ij} is the mean rate of strain tensor, K is the turbulent kinetic energy. The turbulent viscosity μ_t can be calculated from the turbulent viscosity transport equations of corresponding turbulence models. Commonly employed models in the modern engineering applications include Spalart-Allmaras (S-A) [9], k-ε (k-epsilon) [10], and k-ω (k-omega) [11] models. The S-A model uses only one additional equation to model turbulent viscosity transport, while the k models use two. In CFD practice, unsteady Reynolds-averaged Navier-Stokes equations (URANS) are often used to solve the turbulent flow field. The concept of URANS is that flow variables are only averaged over small time scales while they are still time dependent over large time intervals, which means, in terms of mathematics, the time derivative term would be kept in the RANS equation. Since URANS methods provide relatively "averaged" results, they may not perform well in predicting instantaneous flow characteristics.

Large-eddy simulation (LES) is an alternative method capable of modeling small unsteady flow characteristics, which is based on Kolmogorov's theory of self similarity. In his theory, large eddies of the flow are dependent on the flow geometry, while smaller eddies are self similar and have a universal character. For this reason, we can resolve the large eddies explicitly, and model the effect of the smaller and more universal eddies on the larger ones. Thus, in LES the large scale motions of the flow are calculated, while the effect of the smaller universal scales (the so called sub-grid scales) are modeled using a sub-grid scale (SGS) model [12].

LES requires less computational effort than DNS but more effort than those methods that solve URANS. The computational demands increase significantly close to the walls, where the characteristic scale is too small, and usually exceeds the limits of

modern supercomputers. For this reason, zonal approaches are often adopted, with RANS or other empirically-based models replacing LES in the wall region. Detached eddy simulation (DES) is such a modification of the RANS model in which the model switches to a sub-grid scale formulation in regions fine enough for LES calculations [4]. Regions near solid boundaries and where the turbulent length scale is less than the minimum grid dimension are assigned the RANS mode of the solution. As the turbulent length scale exceeds the grid dimension, the regions are solved using the LES mode. DES has less grid resolution requirement than pure LES, thereby considerably cuts down the cost of the computation. Hedges, et al. [4] compared DES and URANS in the landing gear simulations, and suggested that with the Spalart-Allmaras (S-A) turbulence model [9], DES performed consistently better than URANS calculation in the time-averaged sense. For instantaneous flow fields, DES developed a much wider range of unsteady scales of motions which is promising for noise prediction. The same preference was also suggested by Lockard, et al. [13] in the case of a more complicated gear model. Spalart et al. [14] have recently modified the DES model to overcome some of the shortcomings related to its grid dependence in a new model named Delayed Detached Eddy Simulation or DDES. The DDES model applies a blending function that varies between 0 for RANS mode and 1 for LES mode to the destruction terms.

2.2. Aeroacoustics

Noise generation can be associated with turbulent fluid motions and aerodynamic forces interacting with body surfaces, which is the scope of the aeroacoustic research. Most practical aeroacoustic analysis relies on the acoustic analogy [15], where the governing equations of the fluid motions can be solved in a similar form of the classic wave equations. Computational Aeroacoustics (CAA) is the application of numerical methods to compute the approximate solutions of the governing equations for the specific aeroacoustic problems.

2.2.1. General Noise Sources

In mathematics, the elementary solutions of the wave equation are described as the sound sources, and can be categorized into three major types based on their generating

mechanism: monopole, dipole, and quadruple. Different types of sources have distinct directivity characteristics, which is helpful in understanding the physics of sound generation and radiation.

Monopole, also known as a point source, is associated with the displacement of the fluid mass due to the acceleration of the moving surface. The acoustic waves generated by a monopole are propagating equally in all directions. The directivity pattern appears in the form of a circle as shown in Figure 2.1(a).

The simplest dipole source consists of two point sources which are of equal strength infinitely close to each other, operating at the same frequency with phase difference of half periods. The dipole is generated by fluctuating force acting on the solid surface, and its directivity pattern shows two lobes with maxima along upward and downward directions in Figure 2.1(b). Sound is cancelled in forward and backward directions.

A quadruple consists of two identical dipoles which are opposite in phase. There are two kinds of quadruples: the lateral quadruple and the longitudinal quadruple. The lateral quadruple has the axes of dipoles not lying on a same line, and has a directivity pattern with four lobes as shown in Figure 2.1(c). The lateral quadruple is associated with the shear stress and can be found in all turbulent flows. The longitudinal quadruple has the axes of dipoles lying on the same line, and has a directivity pattern similar to a dipole.

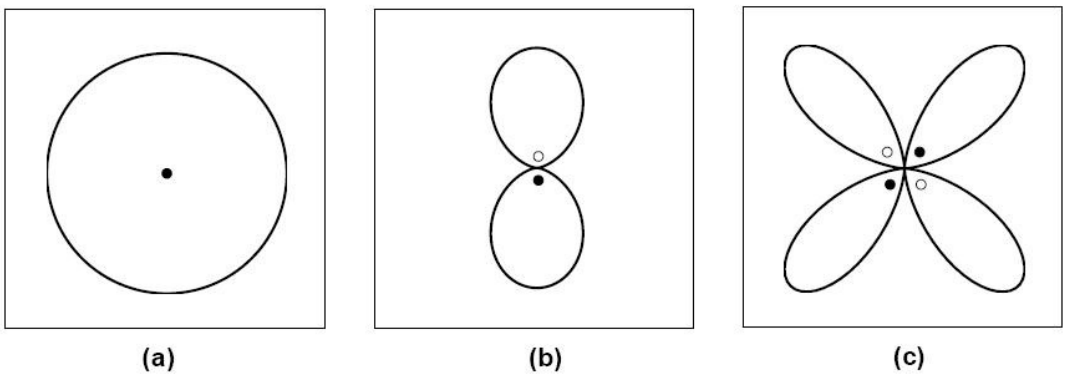

Figure 2.1: Directivity patterns for acoustic sources; (a) monopole; (b) dipole; (c) quadruple.

Generally speaking, aerodynamic noise involves the unsteady flow noise and the interaction noise. The flow noise is generated entirely by unsteady motions away from

the boundary surfaces, and the noise sources can be described as monopole or quadruple types. The interaction noise originates from the interactions of unsteady flows with stationary or moving surfaces and acts in the dipole behavior. The practical examples of different types of sound sources are demonstrated in Fig. 2.2.

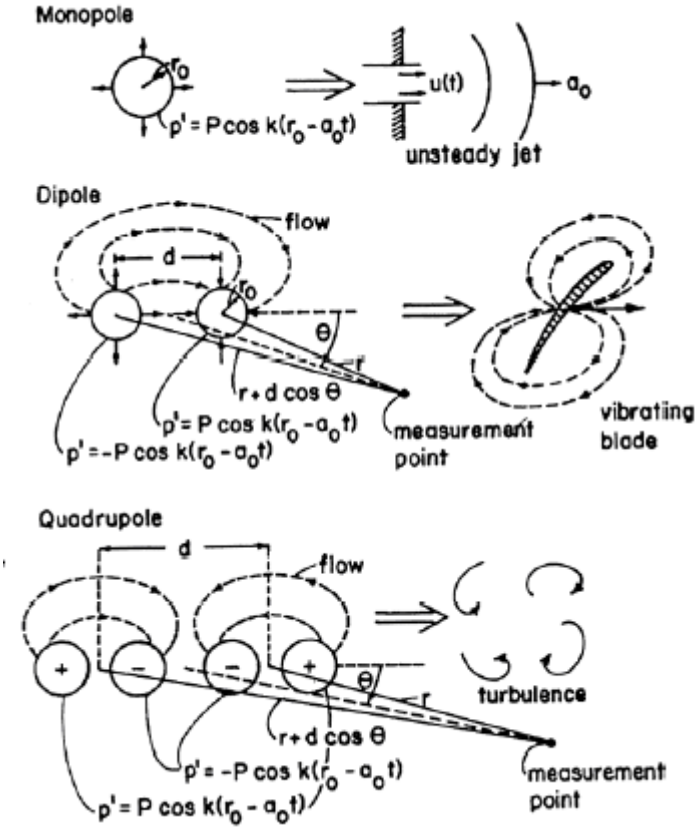

Figure 2.2: A demonstration of aerodynamic noise sources [16].

2.2.2. Acoustic Analogy

Early in 1950s, Lighthill [15] first uncovered the fundamental mechanism of conversion of energy between two forms, the kinematic energy of fluctuating shearing motions and the acoustic energy of fluctuating longitudinal motions. He confirmed that sound can be generated aerodynamically as a by-product of an airflow, which is different from sound produced by the vibration of solids. The approach is proposed that the details of the flow are firstly to be estimated from aerodynamic principles not concerned with the acoustic propagation of fluctuations in the flow, and secondly the sound field is to be deduced, ignoring the phenomena where there is a significant back-reaction of the

sound produced on the flow field itself. Evidence suggests that the sound produced is so weak relative to the motions producing it that no significant back-reaction can be expected unless there is such a resonator present to amplify the sound [15].

Based on Lighthill's theory, the whole flow field is divided into two parts: one contains most of the unsteady flow features and the remainder is at rest. The governing equations for the two parts are different, one of which governs the fluctuation of density in the real flow while the other is suitable for the uniform acoustic medium. The difference between the two equations is considered as if it were the effect of fluctuating external forces acting on the uniform acoustic medium, and radiating sound into it according to the ordinary laws of acoustics.

The propagation of sound in a uniform medium, without sources of matter or external forces, is governed by the equation

$$\frac{\partial^2 \rho}{\partial t^2} - a_0^2 \nabla^2 \rho = 0 . \tag{2.6}$$

On the other hand, the exact equation of momentum in an arbitrary continuous medium without external forces is

$$\frac{\partial \rho u_i}{\partial t} + \frac{\partial}{\partial x_j}\left(\rho u_i u_j + p_{ij}\right) = 0 . \tag{2.7}$$

According to Eq. (2.3) for Newtonian fluid, the compressive stress tensor is

$$p_{ij} = p\delta_{ij} - \mu\left(-\frac{2}{3}\frac{\partial u_k}{\partial x_k}\delta_{ij} + \frac{\partial u_i}{\partial x_j} + \frac{\partial u_j}{\partial u_i}\right), \tag{2.8}$$

which represents the force in the x_i direction acting on a portion of fluid, per unit surface area with inward normal in the x_j direction. The equation of momentum can be rearranged as

$$\frac{\partial \rho u_i}{\partial t} + a_0^2 \frac{\partial \rho}{\partial x_i} = -\frac{\partial T_{ij}}{\partial x_j} , \tag{2.9}$$

where $T_{ij} = \rho u_i u_j + p_{ij} - a_0^2 \rho \delta_{ij}$ is known as Lighthill tensor. It represents the difference between the effective stresses in the real flow and the stresses in the uniform acoustics medium, which is comparative to external fluctuating forces acting on a uniform medium. This can be easily shown by combining Eq. (2.1) and Eq. (2.9), and the rearranged sound propagation equation is

$$\frac{\partial^2 \rho}{\partial t^2} - a_0^2 \nabla^2 \rho = \frac{\partial^2 T_{ij}}{\partial x_i \partial x_j}. \tag{2.10}$$

For the airflow in a uniform atmosphere, the stress system can be neglected outside the flow itself, since the velocity u_i is small and appears quadratically. Also the viscous stresses in p_{ij}, and the conduction of heat both have small effect. Thus outside the airflow the density satisfies the ordinary sound equation Eq. (2.6), and the fluctuations in density caused by the effective applied stresses within the flow, are propagated acoustically.

If T_{ij} is known exactly, then the density perturbation $\rho' = \rho - \rho_o$ (ambient density) can be obtained, using Green's Functions [17]

$$\rho'(\mathrm{x}, t) = \frac{1}{4\pi a_0^2} \int_V \frac{1}{r} \frac{\partial^2 T_{ij}(\mathrm{y}, \tau)}{\partial x_i \partial x_j} d\mathrm{y}, \tag{2.11}$$

where V is the finite volume of the flow field over which T_{ij} is non-zero, $\boldsymbol{r} = |\mathbf{x} - \mathbf{y}|$ is the separation distance between the source point **y** and the observer position **x**, and $\tau = t - \boldsymbol{r}/a_0$ is the retarded time. The retarded time accounts for the time required for sound emitted at the source point **y** to propagate to the observer position **x**. In the integral above, the sound source is represented by a quadruple field $\partial^2 T_{ij}(\mathbf{y}, \tau) / \partial x_i \partial x_j$. If we let $x = (x_i x_i)^{1/2}$, and use the result $\partial x / \partial x_i = x_i / x$, it can be shown that $\partial^2 / \partial x_i \partial x_j = (x_i x_j / a_0^2 x^2) d^2 / dt^2$. Hence, for an observer at **x** in the far field ($x >> \lambda$, where λ is a typical wave length of the generated sound), the double divergence can be approximated with a second time derivative to give

$$\rho'(\mathrm{x},t)=\frac{1}{4\pi a_0^4}\frac{x_i x_j}{x^3}\int_V \frac{\partial^2 T_{ij}(\mathrm{y},\tau)}{\partial t^2}d\mathrm{y}. \tag{2.12}$$

A useful and practical deduction with dimensional analysis can be obtained given volume integral above. For low Mach numbers, in unbounded flow the stress tensor can be estimated by $\rho u_i u_j$ (Lighthill reasoned that under certain circumstance it would be the dominant factor [15]), which has a scale of ρU^2. Since Strouhal number $f\,l/U$ has been found to vary far less with changing conditions (like Reynolds number), one may take frequency as proportional to $U\,/\,l$. Now, we can find that the density variation is dimensionally proportional to the product as

$$\rho' \propto \frac{1}{a_0^4}\frac{1}{x}\left(\frac{U}{l}\right)^2 \rho U^2 l^3 = \rho\left(\frac{U}{a_0}\right)^4 \frac{l}{x}. \tag{2.13}$$

Extension to Lighthill's Theory

One of the restrictions for the Lighthill's theory is that the sound wave estimated is only for free sound field, where the effects of reflection, diffraction, absorption or scattering by solid boundaries are all neglected. Later, the solution of Eq. (2.11) was extended by Curle [18] to include the effects of solid walls. The corresponding solution is given by

$$\rho'(\mathrm{x},t)=\frac{1}{4\pi a_0^2}\left(\int_V \frac{1}{r}\frac{\partial^2 T_{ij}(\mathrm{y},\tau)}{\partial x_i \partial x_j}d\mathrm{y}+\frac{\partial}{\partial x_i}\int_S l_j \frac{(\rho u_i u_j + p_{ij})}{r}dS(\mathrm{y})-\frac{d}{dt}\int_S l_i \frac{(\rho u_i)}{r}dS(\mathrm{y})\right), \tag{2.14}$$

where l_i is the i th component of the outward-pointing vector, normal to the fluid. The first surface integral in Eq. (2.14) describes the distribution of dipoles on the surface, and the second surface integral represents the distribution of monopoles on the surface, due to the mass addition at the boundary. If there is zero normal velocity at solid boundaries, which is if each surface is fixed or is vibrating in its own plane, we have $l_i u_i \equiv 0$. Hence Eq. (2.14) would be simplified as

$$\rho'(\mathrm{x},t)=\frac{1}{4\pi a_0^2}\left(\int_V \frac{1}{r}\frac{\partial^2 T_{ij}(\mathrm{y},\tau)}{\partial x_i \partial x_j}d\mathrm{y}+\frac{\partial}{\partial x_i}\int_S l_j \frac{\left(\rho u_i u_j + p_{ij}\right)}{r}dS(\mathrm{y})\right). \tag{2.15}$$

The sound field therefore can be generated in a hypothetical unbounded uniform medium, with a volume distribution of quadruples $\partial^2 T_{ij}(\mathbf{y},\tau) / \partial x_i \partial x_j$ throughout the region external to the solid bodies and a surface distribution of dipoles $\partial p_{ij}(\mathbf{y},\tau) / \partial x_i$ acting on the surfaces of the solid bodies. In much the similar way as Lighthill suggested, the dipole sources can be also simplified as

$$\rho'(\mathrm{x},t)_{dipole}=\frac{1}{4\pi a_0^2 \mathrm{x}}\frac{x_i}{a_0 \mathrm{x}}\frac{\partial}{\partial t}\int_S l_j p_{ij}(\mathrm{y},\tau)dS(\mathrm{y}). \tag{2.16}$$

and the dimensional analysis yields

$$\rho'_{dipole} \propto \frac{1}{a_0^3}\frac{1}{x}\frac{U}{l}\rho U^2 l^2 = \rho\left(\frac{U}{a_0}\right)^3 \frac{l}{x}. \tag{2.17}$$

Comparing dipole source and quadruple source dimensionally, it can be shown that

$$\frac{\rho'_{quadrupole}}{\rho'_{dipole}}=\frac{U}{a_0}=M. \tag{2.18}$$

It suggests that at sufficiently low Mach numbers, the contribution from dipole sources should be greater than that from quadruples.

Ffowcs Williams and Hawkings [17] (FW-H) further generalized the form of the Lighthill's acoustic analogy to include moving surfaces. Following Brentner and Farassat [19], the FW-H equation can be written in a differential form as

$$\left(\frac{\partial^2}{\partial t^2}-a_0^2\nabla^2\right)\rho'(\mathrm{x},t)=\frac{\partial^2}{\partial x_i \partial x_j}\left[T_{ij}H(f)\right]-\frac{\partial}{\partial x_i}\left[F_i\delta(f)\right]+\frac{\partial}{\partial t}\left[Q\delta(f)\right], \tag{2.19}$$

where $f = 0$ describes an integration surface, $f < 0$ is inside the integration surface, $\delta(f)$ is the Dirac delta function, and $H(f)$ is the Heaviside function. The quantities Q and F_i are defined by

$$Q = \left(\rho_0 v_i + \rho(u_i - v_i)\right)\frac{\partial f}{\partial x_i}, \text{ and } F_i = \left(p_{ij} + \rho u_i(u_i - v_j)\right)\frac{\partial f}{\partial x_j}. \qquad (2.20)$$

In the above equations, v_j is the velocity of the integration surface $f = 0$. n_j is the outward unit normal to the surface $f = 0$. The dipole term F_i involves an unsteady force, and Q gives rise to a monopole-type contribution that can be considered as an unsteady mass addition.

The FW-H equation is an exact rearrangement of the N-S equations and hence is efficient and amendable to numerical computations. These equations can also be solved in the frequency domain which is useful when analyzing radiated sound frequencies [20, 21].

2.2.3. Computational Aeroacoustics

Direct Numerical Simulation

With the help of fast growing computing capabilities, it is possible and becoming much more popular, for the reason of cost saving, to conduct computational simulations for aeroacoustic problems. After Lighthill discovered that sound can be generated as a by-product of an airflow (known as the acoustic analogy), it is understood that aerodynamic noise could be computed by directly solving the fully compressible flow equations in a domain that includes both the aerodynamic noise sources and the observers. Although conventional computational fluid dynamics (CFD) methods have been very successful for the aerodynamic computations, it is not possible to simply use existing CFD codes to directly calculate the sound generations and radiations to far field, because the characteristics of aeroacoustic problems are distinctly different from those commonly encountered in aerodynamics [22, 23]. Aeroacoustic problems are, by definition, time dependant. They must be treated time-accurately with appropriate consideration of all relevant time-scales and spectral analysis requirements, for example the requirement of frequency range of human ear sensitivity. Furthermore, since the computed sound fields

need to be propagated over large distances comprising many wavelengths, the numerical schemes of CAA must be highly accurate with low dispersion and dissipation. For practical geometries, the direct computation involving both sound generation and propagation is probably unrealistic in 20 years [24], due to the high demand on computing resources.

Hybrid Approach

The hybrid approach does not directly resolve the small acoustic perturbations up to the far field observer, therefore reducing the computational cost significantly. In the hybrid approach the computational domain is split into different regions, such that the acoustic and flow field can be solved with different governing equations and numerical techniques [25]. This would involve using two different numerical solvers, first a dedicated CFD tool and secondly an acoustic solver. The flow field is firstly calculated in the near field to collect the acoustic sources. Then, these acoustic sources are provided to the second solver which calculates the acoustic propagation in an inexpensive way. Acoustic propagation can be calculated via either Linearized Euler equations (LEE) [26] and Acoustic perturbation equations (APE) [27, 28] or integral methods such as Kirchhoff integral [29] and FW-H integral [17]. For low Mach number flows, the acoustic propagation may not be influenced by the non-linearity and the LEE/APE becomes applicable by only dealing with perturbations. Different from the LEE method that supports three types of wave perturbations, i.e. acoustic waves, vorticity waves and entropy waves, APE only models the acoustic propagations. Integral methods are based on the known solution of the acoustic wave equation in the form of surface and volume integrations. The difference between Kirchhoff integral and FW-H is that Kirchhoff integral is derived from linearized wave equation neglecting non-linearity while FW-H comes from Lighthill acoustic analogy directly following the N-S equations. When considering the same assumption as Kirchhoff linear theory, the FW-H method equals to Kirchhoff method. However, the FW-H equation is more general and accurate even if the integration surface lies in the non-linear region.

Finite Difference Schemes of CAA

In the hybrid methods the unsteady flow field must be computed accurately within a region containing the sources. Because the flow is compressible, sound waves exist within the flow. The amplitude of sound waves is so small compared to the characteristic flow perturbations, that the accuracy required for calculating the waves is very high which results in the demand of high-order accurate schemes.

For spatial discretization, the most popular schemes used in the CAA are high-order finite-difference schemes because of the high accuracy and simplicity of implementations [30]. There are two main classes of high accuracy finite difference schemes, which are explicit and compact schemes. Explicit schemes directly compute the numeric derivatives by employing large number of computational points for high accuracy [31]. Compact schemes (implicit schemes) [32] employ fewer points by solving a matrix for the numerical derivatives along a grid line, where the numerical derivative at each point depends on the value of the derivative at neighbor points. The advantage of compact scheme is the higher accuracy than the explicit scheme, based on limited grid points; while the disadvantage is that a linear system of equations has to be solved resulting in high computing demand.

The dispersion-relation-preserving (DRP) scheme of Tam et al. [31] is an explicit scheme with seven-point central-difference stencil. DRP schemes have the same wave propagation characteristics and the same wave speeds as those of the Euler equations, and can provide high quality wave solutions. The method of Fourier transforms is usually used to optimize the finite difference approximations of the space and time derivatives in the wave-number and frequency space, providing better wave-number resolution.

Hixon [33, 34] developed compact differencing schemes of up to 6th-order accuracy, which are suitable for solving aeroacoustic problems. In Hixon's approach, the derivative operator is split into forward and backward operators. Only three points are needed to obtain the biased derivatives and only two independent bi-diagonal matrices are needed to be reversed instead of solving tri-diagonal linear system of equations. To improve the resolution characteristics of Hixon's scheme, an optimization strategy is developed by Ashcroft and Zhang [35], in which order of accuracy is sacrificed in preference to resolution characteristics across the range of wave-numbers

on a given mesh. The optimized schemes improve the dispersion characteristics, making them more accurate for high resolution calculations in aeroacoustics.

There are also two types of schemes for time integrations, categorized by explicit or implicit. In general, explicit time integration schemes have many advantages, only requiring no matrix inversions, limited computer memories, and less effort to construct. We commonly use Runge-Kutta method [36] to approximate the solutions of ordinary differential equations. If we take U^n and U^{n+1} to be the flow states at two successive times, a *m*-stage Runge-Kutta general scheme can be defined as

$$\begin{aligned} U^{(0)} &= U^n, \\ U^{(l)} &= U^{(0)} + \frac{\Delta t}{m-l+1}\left(\frac{\partial U}{\partial t}\right)^{l-1}, \; l = 1,2,\cdots,m; \\ U^{n+1} &= U^{(m)}. \end{aligned} \tag{2.21}$$

The number of stages and the coefficients can be specified to give a certain order of accuracy or to provide extra characteristics. For example, a low dispersion and dissipation Runge Kutta (LDDRK), which is 4th-order accurate for linear problems and 2nd-order accurate for non-linear problems, consists of two storage level marching cycle (4-6 LDDRK) [37]. The disadvantage of the explicit methods is that the time step size is restricted by the stability conditions of the algorithms rather than by the frequency content of the flow fluctuations. In addition, the situation is even worse if computations must be carried out for extended periods of time in order to collect statistical information of the flows. The implicit technique may be considered as a desirable alternative by allowing larger time increments [38, 39]. A lower-upper factorization with a symmetric Gauss-Seidel relaxation technique (LU-SGS) has become increasingly popular, due to its high efficiency [40].

Radiation Boundary Conditions

Radiation boundary conditions are crucial factors to obtain high accuracy in computing the flow/acoustic field. In practice, the domain in the physical problem extends to infinity, whilst the computational domain is truncated. At these computational boundaries, reflections of waves into the domain are numerical artifacts. In some particular cases, the adverse influence of boundary conditions can be avoided by using a

sufficiently large computational domain, where the time required for an acoustic wave to reflect exceeds the calculated time length [41].

A variety of non-reflecting boundary conditions have been developed that reduce spurious reflections at the edges of truncated computational grids. Three of the main types of non-reflecting boundary conditions [42] are characteristic based methods [43-47], far field asymptotic solutions [31, 48-50] and Absorbing boundary conditions (buffer zone) [51-53]. In characteristic methods, the boundary condition is formulated by conducting a one-dimensional characteristic analysis of the Euler equations. The boundary equations can be written in characteristic form, and the non-reflecting boundary condition is created by assigning the value of the characteristic that represents waves entering at the boundary. Due to the one-dimensional formulation, they perform best when the out-going wave is normal to the grid boundary. A buffer zone layer usually consists of 10 to 20 mesh points in which damping terms are introduced to damp out the acoustic waves. Buffer zone boundary conditions are easy to implement, but the inclusion of artificial damping within the buffer zone means that the solution is not physical. The addition of extra grid points in the buffer zones adds to the computational cost.

FW-H Integration Surface

An important issue in the FW-H calculation is the choice of the integral surface that separates the source region from the external field. In order to reduce the cost, the size of integral surface should be designed as small as possible, while the accuracy demand requires the integration surface to be sufficiently large to include as many noise sources as possible [54]. This is a trade-off between cost and accuracy, which should be considered carefully. In practice, one can consider the solid wall as the integration surface, and ignore the volume integration if the quadruple sources are not that significant. Cox, et al. [55] showed that in the Reynolds number range considered ($10^2 < Re < 5\times10^6$), for most observer positions, the unsteady forces on the solid surface of the cylinder were responsible for generating far more of the total noise than the volumetric noise produced away from the solid surface. Therefore, solutions to the FW-H equation should not differ much with the choice of the integration surface. However, with a permeable surface, it is easy to include the quadruple sources inside without performing

any volume integrations, which can significantly improve the accuracy of the noise predictions at locations where nonlinear interactions in the flow cannot be ignored [56].

One concern with the use of a permeable integration surface is that nonacoustic variations passing through the integration surface might seriously degrade the resulting acoustic calculation. The paper published by Lockard, et al. [13] suggests that computations with the permeable surfaces appear to be contaminated by strong wake flows passing through the surfaces compared to the calculations with solid surfaces which are in good agreement with CFD data in the flow field as long as wakes are not present. One possible reason suggested by Lockard, et al. is that the strength of the vortices is too large, and the errors caused by vortices passing through the surfaces were suspected as the noise sources which produce sound levels that are significantly higher than those when using the solid surfaces. Lockard and Casper [57] tried to introduce a correction for the error, which was found to work reasonably well in several test cases where the error is a small fraction of the actual radiated noise.

2.3. Landing Gear Noise

2.3.1. General Noise Characteristics

Landing gears have in the past been considered as a component only performing in a short period compared to the aircraft total operation time. Therefore, the previous configuration design of the landing gears was highly non-streamlined. Both nose and main landing gears consist of many components, such as wheels, axles, shafts with lateral support struts, drag braces, actuators, doors and a wheel-well to accept the gear when retracted, see Fig. 2.3. From the scale of major landing gear components, it is expected that low-frequency wake phenomena will occur. Hence corresponding sound characteristics will likely be of low-frequency. On the other hand, small-scale structural elements such as wires, hoses, screw-holes, small diameter cylindrical struts, etc., would probably generate high-frequency noise. Thus, we would expect a fairly broadband frequency spectrum to be emitted from landing gears.

Figure 2.3: Typical landing gears of A320: (a) nose landing gear; (b) main landing gear.

Heller and Dobrzynski [58] conducted experiments to determine the noise radiation from landing gear configurations of large commercial aircraft and show a broad spectral peak between a Strouhal numbers of 0.8 to 8. The position of the spectral peak is dependent on the dimensions and configurations of the specific landing gear, and is normally observed at low to mid frequencies. The contributions from components to the whole landing gear noise were investigated by exposing individual components to the flow. This approach neglects the significant interaction effects between components but still provides useful information about how the spectrum is made up. The measured spectrum is depicted in Fig. 2.4.

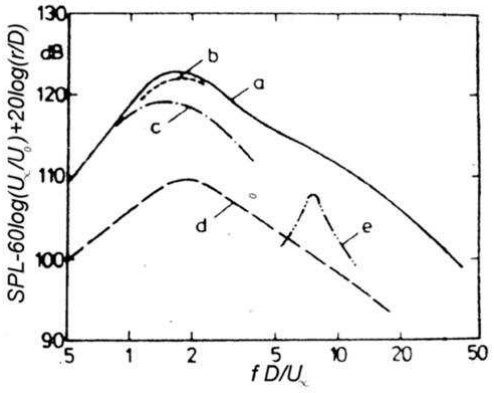

Figure 2.4: Typical landing gear noise spectrum: a) complete configuration; b) side support struts; c) lower drag brace actuator; d) wheel; e) door [58].

The landing gear noise is broadband in nature; however from some components tonal noise could also be identified. Landing gear structures are normally connected through joints with hollow pins. Flow-induced cavity resonances in these pin holes can result in prominent tonal noise. An example from full-scale gear tests in the wind tunnel is shown in Fig. 2.5. Whether or not such resonances are excited depends on the local flow conditions, which are highly affected by the position of the pin relative to the gear structure and the changing aircraft operational conditions (e.g., cross wind). Therefore, it is difficult to predict the potential of cavity resonance related tonal noise generation [1].

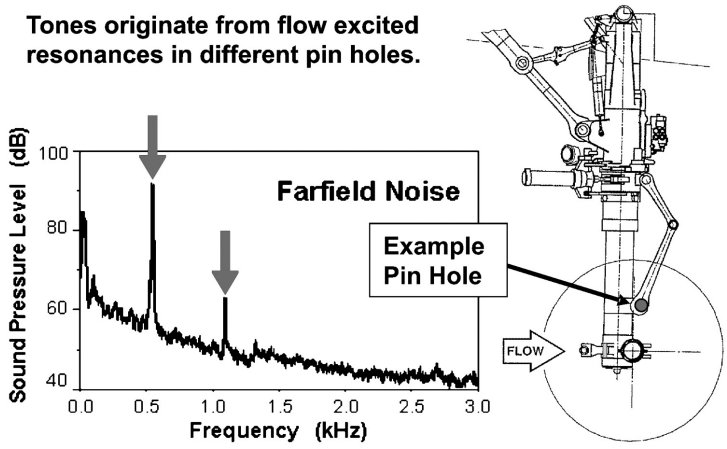

Figure 2.5: Example of flow-induced tonal noise from open pin holes in landing gear structures [59].

2.3.2. Noise Source Mechanism

Broadband noise from flow around landing gear structures is generated by: turbulent flow separation off the bluff body structural components, and the interaction of such turbulent wake flows with downstream gear components. The interaction of turbulent flow pressures with solid boundaries cause the turbulence energy to be transformed into sound pressure energy, which is the underlying noise source mechanism of landing gear noise. In the acoustic analogy this noise source mechanism is modeled by acoustic dipoles, and primarily governed by the velocity of the impinging flow and its turbulence characteristics. Investigation revealed that it would be beneficial to reduce local inflow

velocity, for example in the turbulent wake of an upstream located component, so as to minimize aerodynamic noise generation [3].

2.3.3. Landing Gear Types and Challenges

Typical aircraft landing gear system includes nose landing gear (NLG) and main landing gear (MLG), distinguished by their relative positions to the aircraft airframe. Nose landing gears are located under the nose of aircraft fuselage and normally have two-wheel structures with vertical oriented single strut, shown in Fig. 2.3(a). In general, nose landing gears produce a more pronounced dipole directivity pattern, radiating more noise to the sides [58]. Main landing gears are normally installed under the wings, and have four to six wheels structures with more complicated bogie and diagonal support systems, shown in Fig. 2.3(b). For medium and larger size civil aircraft, the main landing gears produce more noise than the nose gears due to its complex bogie system [60]. The directivity pattern from main landing gears seems to be more uniform with slight predominance to the sides [58].

Main landing gears are more affected by the installation effects than nose landing gear. The inflow velocity to a nose landing gear is almost equal to the flight speed, but the under-wing main landing gears experience reduced local inflow velocity due to the circulation flow induced by the wings [61-63]. Because of the strong effect of local flow velocity on the noise level, the installation effect must be accounted for when comparing wind tunnel test results with the test data from installed gears in-flight. The lower-wing surface also acts as an acoustic reflector. The sound reflections introduce acoustic interference effects to the noise level spectra, when the wavelength is smaller than the wing cord. However, these interferences at corresponding frequencies partially cancelled out because the gear structure represents a geometrically extended cluster of sound sources with various distances to the reflecting wings [64].

2.3.4. Experimental Measurement for Landing Gears Noise

When airframe noise was identified as a major aircraft noise component in approach condition, the scaled model wind tunnel experiments were conducted to quantify the landing gear noise characteristics. The generic landing gear model used in these experiments lack geometrical details, and thus provided misleading results that landing

gear noise was considered as a low-frequency phenomenon. In the 1990s, when full-scale landing gears were noise tested in the large high-quality acoustic wind tunnel facilities [65, 66], it turned out that landing gear noise covers a large frequency range sensitive to human noise perception. More recently, wind tunnel measurements tested high-fidelity scaled model gears and provided good results [67, 68], suggesting that scaled models with sufficient geometrical details can also be accepted in the landing gear noise studies.

When measuring the noise generated by landing gears in wind tunnel, the background noise (for example, the engines compressing the air) must be taken in account and collected sound signal should be corrected responsively. In addition, when a sound source is placed in the wind tunnel core flow whereas the measuring microphones are placed outside, the sound waves have to pass through the shear-layer separating the open jet from the ambient air. This leads to a change in propagation direction and amplitude of the sound waves. To account for these effects the data must be also corrected.

While the stationary measurements allow a fairly detailed investigation of individual noise contributors and directivity, they lack the important feature of the relative motion between source and receiver. Flyover measurements are considered important to determine whether the ground based test results could be applied to the realistic flight situations.

Two Wheel Landing Gear Measurements

Guo, et al [69] conducted aeroacoustic experiments on a full scale Boeing 737 landing gear in Boeing's LSAF (Low-Speed Aeroacoustic Facility) wind tunnel with Mach numbers ranging between 0.18 and 0.24. The measurements employed phased microphone array along with far filed microphone technique to record the acoustic signals. The collected data formed part of the knowledge base for validating Guo's prediction methodologies [70].

The 40% scale A320 simplified nose landing gear model was tested under LAGOON (LAnding Gear nOse database for CAA ValidatiON) project [7, 71] by Airbus France. The objectives of the project are to build an extensive and accurate experimental database for a simple landing gear structure to enable the validation of aeroacoustic numerical tools for landing gear applications based on steady/unsteady

CFD and CAA codes, and to assess available CFD/CAA tools on this configuration. The aerodynamic measurement was performed in the ONERA's F2 aerodynamic wind tunnel with closed section. Both steady and unsteady pressure signals on the landing gear surface were collected via static pressure taps and Kulite pressure sensors. PIV and LDV measurements were also performed in the wake of the wheels and struts. The acoustic measurements were conducted in ONERA's CEPRA19 open jet aeroacoustic wind tunnel, with far field microphones arcs and microphone arrays to record sound signals.

The 25% scale Gulfstream G550 NLG geometry was chosen as a benchmark configuration [72] proposed by NASA and the Gulfstream Aerospace company, and extensively discussed in the BANC-I conference (Benchmark problems of Airframe Noise Computations) in 2010. Experimental database were obtained through collaboration between NASA and University of Florida. Extensive aerodynamic measurements were performed in the closed-wall Basic Aerodynamic Research Tunnel (BART) at NASA [73] at M=0.12, 0.145, and 0.166. The data consisted of steady and unsteady surface pressures plus PIV results in the turbulent wake regions. The corresponding acoustic and limited surface pressure measurements were conducted in the open-jet University of Florida Aeroacoustic Flow Facility (UFAFF) [74] at M=0.145, 0.166, and 0.189. The good comparisons between the BART and UFAFF aerodynamic results indicate confidence in the wind tunnel data and provide a large range of validation opportunities for different partners to compare numerical methods at the BANC-I conference 2010.

Yokokawa et al. [75] took noise measurements of a 40% scale two wheel main landing gear, based on a 100-PAX class regional jet, at M=0.16. The high fidelity scale model includes small components such as the link mechanism, hydraulic tubes and electrical wiring. Acoustic measurements were conducted in the low speed wind tunnel at the Japanese Aerospace Exploration Agency (JAXA) and the large scale anechoic facility at the Railway Technical Research Institute (RTRI). The measurements showed major noise sources to be around the tires, sidebrace, parts of the door and the junction between the cylinder and sidebrace.

Four Wheel Landing Gear Measurements

Lazos [76, 77] conducted the aerodynamic experimental analysis of the Boeing 757 main landing gear on a 31% scale simplified model at Mach number below 0.1 in the NASA BART wind tunnel. The main aim of this experiment was to obtain results from a series of 160 PIV data sites from between the wheels and in the wake. The experiments highlighted that the vortex is generated by the asymmetry caused by the presence of the main strut, and oscillates between the front and rear wheels. Lazos suggested that this mid-wheel vortex interacting with wheel surfaces could be a potential noise source. However, the lack of unsteady experimental data meant that comparisons with unsteady simulations are not available.

Six Wheel Landing gear Measurements

Ringshia et al. [78] performed aerodynamic experiments on a high fidelity 13% scale and 26% scale Boeing 777 main landing gear model in the Virginia Tech Stability Wind Tunnel (VT-SWT) at a Mach number of 0.16. The study highlighted the flows between the front and middle wheels with a recirculation region. The PIV results show vortex shedding from the front wheel and impinging on the middle wheels, which was considered as the source of interaction noise. The acoustic measurement on the 13% scale high fidelity Boeing 777 main landing gear model was conducted by Ravetta et al. [67] in VT-SWT, in order to identify the noise sources using a phased microphone array.

2.3.5. Empirical Methods for Landing Gear Noise

The first empirical landing gear noise prediction model was developed by Fink [79] based on both flight-test data and simplified generic scale model wind tunnel test data. The prediction model only requires the number of wheels, the wheel diameter and the length of the main strut as the major parameter inputs, assuming that the whole sound level spectrum is determined by the major components of the landing gear. Separate predictions are made for the strut and wheel noise, which are summed to give the total landing gear noise. The Strouhal scaling approach is introduced in the model for general applications regardless the landing gear scale. This simple model only uses the

dimensions of the largest components, thus significantly underestimate high-frequency noise levels.

Smith and Chow [80] established a model incorporating aeroacoustic theories. This model breaks down the gear into its major components, compute sound intensities according to the dimensions and orientation with respect to an observation location, and at the end sum up the noise intensities from all components to provide the overall sound level spectrum. The estimated sound intensities from individual components are based on Curle's theory [18], which scale to the six power of flow velocity and the square of the source characteristic dimension, assuming dipole-type noise sources. This model only considers components of primary structure. The small scale components are accounted for in the prediction via a user defined dressing factor. The capability of this empirical tool has been proved in the prediction of the noise reduction potential from a low-noise redesign of gear components [81].

Similar noise prediction approaches were developed by Guo et al. [82] and Guo [70], validated by data from both full scale wind tunnel and flight test. Guo's tool distinguishes between three sets of gear components: large, medium and small scale elements, responsible for low-, medium- and high-frequency noise contributions respectively. Similar to Smith's dressing factor, a complexity factor is defined to account for the high-frequency noise contributions from small structures. Guo's method was developed in terms of narrowband spectrum without Strouhal scaling approach, therefore only applicable to full scale landing gear.

The Aircraft Noise Prediction Program (ANOPP) of NASA, which originally relied on the Fink method only, now is combining the methods from both Fink and Guo to improve the prediction accuracy [83]. It is recommended to use Guo's method for full scale landing gear noise prediction, but to use Fink's method with scaled model due to its Strouhal number dependency.

The empirical prediction models usually requires lots of calibrations against existing test data, and therefore has limited reliability on predicting noise from unconventional gear architectures at the design stage. Computational methods for landing gear noise prediction could in principle be general tools with increases in computational power. Such methods could be applied to any novel landing gear geometry because they do not need to be calibrated against existing test results.

2.3.6. Computations of Landing Gear Noise

Two Wheel Landing Gears

Imamura et al. [84] performed both steady and unsteady computations on a PAX-100 two-wheel landing gear geometry, called Landing gear noise Evaluation Geometry (LEG). Measurement data are available for the comparison study through the wind tunnel experiments performed by Japan Aerospace Exploration Agency (JAXA) [75]. The purpose of the steady-state simulations is to investigate the mean flow patterns around the landing gear. The 40% scale LEG model with considerable details was computed on unstructured grids of 6.9 million cells for the closed wind tunnel case and 10.2 million cells for the open jet wind tunnel case, which were built up by the unstructured mesh generator MEGG3D. This allows for the effects of wind tunnel walls to be investigated. The flow solver is J-TAS code originally developed at Tohoku University. Three-dimensional RANS are solved on unstructured grid by a finite volume method, and S-A one equation model is chosen as the turbulence model. The simulation was performed at 68 m/s with a Reynolds number of 1.8×10^{6} based on the wheel diameter. It was found that accelerated and decelerated regions existed in the narrow area between two tires and flow-body interaction occurred between the cylinder and side-brace, which could be the potential noise sources.

The computational geometry in the unsteady simulation is a heavily simplified 40% scale LEG model. Block-structured grids are generated using commercial software Gridgen [85] with approximately 26 million grid points in total. The unsteady flow solver is developed based on UPACS code which is an in-house CFD code in JAXA, and employing a finite volume method on multi-block structured grids solving three-dimensional compressible N-S equations. The convection terms are discretized using 6th-order compact scheme, and the viscous terms are discretized using 2nd-order central scheme. Second-order time integration is performed using a time step 2.5×10^{-3} seconds. The Smagorinsky SGS model is used as a sub-grid scale model, and van Driest damping is applied at the wall boundary of the LES region. The filter technique is employed with 6th-order accuracy to avoid numerical instability. The LES computation seemed to be not resolving boundary layer sufficiently compared to the previous RANS results. The author suggested that this might be improved by choosing LES/RANS hybrid method in the future work. Far field noise is predicted using the FW-H method on three permeable

surfaces with the domain, shown in Fig. 2.6. The downstream surface is excluded from the permeable surface to remove artificial acoustic wave generated by density fluctuation due to strong vortex convection. The estimated far field noise shows reasonably good agreement with the experimental results up to 1 kHz, shown in Fig. 2.7. The differences among different permeable surface locations are small which indicates the reliability in the estimation procedure.

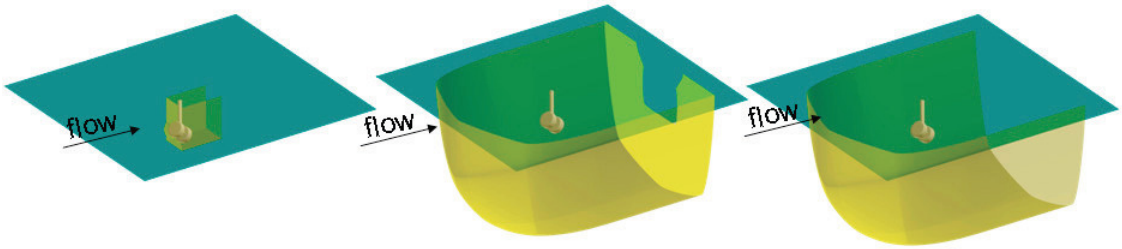

Figure 2.6: FW-H integration surfaces as used by Imamura et al. [84].

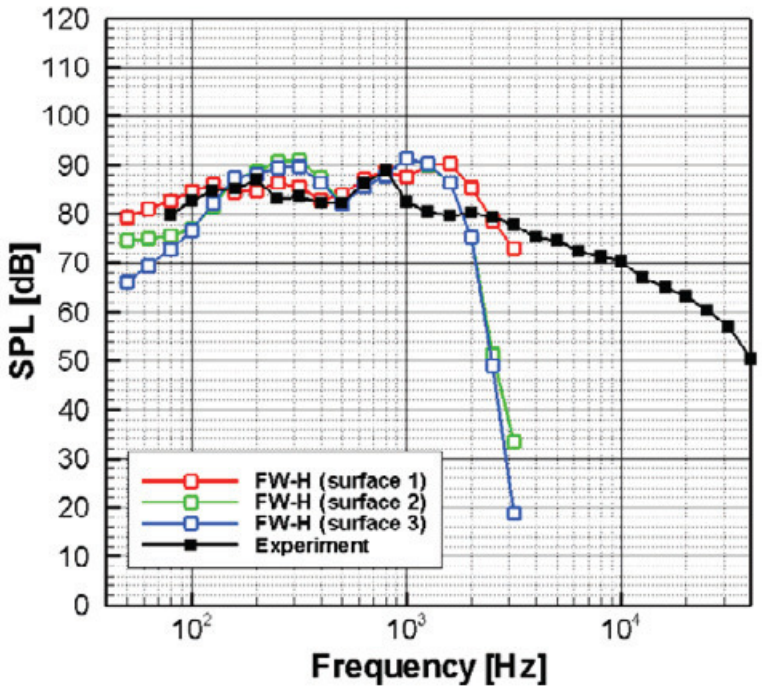

Figure 2.7: Far field noise comparisons of a two wheel PAX-100 landing gear [84].

A joint project was proposed by NASA and the Gulfstream Aerospace Company on benchmark problems for airframe noise computations (BANC). The NLG was chosen in preference to an MLG because of significant installation effects caused by proximity to

the wing with deployed flaps. Two configurations of a partially and fully dressed landing gear will allow increasing geometry complexity into the future. In BANC-I 2010 conference, several computational works have been discussed based on the 25% scale Gulfstream G550 nose landing gear model.

Van de Ven et al. [5] was one of the computational submissions using the commercial Navier-Stokes finite volume CFD solver STAR-CCM+. The solver is fully unstructured and employs second-order discretizations in both space and time. A series of unstructured grids of up to 58 million cells were built with the built-in grid generation tool in the solver. The k-ω SST based Delayed Detached Eddy Simulation (DDES) was performed with time step size of 2×10^{-5} second (50 kHz sampling rate). A larger time step size of 1×10^{-4} second was also used in the simulation to improve the low frequency predictions. From the steady solution, static pressure on the surface of the wheel was compared against the measurement locations from the NASA BART experiment. The results show a consistent 0.1 psi difference around the whole wheel. The unsteady pressure data monitored at identical locations to those measured at BART and UFAFF wind tunnels were then compared to the measurement data in the form of power spectral density (PSD). Good agreements had been achieved up to approximately 5 kHz. Far field acoustic predictions were not made, but might be attempted with FW-H tools in the future work.

Dethuioux et al. [86] applied the Lattice Boltzmann solver PowerFLOW 4.2 on the same Gulfstream G550 geometry. It is an explicit solver which uses a DDES turbulence method based on the RNG k-ε model. The voxel based meshes were generated automatically by the built-in PowerFLOW grid generation tool with four-stage refinement. The finest mesh consists of 52.4 million voxels with a 0.25 mm voxel size. This manages to achieve a 4 kHz cut-off frequency on the surface pressure PSD comparisons. The mean velocity and vorticity results compared with the PIV measurement show general agreement with discrepancies in the flow separation regions which were considered to be caused by the fully turbulent model without transition treatment. The far field noise prediction was obtained with a FW-H solver using the solid surface data, which showed the same shape in the middle frequency range with 5dB under-prediction level, see Fig. 2.8. The author suggested that the using a permeable integration surface and higher sampling frequencies may help improve the far field noise predictions.

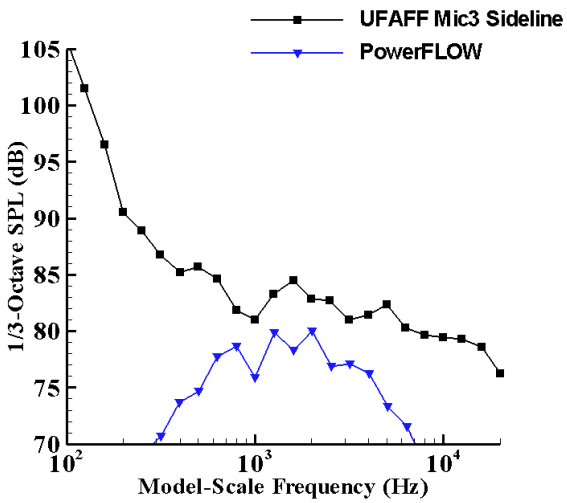

Figure 2.8: Far field noise comparisons of a 25% scale Gulfstream NLG using PowerFLOW 4.2 [86].

Ueno et al. [87] used a high-order Pseudo DNS code Cflow (in-house code of Kawasaki heavy industries, Ltd.) to analyze the Gulfstream G550 geometry. The Cflow code solves three dimensional compressible N-S equations with seventh-order spatial discretization. The implicit time integration was performed with the time step size of 5.9×10^{-7} second. The unstructured mesh consists of 36.7 million cells with 1.7 million surface grids, which was generated automatically in the solver. Steady surface pressures are compared with wind tunnel measurement data, showing differences around the flow separation regions. The author suggested that the discrepancies could be the effect of grid reduction. Unsteady surface pressure at the probes are also compared with measurement in the form of PSD, showing a cut-off around 2-3 kHz. The mean velocity levels in the wake are under-predicted by 5m/s with general wake shape captured. The direct calculation of the far field noise has agreement with measurement up to 2 kHz, depicted in Fig. 2.9. The far field prediction using Curle's acoustic analogy is extended to high frequencies with good accuracy, which suggests that sufficient grid resolution is obtained in the near field region.

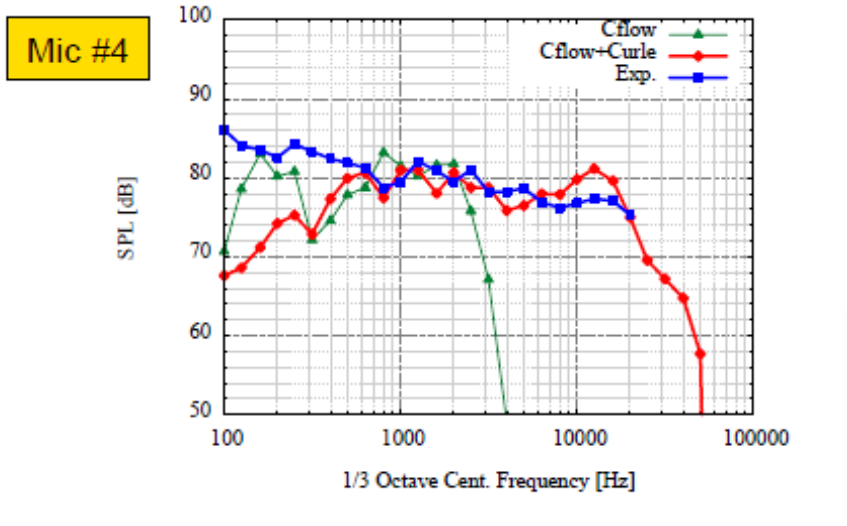

Figure 2.9: Far field noise comparisons of a 25% scale Gulfstream NLG using Cflow code [87].

Vasta et al. [6] conducted aeroacoustic simulations on the Gulfstream G550 model using the NASA unstructured node-based flow solver FUN3D, which is second-order accurate in both space and time. A set of three successively finer unstructured grids comprised of approximately 9, 25, and 71 million nodes were generated using the VGRID grid generation software. A locally enriched 47 million cell grid was also produced with refinement in key areas. The computations were performed at M=0.166 and a Reynolds number of 7.3×10^4 based on the main strut diameter. Two different turbulence models HRLES (hybrid RANS/LES) and MDDES (modified Delayed Detached Eddy Simulation) were attempted in the simulations, which provided results with small differences. Significant improvement in time-averaged surface pressure and power spectral density comparisons with the experimental data is observed with grid refinement, shown in Fig. 2.10. The best PSD comparisons are obtained for the surface of the door, where a cut-off frequency of around 3 kHz is achieved. The spanwise time-averaged vorticity contours are in good agreement with the PIV data, but the 2D TKE (turbulent kinetic energy) levels are over-predicted. The grid refinement has only a minor effect on these results. The far field noise calculation was attempted using FW-H predictions with solid surface data, see Fig. 2.11. In general, the predicted levels show a deep drop-off in SPL (sound pressure level). The drop-off frequency increases with the grid refinement, which improves the comparison with measured data for finer grids.

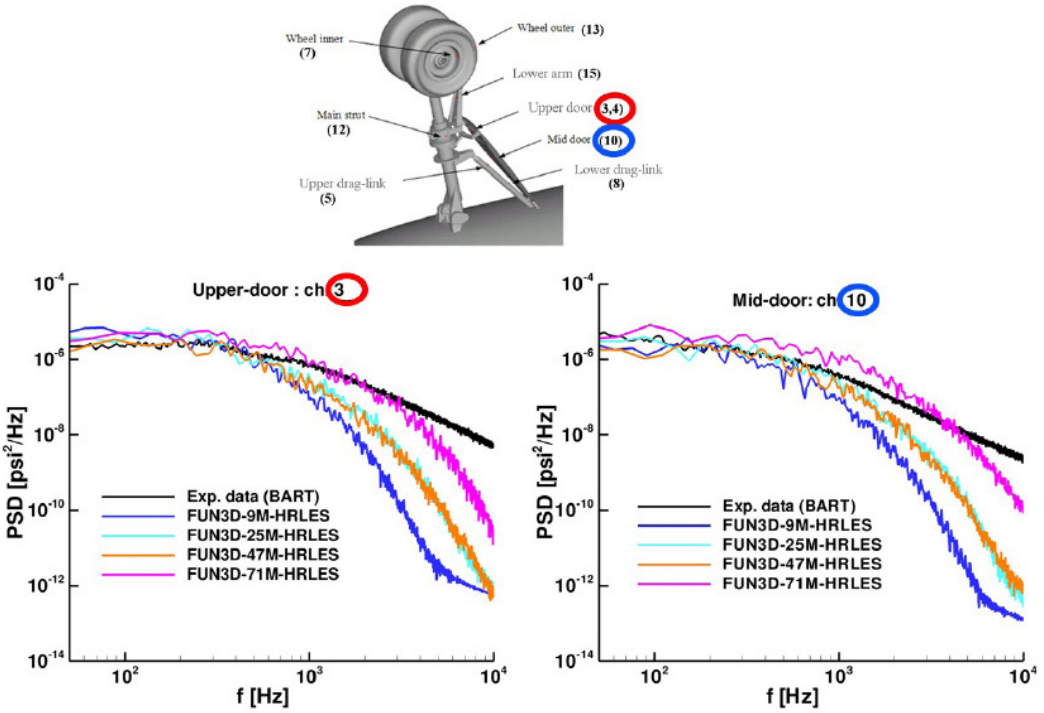

Figure 2.10: Effect of grid refinement on PSD of a NLG simulation using FUN3D [6].

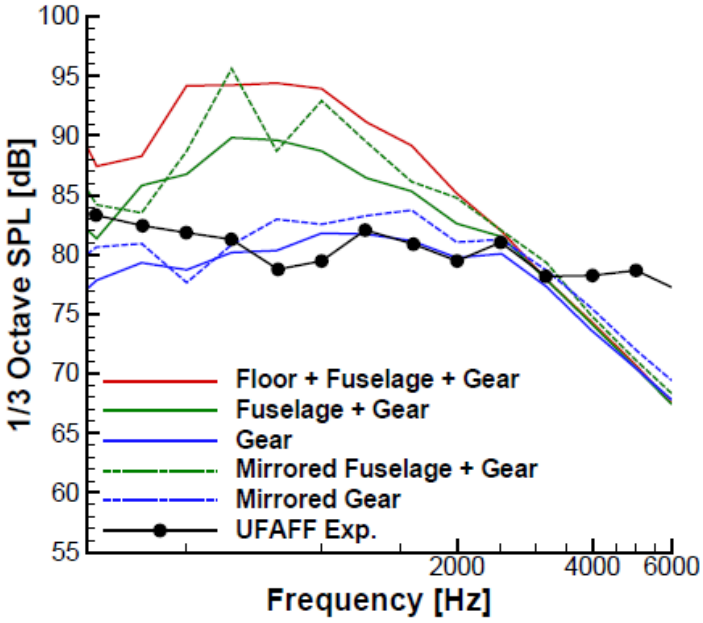

Figure 2.11: Far field noise prediction using FUN3D with 71 million cells [6].

Four Wheel Landing Gears

The simplified 31% scale Boeing 757 main landing gear model was numerically investigated by Hedges et al. [4] in 2002. The flow around the landing gear was

modeled as incompressible and at a Reynolds number, based on wheel diameter of 6×10^5. The computations were performed with the NTS code solving the incompressible N-S equations with fourth-order spatial schemes and second-order implicit time schemes. The time step size is 0.03, normalized with inflow velocity and wheel diameter. Both URANS and DES based on the same S-A turbulence model were attempted and compared to each other with a multi-block structured grid with approximately 2.5 million points. Comparison to Lazos' experiments shows that the simulations predict the pressure over the surface of the wheels with reasonable accuracy considering the presence of bluff bodies and separated regions. Flow features and the surface pressure levels are all in good agreement. The computational simulation not only characterizes the mean flow features around landing gear model, but also investigates the instantaneous flow fields. The two time-averaged flow field are similar, though the DES shows more turbulence intensity overall. The instantaneous flow fields are however, very dissimilar. DES was suggested to be more promising for noise prediction, though no aeroacoustic simulations were conducted.

Souliez et al. [56] investigated the aerodynamic noise from Boeing 757 main landing gears using unstructured grids. Two geometric configurations were tested in order to assess the impact of two lateral struts on the sound level and directivity in the far field. The first baseline grid uses 880k unstructured volume cells and the second more complex grid with additional struts uses 1.2 million unstructured cells, both of which were generated using Gridgen [85]. In this study the compressible N-S equations were solved with the finite volume, Runge-Kutta time-marching code PUMA (Parallel Unstructured Maritime Aerodynamics) with no RANS or LES model. The free stream Mach number is 0.2, and the Reynolds number is 1.23×10^6 based on the wheel diameter. The time step for the first grid is 0.86×10^{-8} second, and 1.9×10^{-8} second for the second grid. The aerodynamic noise was computed with the FW-H integrals using both the solid surface and a permeable surface away from the landing gear. Excellent agreement was obtained in the near field between permeable FW-H surface predictions and the CFD results, which indicates that the volume sources cannot be ignored in the near field. For the far field noise the difference between two FW-H solutions decreases as observing distance increases, which suggests that volume sources are of short range. No comparisons with experimental data were made in this study.

Li et al. [88] performed URANS computations for a relatively complex Boeing 757 main landing gear assembly. It consists of four wheels, two diagonal struts, an oleo-

strut, a side-door attached to the oleo, yokes/pin and other structures that join the system together. A flat plate is attached to the top-end of the oleo and struts, which is meant to represent the aircraft wing. Li's work was aimed at understanding the flow field associated with a representative MLG configuration, therefore attempted no aeroacoustic computations. The flow solver is CFL3D developed at NASA, employing the two equation k-ω turbulence model. The flow conditions are identical to those used in Souliez's simulations [56]. The time step is 0.01, normalized with sound speed and the wheel diameter. The constructed grid consists of 155 blocks with a total of 13.3 million grid points. The unsteady flow structures, such as flow separations, vortices shedding off the bluff bodies, and flow-surface interactions, were studied and compared to the experiment results obtained by Lazos. Results show an asymmetrical flow caused by the asymmetry of the geometry with only one side having diagonal struts, and a strong interaction mechanism between components on the landing gear.

Lockard and Khorrami [13, 89] undertook consecutive computational simulations and investigated the contribution of each gear component to overall landing gear noise using a 10% simplified main landing gear model in 2003 and 2004. The model geometry and the flow solver are those in CFD simulation performed by Li et al. [88]. The reference length scale is the gear wheel diameter (0.09398 m), and the free-stream Mach number is 0.2. The Reynolds number based on the wheel diameter is 1.23×10^6. URANS equations were solved using structured grids consisting of 155 blocks possessing a total of 1.8 million grid points in 2003's simulation, while the later calculation increased the resolution to a higher level of 13.3 million grid points. The FW-H equation was solved to predict the noise at far field observer locations. Noise predictions using the permeable surfaces appeared to be contaminated by errors by large wake fluctuations passing through the surfaces [57]. However, solid surface FW-H solutions are in good agreement with the near field CFD solutions giving confidence in the far field results. It is believed that bluff body separation and the formation of vortex structures are often responsible for the strong fluctuations. Vortex shedding off various components is expected to be a primary source of noise for landing gears.

A four-wheel "rudimentary" landing gear was introduced by Spalart et al. [90], with relatively simple and manageable geometry for current numerical simulations. Detached-Eddy Simulations (DES) was performed using up to 18 million points in the high-order NTS code. The grids contain 14 structured blocks of 10 million cells in the wind tunnel section and 16 structured blocks of 18 million cells in free air. The non-

dimensional time step is 5×10^{-3}. Far field noise predictions were performed by coupling the DES and a FW-H calculation. The results include force, wall pressure, and noise spectra. The wall pressure signals in wind tunnel simulation and free air simulation are quite similar, suggesting that the existence of wind tunnel wall has slight effect on the flow. In the absence of the noise experimental data, the attention was focused on the internal quality check, in particular by varying the permeable FW-H surface (e.g. using solid surface, or open permeable surface). It was found that the difference ranges from 4 to 7 dB in SPL between solid and permeable surfaces, which might be due to the neglection of quadruple sources enclosed in the permeable surface. However, the interfaces inside the permeable FW-H surface have significant changes in grid spacing, and could result in numerical errors in far field noise predictions. Khorrami and Lockard [91] also found the grid block interface induced errors in their FW-H predictions.

Dobrzynski et al. [92] conducted computations on CAD models of both A340 nose landing gear and main landing gear, to design low noise landing gear configurations for future aircraft. The Reynolds number for these computations is 1.25×10^{6} with a Mach number of 0.2. The commercial software package Centaur [93] was applied for hybrid grid generation. In the hybrid grid, a number of 20 prism layers are assigned to simulate the boundary layer with first spacing of 0.1. For the NLG a total of 270k and for the MLG a total of 390k surface grid points are used. The corresponding numbers of volume cells are about 4 million and 8 million, respectively. The computations were performed with the finite volume CFD code Tau (developed by German aerospace center DLR), to solve the Reynolds-averaged Navier-Stokes equations using S-A turbulence model. The computational design was performed in an iterative process until the critical areas of high speed turbulent flow interaction with downstream gear components was eliminated. Because of the limited number of gird points, the direct comparison between CFD results and experimental data is impossible. The calculated local flow data were used in a semi-empirical prediction model [81] to estimate the noise radiations. The noise model indicated that the reductions of -6.5 dB for the NLG and -5.7 dB for the MLG would be achieved for the optimized designs.

Summary of Landing Gear Simulations

Previous researches in the aeroacoustic computations of landing gear geometry show that finite volume methods were widely attempted to cope with the complex landing

gear geometries, and required large amount of unstructured grid points to obtain reasonable acoustic results. The current knowledge from aerodynamic and aeroacoustic calculations show that separated flows around complex geometries and flow-surface interactions could be the potential noise sources. Thus, accurate unsteady solutions preserving more flow details are required to obtain reliable noise results. URANS is commonly used in many researches, but DES (and DDES) seems to be able to provide more accurate instantaneous flow perturbations. Far field noise prediction using the solid surface sources shows good results. The permeable surface FW-H solution is not always reasonable due to the interference of strong waves. Summaries of computational studies on two wheel and four wheel landing gear geometries are listed in Table 2.1 and 2.2.

Table 2.1: Summery of computational studies on two wheel landing gear geometries.

Authors	Geometry	Mesh	Flow solver	Acoustics	Validation
Imamura et al. [84]	40% scale LEG	Unstructured up to 10.2M	J-TAS RANS(S-A)	None	JAXA WT
Imamura et al. [84]	40% scale simplified LEG	Structured 26M	UPACS LES	FW-H	JAXA WT
Van de Ven et al. [5]	25% scale Gulfstream G550	Unstructured 58M	STA-CCM+ DDES(k-ω SST)	Surface pressure PSD	BART & UFAFF WT
Dethuioux et al. [86]	25% scale Gulfstream G550	Voxels 52.4M	PowerFLOW DDES(RNG k-ω)	Surface pressure PSD & FWH	BART & UFAFF WT
Ueno et al. [87]	25% scale Gulfstream G550	Unstructured 36.7M	Cflow Pseudo DNS	Surface pressure PSD & Curle's	BART & UFAFF WT
Vasta et al. [6]	25% scale Gulfstream G550	Unstructured up to 71M	FUN3D HRLES/MDDES	Surface pressure PSD & FWH	BART & UFAFF WT

Table 2.2: Summery of computational studies on four wheel landing gear geometries.

Authors	Geometry	Mesh	Flow solver	Acoustics	Validation
Hedges et al. [4]	Simplified 31% scale B757 MLG	Structured 2.5M	NTS code URANS (S-A)&DES (S-A)	None	BART WT
Souliez et al. [56]	Boeing757 MLG	Unstructured up to 1.2M	PUMA	FW-H	None
Li et al.[88]	10% Boeing 757 MLG	Structured 13.3M	CFL3D URANS (k-ω)	None	BART WT

Lockard et al. [13, 89]	10% Boeing 757 MLG	Structured 1.8M &13.3M	CFL3D URANS (k-ω)	FW-H	BART WT
Spalart et al. [90]	Rudimentary MLG	Structured 18M	NTS code DES	FW-H	None
Dobrzynski et al. [92]	A340 NLG&MLG	Hybrid 4M&8M	DLR Tau RANS(S-A)	None	DNW WT

2.3.7. Landing Gear Noise Reduction Strategy

The knowledge from various wind tunnel experiments suggests that noise reduction could be achieved by either reducing the number and complexity of components exposed to the incoming flow or avoiding the wake-body interaction with downstream components. The development of noise reduction concepts distinguishes between the application to existing landing gears and future new gear architectures. In the first case, only add-on fairings could be used to cover complex gear structures, while in the second case the landing gear structures could be optimized for low aerodynamic noise generation.

Streamlined add-on fairings have been extensively tested to protect complex gear elements from high speed inflow in numerous wind tunnel experiments [94]. Examples of such add-on fairings are depicted in Fig. 2.12.

Figure 2.12: Examples of landing gear add-on fairings [1].

The under-tray fairings were designed for A340 landing gears to cover the bogie area from the flow. Wind tunnel tests indicated a noise reduction potential in the order of 3dBA for such kinds of fairings, and Flight tests achieved a 2EPNdB (effective perceived noise level) reduction. Similar approach was followed by NASA and Boeing with toboggan for the six-wheel Boeing 777 MLG [95]. Add-on fairings can also an adverse effect, which is a noise increase due to the flow alterations enforced by the fairings and the corresponding increase in the local impinging velocity to the downstream gear components. To overcome this problem, the next generation of fairings was manufactured with flow transparent materials, such as meshes or elastic cloth [68, 96, 97].

The design of low noise landing gear can be supported by the use of empirical noise prediction models as well as numerical simulations. Three-dimensional flow field calculations help to identify and potentially avoid local flow separations and the impingement of high speed flow onto critical gear structure components. Such a low noise design was studied in the European project Significantly Lower Community Exposure to Aircraft Noise (SILNCER) [92]. For the NLG the major improvements are related to a deployable spoiler to protect the upper gear leg from high speed inflow, and the inverted steering mechanism which hides complex steering systems from the flow,

shown in Fig. 2.13(a). The low noise MLG, depicted in Fig. 2.13(b), has new designs of side-stay and leg door with aerodynamic considerations. The brakes are protected from high speed inflow and the bogie is aligned with the inflow direction. Subsequent wind tunnel tests revealed a noise reduction potential in the order of up to 7 dBA in the mid frequency range for the advanced gear design.

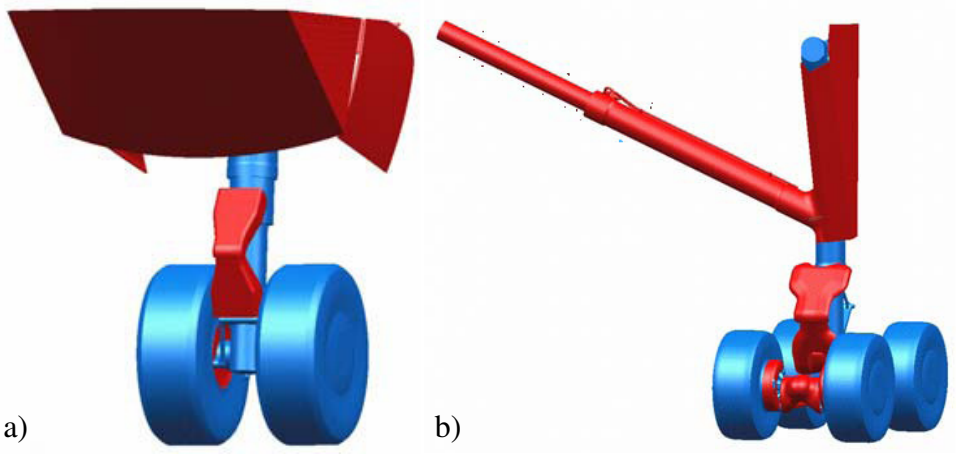

Figure 2.13: Advanced low noise A340 landing gear design of a) NLG; b) MLG.

Flow control is the last member in the development chain toward low noise landing gears. It might be used to locally reduce flow separation and unsteady wake shedding off single struts. There are both passive control methods (e.g., splitter plates, truncation of cylinders) [98, 99] and active methods such as blowing and plasma actuation [100, 101]. The low noise gear design has to take some important constraints into account, regarding flight operation, safety, and cost. For example, active control technologies inherently increase the system complexity in operation and cost. Therefore, the noise benefits from active control must be verified before a practical application on an aircraft.

Chapter 3
Numerical Methods

3.1. Introduction

SotonCAA is a Fortran-based code package providing numerical solutions to general CFD/CAA problems, and is capable of dealing with complex geometries using multi-block structured grids. A feature of SotonCAA is the embedded high-order high resolution numerical schemes [34, 35]. Because of this, it is able to directly calculate the sound field characteristics in the near field with high accuracy. Furthermore, it is capable of solving different fluid governing equations such as Navier-Stokes equations (DES and URANS), linearized Euler's equation, and acoustic perturbation equations. The code structure is based on a series of modules, in order to maximize the maintainability and expansion possibilities. A benefit of this structure is the convenience to implement new schemes to the rest of the code, which can evolve easily over time. The disadvantage of this is that the code has grown rather complex with increasing number of subroutines.

Prefactored, compact finite-difference scheme (6th-order) proposed by Hixon [34] is employed in the code package and optimized by Ashcroft, et al. [35] in preference to improve dispersion characteristics. Finite difference filtering schemes are optional with 2nd-order, 6th-order and 10th-order central schemes coupled with biased boundary schemes of reduced order. Time integration, uses a low storage, low dispersion and dissipation Runge-Kutta (LDDRK) [37] scheme which is 4th-order accurate 4-6 stage explicit scheme. An implicit 2nd-order time-accurate LU-SGS method [102] has been introduced into SotonCAA by Ma, et al. [103]. There are several selectable non-reflecting boundary conditions implemented in SotonCAA in order to perform acoustic calculations. As mentioned before, buffer zone schemes are preferred due to its excellent performance with non-linear flows and the easy way of implementation. In SotonCAA, structured grids are required for use of numerical calculations with high-order accurate solutions. In order to improve the numerical stability in multi-block

junctions, we implement a characteristic interface condition proposed by Kim and Lee [104]. Turbulence models are selectable and treated in a modular manner so that additional models are easy to be added on. At the moment, SotonCAA turbulence treatments include URANS (with S-A) [9], Large Eddy Simulation (LES) [110], and Detached Eddy Simulation (DES) [4].

For aeroacoustic calculations, a time domain radiation model is employed in SotonCAA package to determine the far field sound properties. In support of aeroacoustic simulations, the polynomial interpolation code 'CFDtoFWH' is developed to transform CFD flow information to acoustic sources on the user defined integration surface. The raw data output from CFD calculation are treated with appropriate coordinate translation before being stored for the aeroacoustics solver. The far field observer positions and the shape of the integration surface are determined independently without interfering with both solvers.

Initial numerical parameters required for CFD/CAA calculation must be specified through 'input file', 'grid file' and 'parameters file'. The input file specifies flow conditions of the simulation and boundary condition specifications for each block. The grid file contains the grid-point coordinate information generated by the commercial grid generating software, e.g. Gridgen [85]. The parameter file contains user defined parameters such as turbulence options and output format options. The code is portable across all platforms with Fortran 90 and MPI installed, including windows and UNIX machines. The output can be displayed via both text files and commercial software such as Tecplot [106].

In the following sections, details of the numerical implementations used in the research are presented. Section 3.2 describes the governing equations in the noise generating flow field. Difference schemes are introduced in section 3.3, 3.4, and 3.5. DES turbulence model is presented in section 3.6, and grid generation issues can be found in section 3.7. Boundary related problems are discussed in section 3.8 and 3.9. Parallel computing strategy is presented in section 3.10. Section 3.11 explains the radiation model that is implemented to calculate the acoustic field, followed by the summary of the numerical methods in section 3.12.

3.2. Governing Equations

The three-dimensional conservative form Reynolds averaged Navier-Stokes equations are solved in SotonCAA, which is represented in Cartesian coordinates as

$$\frac{\partial Q}{\partial t}+\frac{\partial E}{\partial x}+\frac{\partial F}{\partial y}+\frac{\partial G}{\partial z}=S_V, \tag{3.1}$$

where the conservative variables and the inviscid flux vectors are given below

$$\begin{aligned} E&=\left[\rho u,\rho u^2+p,\rho vu,\rho wu,(\rho e_t+p)u\right]^T,\\ F&=\left[\rho v,\rho uv,\rho v^2+p,\rho wv,(\rho e_t+p)v\right]^T,\\ G&=\left[\rho w,\rho uw,\rho vw,\rho w^2+p,(\rho e_t+p)w\right]^T, \end{aligned} \tag{3.2}$$

and S_V is a source term that consists of the viscous flux derivatives

$$S_V=\frac{\partial E_V}{\partial x}+\frac{\partial F_V}{\partial y}+\frac{\partial G_V}{\partial z}, \tag{3.3}$$

where the viscous flux vectors, the stress tensor components, and the heat fluxes are given as

$$\begin{aligned} E_V&=\left[0,\tau_{xx},\tau_{xy},\tau_{xz},u\tau_{xx}+v\tau_{xy}+w\tau_{xz}+q_x\right]^T,\\ F_V&=\left[0,\tau_{yx},\tau_{yy},\tau_{yz},u\tau_{yx}+v\tau_{yy}+w\tau_{yz}+q_y\right]^T,\\ G_V&=\left[0,\tau_{zx},\tau_{zy},\tau_{zz},u\tau_{zx}+v\tau_{zy}+w\tau_{zz}+q_z\right]^T,\\ \tau_{xx}&=\frac{1}{\mathrm{Re}_\infty}(2\mu\frac{\partial u}{\partial x}+\lambda\nabla\cdot\vec{V}),\\ \tau_{xx}&=\frac{1}{\mathrm{Re}_\infty}(2\mu\frac{\partial u}{\partial x}+\lambda\nabla\cdot\vec{V}),\\ \tau_{zz}&=\frac{1}{\mathrm{Re}_\infty}(2\mu\frac{\partial w}{\partial z}+\lambda\nabla\cdot\vec{V}), \end{aligned}$$

$$\tau_{xy} = \tau_{yz} = \frac{\mu}{\mathrm{Re}_\infty}(\frac{\partial u}{\partial y} + \frac{\partial v}{\partial x}),$$

$$\tau_{yz} = \tau_{zy} = \frac{\mu}{\mathrm{Re}_\infty}(\frac{\partial v}{\partial z} + \frac{\partial w}{\partial y}),$$

$$\tau_{zx} = \tau_{xz} = \frac{\mu}{\mathrm{Re}_\infty}(\frac{\partial w}{\partial x} + \frac{\partial u}{\partial z}),$$

$$q_x = \frac{\mu}{(\gamma-1)P_r \mathrm{Re}_\infty M_\infty}\frac{\partial T}{\partial x},$$

$$q_y = \frac{\mu}{(\gamma-1)P_r \mathrm{Re}_\infty M_\infty}\frac{\partial T}{\partial y},$$

$$q_z = \frac{\mu}{(\gamma-1)P_r \mathrm{Re}_\infty M_\infty}\frac{\partial T}{\partial z}. \tag{3.4}$$

The total energy per unit mass is defined as

$$e_t = \frac{p}{(\gamma-1)\rho} + \frac{u^2+v^2+w^2}{2}. \tag{3.5}$$

For practical CFD/CAA with finite difference schemes, the partial differential equations are solved in the transformed domains with generalized coordinates, which is given as

$$\frac{\partial \hat{Q}}{\partial t} + \frac{\partial \hat{E}}{\partial \xi} + \frac{\partial \hat{F}}{\partial \eta} + \frac{\partial \hat{G}}{\partial \zeta} = \hat{S}_V, \tag{3.6}$$

where the caret indicates the transformed properties. The vectors of the conservative variables in the generalized coordinates can be represented as

$$\hat{Q} = \frac{Q}{J},$$

$$\hat{E} = \frac{\xi_x E + \xi_y F + \xi_z G}{J},$$

$$\hat{F} = \frac{\eta_x E + \eta_y F + \eta_z G}{J},$$

$$\hat{G} = \frac{\zeta_x E + \zeta_y F + \zeta_z G}{J}. \tag{3.7}$$

In Eq. (3.7) the transformation Jacobian and the grid matrices are given by

$$J = 1/[x_\xi(y_\eta z_\zeta - y_\zeta z_\eta) + x_\eta(y_\zeta z_\xi - y_\xi z_\zeta) + x_\zeta(y_\xi z_\eta - y_\eta z_\xi)], \tag{3.8}$$

With

$$\begin{pmatrix} \xi_x & \xi_y & \xi_z \\ \eta_x & \eta_y & \eta_z \\ \zeta_x & \zeta_y & \zeta_z \end{pmatrix} = J \begin{pmatrix} y_\eta z_\zeta - y_\zeta z_\eta & z_\eta x_\zeta - z_\zeta x_\eta & x_\eta y_\zeta - x_\zeta y_\eta \\ y_\zeta z_\xi - y_\xi z_\zeta & z_\zeta x_\xi - z_\xi x_\zeta & x_\zeta y_\xi - x_\xi y_\zeta \\ y_\xi z_\eta - y_\eta z_\xi & z_\xi x_\eta - z_\eta x_\xi & x_\xi y_\eta - x_\eta y_\xi \end{pmatrix}. \tag{3.9}$$

3.3. Spatial Discretization

The finite-difference approach is employed in the spatial discretization of the governing equations. This choice is motivated by the relative ease of formal extension to higher-order accuracy, low operation count and general flexibility. Following Lele [32], a general compact approximation to the first spatial derivative ($\partial f/\partial x$) may be written in the form

$$\beta D_{i-2} + \alpha D_{i-1} + D_i + \alpha D_{i+1} + \beta D_{i+2} = c\frac{f_{i+3} - f_{i-3}}{6\Delta x} + b\frac{f_{i+2} - f_{i-2}}{4\Delta x} + a\frac{f_{i+1} - f_{i-1}}{2\Delta x}, \tag{3.10}$$

where D_i is the spatial derivative of the function f. The relations between the coefficients a, b, c, α and β are derived by matching the Taylor series of various orders. The first unmatched coefficient determines the formal truncation error of the approximation. These relations are

$$a + b + c = 1 + 2\alpha + 2\beta \text{ (Second order)},$$

$$a + 2^2 b + 3^2 c = 2\frac{3!}{2!}(\alpha + 2^2\beta) \text{ (Fourth order)},$$

$$a + 2^4 b + 3^4 c = 2\frac{5!}{4!}(\alpha + 2^4\beta) \text{ (Sixth order)},$$

$$a+2^6 b+3^6 c=2\frac{7!}{6!}(\alpha+2^6\beta) \text{ (Eighth order),}$$

$$a+2^8 b+3^8 c=2\frac{9!}{8!}(\alpha+2^8\beta) \text{ (Tenth order).} \tag{3.11}$$

Only the eighth-order tri-diagonal ($\beta = 0$) and the tenth-order pentadiagonal ($\beta \neq 0$) schemes have unique coefficients. The other lower-order schemes have free coefficients that are not determined until more constraints are imposed or the stencil size is reduced. Both Hixon's [34] and Ashcroft's [35] compact schemes consider only tri-diagonal systems ($\beta = 0$). One example of this type of compact scheme with 6th-order accuracy can be written as

$$\frac{1}{5}(D_{i+1}+D_{i-1})+\frac{3}{5}D_i=\frac{1}{\Delta x}\left[\frac{1}{60}(f_{i+2}-f_{i-2})+\frac{14}{30}(f_{i+1}-f_{i-1})\right]. \tag{3.12}$$

The numerical wave-number of the generic compact derivative defined in Eq. (3.10) is determined by using Fourier analysis. The Fourier transform and its inverse are related by

$$\tilde{f}(\kappa)=\frac{1}{2\pi}\int_{-\infty}^{\infty} f(x)e^{-i\kappa x}d\kappa,$$

$$f(x)=\int_{-\infty}^{\infty}\tilde{f}(\kappa)e^{-i\kappa x}dx. \tag{3.13}$$

Taking the Fourier transform of both sides of Eq. (3.10), we find

$$i\kappa\tilde{f}=\frac{i}{\Delta x}\left(\frac{a\sin(\kappa\Delta x)+(b/2)\sin(2\kappa\Delta x)+(c/3)\sin(3\kappa\Delta x)}{1+2\alpha\cos(\kappa\Delta x)+2\beta\cos(2\kappa\Delta x)}\right)\tilde{f}. \tag{3.14}$$

Comparing the two sides of the above equation it is clear that

$$\kappa'=\frac{1}{\Delta x}\left(\frac{a\sin(\kappa\Delta x)+(b/2)\sin(2\kappa\Delta x)+(c/3)\sin(3\kappa\Delta x)}{1+2\alpha\cos(\kappa\Delta x)+2\beta\cos(2\kappa\Delta x)}\right). \tag{3.15}$$

which is the numerical wave-number of the Fourier transformation of the compact finite difference scheme. The numerical wave-number is purely real, which is a property of the non-dissipative central schemes. It can also be observed that the numerical wave-number provides a good approximation of the actual wave-number only over a limited portion of the wave-number spectrum. This can be shown in Fig. 3.1 as an example of the dispersive characteristics of a 6th-order compact scheme.

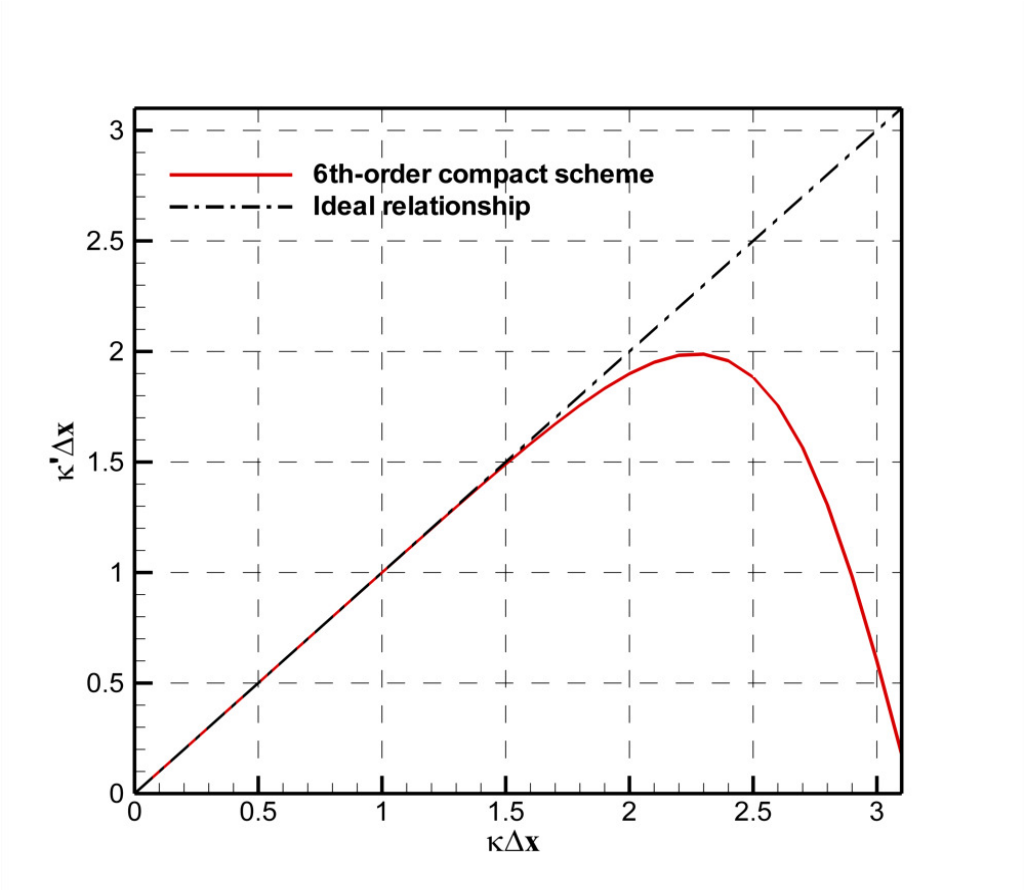

Figure 3.1: Dispersive characteristics of a 6th-order compact scheme.

The discretization schemes can be optimized by sacrificing formal order of accuracy to provide significantly better wave propagation characteristics in the high wave-number range. Ashcroft adopted the optimization strategy proposed by Kim and Lee [107] based on the Lagrange multipliers to minimize the difference between numerical wave-number and actual wave-number, subject to a certain accuracy constraint. The integrated error is defined as:

$$Err \equiv \int_0^{r\pi} (\kappa\Delta x - \kappa'\Delta x)^2 \, [1 + 2\alpha\cos(\kappa\Delta x) + 2\beta\cos(2\kappa\Delta x)]^2 \, d(\kappa\Delta x) \,, \qquad (3.16)$$

where the parameters α and β correspond to those defined in Eq. (3.10), and r is a factor to determine the optimization range ($0 < r < 1$). The conditions for Err to be minimal are

$$\frac{\partial Err}{\partial \eta_i} = 0 \,, \text{ for } i = 1, 2, ..., 5, \qquad (3.17)$$

where $\eta_1 = a$, $\eta_2 = b$, $\eta_3 = c$, $\eta_4 = \alpha$ and $\eta_5 = \beta$, again correspond to the coefficients of the basic stencil as defined by Eq. (3.10). When combined with Eq. (3.11) to maintain at least 4th-order accuracy, we obtain a system of linear algebraic equations by which the optimal coefficients may be obtained. Given an optimized scheme, the maximum resolvable wave-number can be defined as $\kappa_c'\Delta x$, using some criterion such as $|(d(\kappa_c'\Delta x)/d(\kappa\Delta x) - 1.0)| < 0.005$. The resolution of the spatial discretization schemes is also represented by the points-per-wavelength (PPW), which is computed as $2\pi / \kappa_c'\Delta x$.

The compact schemes may adopt a prefactorization method proposed by Hixon [34] to reduce a non-dissipative central-difference stencil to two low-order biased stencils which have simpler matrices. The advantages of these prefactored schemes over traditional compact schemes arise from their reduced stencil size and the independent nature of the factored matrices. It is well known that a major difficulty in dealing with high-order finite-difference schemes is the formulation of stable stencils near boundaries. By reducing the stencil size of the compact schemes the prefactorization method reduces the required number of boundary stencils thereby simplifying boundary specifications. The prefactored schemes also make boundary condition implementation much more straightforward than the standard schemes [33].

Define the forward and backward operators D_i^F and D_i^B, then the derivative can be evaluated as

$$D_i = \frac{1}{2}\left(D_i^F + D_i^B\right). \qquad (3.18)$$

The generic stencils for the forward and backward derivative operators are then defined by

$$\alpha_F D_{i+1}^F + \beta_F D_i^F = \frac{1}{\Delta x}\left[a_F f_{i+2} + b_F f_{i+1} + c_F f_i + d_F f_{i-1} + e_F f_{i-2}\right],$$
$$\beta_B D_i^B + \gamma_B D_{i-1}^B = \frac{1}{\Delta x}\left[a_B f_{i+2} + b_B f_{i+1} + c_B f_i + d_B f_{i-1} + e_B f_{i-2}\right], \quad (3.19)$$

where the coefficients must be chosen such that when the two biased stencils are added, the original central compact schemes is recovered.

The numerical wave-numbers of the generic forward and backward operators may be determined in the same way presented in Eq. (3.14). The real and imaginary components of the numerical wave-numbers are given by

$$\begin{aligned}
\mathrm{Re}(\tilde{\kappa}_F \Delta x) &= \frac{(a_F\alpha_F + b_F\beta_F - c_F\alpha_F - d_F\beta_F)\sin(\kappa\Delta x)}{\alpha_F^2 + \beta_F^2 + 2\alpha_F\beta_F\cos(\kappa\Delta x)} \\
&\quad + \frac{(a_F\beta_F - d_F\alpha_F - e_F\beta_F)\sin(2\kappa\Delta x) - e_F\alpha_F\sin(3\kappa\Delta x)}{\alpha_F^2 + \beta_F^2 + 2\alpha_F\beta_F\cos(\kappa\Delta x)}, \\
\mathrm{Im}(\tilde{\kappa}_F \Delta x) &= \frac{-(b_F\alpha_F + c_F\beta_F) - (a_F\alpha_F + b_F\beta_F + c_F\alpha_F + d_F\beta_F)\cos(\kappa\Delta x)}{\alpha_F^2 + \beta_F^2 + 2\alpha_F\beta_F\cos(\kappa\Delta x)} \\
&\quad - \frac{(a_F\beta_F + d_F\alpha_F + e_F\beta_F)\cos(2\kappa\Delta x) + e_F\alpha_F\cos(3\kappa\Delta x)}{\alpha_F^2 + \beta_F^2 + 2\alpha_F\beta_F\cos(\kappa\Delta x)}, \\
\mathrm{Re}(\tilde{\kappa}_B \Delta x) &= \frac{(b_B\beta_B + c_B\gamma_B - d_B\beta_B - e_B\gamma_B)\sin(\kappa\Delta x)}{\beta_B^2 + \gamma_B^2 + 2\gamma_B\beta_B\cos(\kappa\Delta x)} \\
&\quad + \frac{(a_B\beta_B + b_B\gamma_B - e_B\beta_B)\sin(2\kappa\Delta x) + a_B\gamma_B\sin(3\kappa\Delta x)}{\beta_B^2 + \gamma_B^2 + 2\gamma_B\beta_B\cos(\kappa\Delta x)}, \\
\mathrm{Im}(\tilde{\kappa}_B \Delta x) &= \frac{-(c_B\beta_B + d_B\gamma_B) - (b_B\beta_B + c_B\gamma_B + d_B\beta_B + e_B\gamma_B)\cos(\kappa\Delta x)}{\beta_B^2 + \gamma_B^2 + 2\gamma_B\beta_B\cos(\kappa\Delta x)} \\
&\quad - \frac{(a_B\beta_B + b_B\gamma_B + e_B\beta_B)\cos(2\kappa\Delta x) + a_B\gamma_B\cos(3\kappa\Delta x)}{\beta_B^2 + \gamma_B^2 + 2\gamma_B\beta_B\cos(\kappa\Delta x)}.
\end{aligned} \quad (3.20)$$

To recover the original central compact scheme when the biased operators are added, the coefficients of the forward and backward are chosen such that the imaginary components of the numerical wave-numbers of the forward and backward stencils are equal and opposite, and the real components are equal and identical to the numerical

wave-number of the original scheme [108]. Therefore, the coefficients should follow the restrictions as

$$\beta_B = \beta_F,\ \gamma_B = \alpha_F,\ a_B = -e_F,\ b_B = -d_F,\ c_B = -c_F,\ d_B = -b_F,\ e_B = -a_F. \quad (3.21)$$

In this thesis the optimized compact scheme (4th-order) of Ashcroft is employed to evaluate the spatial derivatives. The coefficients are given in Table 3.1. It can be observed that in relation to the original centered scheme the stencil has been reduced from five points to three points, and the original tri-diagonal matrix has been replaced by two independent bi-diagonal matrices.

Table 3.1: The coefficients of the 4th-order compact scheme.

	4th-order scheme
α_F	0.29749586350149729
β_F	0.71518963303413346
a_F	0.0
b_F	0.87203153537225117
c_F	-0.73137757420887159
d_F	-0.14065396116337958
e_F	0.0

For a domain consisting of N points, the three-point, fourth-order scheme can be applied from $j = 2$ to $N - 1$. At and near the domain boundaries it is necessary to employ additional expressions. The biased explicit stencils have therefore been developed at the boundary. The biased derivative operators for use with the three-point, fourth-order scheme are

$$D_1^B = \frac{1}{\Delta x}\sum_{j=1}^{4} s_j f_j,\ D_N^B = \frac{1}{\Delta x}\sum_{j=N-3}^{N} e_j f_j, \quad (3.22)$$

and

$$D_1^F = \frac{1}{\Delta x}\sum_{j=1}^{4} -e_{N+1-j} f_j,\ D_N^F = \frac{1}{\Delta x}\sum_{j=N-3}^{N} -s_{N+1-j} f_j, \quad (3.23)$$

where the coefficients s_j and e_j have been determined by matching the Taylor series of the forward and backward compact interior stencils to third-order accuracy. The numerical values of the coefficients are listed in Table 3.2.

Table 3.2: The coefficients of 4th-order compact scheme at the boundary.

	4th-order scheme
s_1	-1.968010730879214299
s_2	3.336693493864702415
s_3	-1.769354795091761932
s_4	0.400672032106273816
e_N	1.69865593578745236
e_{N-1}	-2.66330650613529758
e_{N-2}	1.23064520490823806
e_{N-3}	-0.26599463456039285

In computations, interior boundaries exist where the flow data are known on both sides of the boundary such as block interface boundary. Along internal boundaries the following eleven point central schemes are employed

$$D_i^F = \frac{1}{\Delta x}\sum_{j=-5}^{5} b_j f_{i+j}\ ,\ D_i^B = \frac{1}{\Delta x}\sum_{j=-5}^{5} -b_{-j} f_{i+j}\ , \tag{3.24}$$

where the coefficients b_j ($b_{-j} = -b_j$) are as listed in Table 3.3. These coefficients have been determined by matching the Taylor series expansions of the forward and backward interior stencils to fourth-order and using the remaining free coefficients to more closely match the dispersion characteristics.

Table 3.3: The coefficients of 4th-order compact scheme at the interior boundary.

	4th-order scheme
b_0	-0.21013712054967647
b_1	0.96979343766394390
b_2	-0.27390976718640895
b_3	0.07031776392683924
b_4	-0.01184575620106222
b_5	0.00083442741566041

The numerical stability and eigenvalue analysis of this optimized compact scheme can be fully reviewed in [35].

3.4. Time Marching Methods

In SotonCAA, a low dispersion and dissipation Runge Kutta (LDDRK) is implemented, which is 4th-order accurate for linear problems and 2nd-order accurate for non-linear problems, consisting of two storage level marching cycle (4-6 LDDRK) [37]. This is an optimized two-step alternating scheme, in which different coefficients are employed at the alternating steps. The scheme uses four stages in the first time step and six stages in the second step of the cycle. If the semi-discretized governing equations are written as

$$\frac{d\hat{Q}}{dt} = -(D_\xi \hat{F} + D_\eta \hat{G} + D_\zeta \hat{H}) + \frac{M_\infty}{\mathrm{Re}}(D_\xi \hat{F}_V + D_\eta \hat{G}_V + D_\zeta \hat{H}_V) = R(\hat{Q}), \tag{3.25}$$

where D_ξ, D_η and D_ζ denotes the spatial derivative operators, each step in the cycle may be written as

$$\hat{Q}^{n+1} = \hat{Q}^n + \sum_{i=1}^{N} s_i K_i, \tag{3.26}$$

where $K_i = \Delta t R(\hat{Q}^n + \sum_{j=1}^{i-1} \varphi_{ij} K_j)$, $i = 1, 2, \ldots, N$.

Here N denotes the number of stages in each step, s_i and φ_{ij} are the coefficients of the particular step. The superscript n indicates time level. Integration from time level n to level $n + 2$ is accomplished by first using the four stages schemes to integrate from time level n to $n + 1$, and then six stages schemes to integrate from time level $n + 1$ to $n + 2$. Two-step schemes permit a greater degree of optimization for wave propagation. In this way the dissipation and dispersion errors are further reduced than those through optimization of either of the individual single steps.

To improve the computation efficiency, the two-step alternating scheme is implemented in a low storage format. Each of the steps in the alternating scheme is evaluated by computing

$$K_i = \Delta t R(\hat{Q}^n + \overline{\varphi}_i K_{i-1}), \tag{3.27}$$

for $i = 1, 2, \ldots, N$ (with $\overline{\varphi}_1 = 0$), and then evaluating

$$\hat{Q}^{n+1} = \hat{Q}^n + K_p. \tag{3.28}$$

This implementation requires three levels of data storage, instead of four levels in the classical fourth-order Runge-Kutta scheme.

In order to overcome the CFL limit of explicit schemes, an implicit lower-upper approximate factorization algorithm is developed. A pseudo-time technique is introduced into this scheme as well as a Newton-like subiteration, which is performed to obtain the convergence of the calculations at each physical time step before progressing to the next time step [109]. The original governing equations can be written as

$$\frac{\partial \hat{Q}}{\partial \tau} + \frac{\partial \hat{Q}}{\partial t} + \frac{\partial \hat{E}}{\partial \xi} + \frac{\partial \hat{F}}{\partial \eta} + \frac{\partial \hat{G}}{\partial \zeta} = \frac{M_\infty}{\mathrm{Re}}\left(\frac{\partial \hat{E}_V}{\partial \xi} + \frac{\partial \hat{F}_V}{\partial \eta} + \frac{\partial \hat{G}_V}{\partial \zeta}\right). \tag{3.29}$$

It then can be represented in the form of notations as follows [40, 102]

$$\begin{aligned}(L+D)D^{-1}(D+U)\Delta\hat{Q}^m = &-\frac{3\hat{Q}^m - 4\hat{Q}^n + \hat{Q}^{n-1}}{2} \\ &- \Delta t D_\xi\left(\hat{E}^m - \frac{M_\infty}{\mathrm{Re}}\hat{E}_V^m\right) \\ &- \Delta t D_\eta\left(\hat{F}^m - \frac{M_\infty}{\mathrm{Re}}\hat{F}_V^m\right) \\ &- \Delta t D_\zeta\left(\hat{G}^m - \frac{M_\infty}{\mathrm{Re}}\hat{G}_V^m\right)\end{aligned}, \tag{3.30}$$

where D_ξ, D_η and D_ζ represents the space differences in the generalized coordinates. To achieve 2nd-order accuracy, subiterations are used to reduce the error due to factorization, linearization and explicit implement of boundary conditions. $\hat{Q}^m$ is the m subiteration to approximate $\hat{Q}^{n+1}$ and $\Delta\hat{Q}^m = \hat{Q}^{m+1} - \hat{Q}^m$. At time level n, the solution is

advanced from $m = 1$ and $\hat{Q}^m = \hat{Q}^n$. Three to five subiterations per time step are suitable for flow calculation [23, 110].

In Eq. (3.30),

$$L = -\Delta t(\hat{A}^+_{i-1,j,k} + \hat{B}^+_{i,j-1,k} + \hat{C}^+_{i,j,k-1}),$$

$$D = [\frac{3}{2} + \Delta t(r_{\hat{A}} + r_{\hat{B}} + r_{\hat{C}})]I,$$

$$U = \Delta t(\hat{A}^-_{i+1,j,k} + \hat{B}^-_{i,j+1,k} + \hat{C}^-_{i,j,k+1}), \tag{3.31}$$

where

$$\hat{A}^+ = \frac{\hat{A} + r_{\hat{A}} I}{2}, \hat{B}^+ = \frac{\hat{B} + r_{\hat{B}} I}{2}, \hat{C}^+ = \frac{\hat{C} + r_{\hat{C}} I}{2},$$

$$\hat{A}^- = \frac{\hat{A} - r_{\hat{A}} I}{2}, \hat{B}^- = \frac{\hat{B} - r_{\hat{B}} I}{2}, \hat{C}^- = \frac{\hat{C} - r_{\hat{C}} I}{2}, \tag{3.32}$$

and $r_{\hat{A}} = \max(|\lambda_{\hat{A}}|)$, $r_{\hat{B}} = \max(|\lambda_{\hat{B}}|)$, $r_{\hat{C}} = \max(|\lambda_{\hat{C}}|)$ where $\lambda_{\hat{A}}$, $\lambda_{\hat{B}}$, and $\lambda_{\hat{C}}$ are the eigenvalues of flux Jacobian matrices. The flux Jacobians are calculated from their Cartesian counterparts by

$$\hat{A} = \xi_x A + \xi_y B + \xi_z C,$$

$$\hat{B} = \eta_x A + \eta_y B + \eta_z C,$$

$$\hat{C} = \zeta_x A + \zeta_y B + \zeta_z C, \tag{3.33}$$

where

$$A = \begin{bmatrix} 0 & 1 & 0 & 0 & 0 \\ -u^2 + \frac{\gamma-1}{2}U^2 & (3-\gamma)u & (1-\gamma)v & (1-\gamma)w & \gamma-1 \\ -vu & v & u & 0 & 0 \\ -wu & w & 0 & u & 0 \\ -\gamma eu + u(\gamma-1)U^2 & \gamma e - \frac{\gamma-1}{2}(2u^2+U^2) & (1-\gamma)uv & (1-\gamma)uw & \gamma u \end{bmatrix},$$

$$B=\begin{bmatrix} 0 & 0 & 1 & 0 & 0 \\ -uv & v & u & 0 & 0 \\ -v^2+\dfrac{\gamma-1}{2}U^2 & (1-\gamma)u & (3-\gamma)v & (1-\gamma)w & \gamma-1 \\ -wv & 0 & w & v & 0 \\ -\gamma ev+v(\gamma-1)U^2 & (1-\gamma)uv & \gamma e-\dfrac{\gamma-1}{2}(2v^2+U^2) & (1-\gamma)vw & \gamma v \end{bmatrix},$$

$$C=\begin{bmatrix} 0 & 0 & 0 & 1 & 0 \\ -uw & w & 0 & u & 0 \\ -vw & 0 & w & v & 0 \\ -w^2+\dfrac{\gamma-1}{2}U^2 & (1-\gamma)u & (1-\gamma)v & (3-\gamma)w & \gamma-1 \\ -\gamma ew+w(\gamma-1)U^2 & (1-\gamma)uw & (1-\gamma)vw & \gamma e-\dfrac{\gamma-1}{2}(2w^2+U^2) & \gamma w \end{bmatrix},$$

and $$U^2=u^2+v^2+w^2. \tag{3.34}$$

3.5. Filtering Technique

When nonlinear problems are computed, the wave-number content of the solution changes as the flow evolves. A classic example of this is a wave steepening into a shock. As this flow phenomenon occurs, it drives the wave-number content of the solution out of the resolvable range of the numerical scheme. These irresolvable waves will travel at the wrong speed, and even in the wrong direction. To combat this, artificial selective damping model is used to selectively damp or remove the high wave-number components of the numerical solution [111]. The artificial selective damping model introduced by Tam et al. [112] basically inserts an artificial damping term D_i to the right-hand side of the finite difference equations. It is constructed in the seven-point stencil, and can be written as

$$D_i=-\frac{v_a}{(\Delta x)^2}\sum_{m=-3}^{3}a_m Q_{i+m}, \tag{3.35}$$

where v_a is the variable artificial viscosity to adjust the magnitude of damping and a_m are the damping coefficients which are determined by the Fourier analysis in the wave-number domain. By choosing the coefficients properly, it is possible to control the damping only in the high wave-number range. In this work, a revised formulation of the artificial selective damping term in a conservative form proposed by Kim et al. [113] is

implemented. The selective damping term is changed into a form of difference between two split damping flux terms as

$$D_i = (d_{i+1/2} - d_{i-1/2}) / \Delta x , \tag{3.36}$$

where the damping flux vector $d_{i+1/2}$ is given as

$$d_{i+1/2} = C_{i+1/2} \sum_{m=-2}^{3} b_m Q_{i+m} , \tag{3.37}$$

and $C_{i+1/2}$ is a controlling function of dissipation magnitude at the interface of adjacent two cells. The damping coefficients b_m are determined by matching the coefficients a_m in Eq. (2.35). In the final formulation, the second-order derivative term in the nonlinear artificial dissipation model [114] is combined to the damping flux to improve the resolution of discontinuity and enhance the numerical stability near the shock wave [113].

In practical CFD/CAA simulations, unexpected numerical errors are inevitable and might originate from many ways: mesh non-uniformity, abrupt slope changes between multiple blocks, nonlinear flow features, boundary conditions or even poorly specified initial conditions. Although these errors are normally very small, they could deteriorate progressively and cause severe problems. To overcome these difficulties, filtering technique is incorporated to smooth all the abnormal deleterious perturbations. If a component of the solution vector is denoted by f_i , filtered value $\hat{f}_i$ is obtained by general central explicit filtering scheme

$$\hat{f}_i = \sum_{j=-m}^{j=m} \alpha_j f_{i+j} , \tag{3.38}$$

where $2m + 1$ points stencil is selected of highest order $2m$ in accuracy. With a proper choice of the coefficients, the order and spectral resolution of the filter can be determined. Table 3.4 gives a group of coefficients of 6th-order central difference filtering scheme with seven-point stencil, which is used in the turbulence equation.

Table 3.4: The coefficients of the 6th-order central difference filtering scheme.

α_{-3}	0.015625
α_{-2}	-0.09375
α_{-1}	0.234375
α_0	0.6875
α_1	0.234375
α_2	-0.09375
α_3	0.015625

The 6th-order central difference formula is not possible for use at and close to boundary points, where biased filtering schemes are used with the order of accuracy gradually reduced. In current research, the filtering accuracy is reduced to 3rd-order at the boundary points, see table 3.5.

Table 3.5: Biased filter schemes at the boundary.

Biased filter	**Accuracy**
$\hat{f}_1 = f_1 - (f_1 - f_4 - 3(f_2 - f_3))/8$	3rd-order
$\hat{f}_2 = f_2 - (-3f_1 + 10f_2 - 12f_3 + 6f_4 - f_5)/32$	4th-order
$\hat{f}_3 = f_3 - (3f_1 - 12f_2 + 19f_3 - 15f_4 + 6f_5 - f_6)/56$	5th-order
$\hat{f}_{i-2} = f_{i-2} - (3f_i - 12f_{i-1} + 19f_{i-2} - 15f_{i-3} + 6f_{i-4} - f_{i-5})/56$	5th-order
$\hat{f}_{i-1} = f_{i-1} - (-3f_i + 10f_{i-1} - 12f_{i-2} + 6f_{i-3} - f_{i-4})/32$	4th-order
$\hat{f}_i = f_i - (f_i - f_{i-3} - 3(f_{i-1} - f_{i-2}))/8$	3rd-order

All the central and biased filters are performed in all generalized directions to conserved variables every time step.

3.6. Turbulence Models

In current research, the S-A [9] one equation model is implemented by solving a single partial differential transport equation for a working variable related to the turbulence viscosity.

$$\frac{\partial \rho \tilde{\nu}}{\partial t} + \frac{\partial \rho u_i \tilde{\nu}}{\partial x_i} = P + \left(\frac{\partial}{\partial x_j}\left(\frac{\mu + \rho\tilde{\nu}}{\sigma}\frac{\partial \tilde{\nu}}{\partial x_j}\right) + \frac{\rho c_{b2}}{\sigma}\left(\frac{\partial \tilde{\nu}}{\partial x_j}\right)^2\right) - D\,. \qquad (3.39)$$

The terms on the RHS of Eq. (3.39) represent production, gradient diffusion and the wall destruction of the turbulent kinematic viscosity respectively. The production is defined as

$$P = c_{b1}\rho\tilde{S}\tilde{\nu}\,, \tag{3.40}$$

where

$$\tilde{S} = \Omega + \frac{\tilde{\nu}}{\kappa^2 d^2} f_{\upsilon 2}\,, \qquad f_{\upsilon 2} = 1 - \frac{\chi}{1+\chi f_{\upsilon 1}}\,, \qquad \chi = \frac{\tilde{\nu}}{\mu/\rho}\,. \tag{3.41}$$

The destruction is defined as

$$D = c_{w1} f_w \rho (\frac{\tilde{\nu}}{d})^2\,, \tag{3.42}$$

where

$$f_w = g[\frac{1+c_{w3}^6}{g^6 + c_{w3}^6}]^{\frac{1}{6}}, \tag{3.43}$$

$$g = r + c_{w2}(r^6 - r)\,, \tag{3.44}$$

and

$$r = \frac{\tilde{\nu}}{\tilde{S}\kappa^2 d^2}\,. \tag{3.45}$$

For numerical stability reasons, some limits are added in the implementation

$$\tilde{\nu} = \max(\tilde{\nu}, 0)\,,\ r = \frac{\tilde{\nu}}{\max(\tilde{S}, \varepsilon)\kappa^2 d^2}\,,\ \varepsilon = 1\times 10^{-16}. \tag{3.46}$$

Finally the eddy viscosity is obtained by

$$\mu_t = \rho f_{\upsilon 1}\tilde{\nu}\,. \tag{3.47}$$

The empirical constants are given by

$$\kappa = 0.41\,,\ c_{b1} = 0.1355\,,\ c_{b2} = 0.622\,,\ c_{w1} = \frac{c_{b1}}{\kappa^2} + \frac{c_{b2}+1}{\sigma}\,,$$

$$c_{w2} = 0.3\,,\ c_{w3} = 2.0\,,\ c_{v1} = 7.1\,,\ \sigma = \frac{2}{3}\,. \tag{3.48}$$

Spalart et al. extended this one-equation model so that it yielded a conventional eddy viscosity near the wall-bounded regions but switched to a pseudo LES model that is proportional to the grid spacing Δ away from the wall. The destruction term now is written as

$$D = c_{w1} f_w \rho (\frac{\tilde{\nu}}{\tilde{d}})^2\,. \tag{3.49}$$

In the S-A model d is the distance to the nearest wall. In DES, d is replaced with $\tilde{d}$, which is defined by

$$\tilde{d} = \min(d, C_{DES}\Delta)\,, \text{ with } C_{DES} = 0.65 \text{ and } \Delta = \max(\Delta x, \Delta y, \Delta z)\,. \tag{3.50}$$

where Δx, Δy, Δz denote the grid spacing in different directions. Defining $\Delta = \max(\Delta x, \Delta y, \Delta z)$ ensures RANS behaviour in boundary layers as $d << \Delta$.

3.7. Grid Generation

The requirement for structured grid topology of high-order finite difference schemes makes the grid generation the most challenging task, especially for some complicated cases with considerably irregular geometries. Sharp angled cells and high stretching ratio grids must be avoided in order to maintain the continuity of the calculated values along the stencil line. The control of the amount of total grid points would be another inevitable issue for CFD/CAA. More detailed mesh structure captures more flow and acoustic details, and thus improves the calculation results. However, more grid points demand high level of computing ability, which could be extremely expensive or even impossible. As for the unsteady flow, mesh must be built sufficiently fine in the vicinity of solid boundary to capture as much unsteady characteristics as possible. The sub-layer

scaled distance y^+ can be considered as a useful guiding value for quality of grid generation. y^+, the non-dimensional wall distance for a wall bounded flow, is defined as

$$y^+ \equiv \frac{u_* y}{\upsilon}. \tag{3.51}$$

where u_* is the friction velocity at the nearest wall, y is the distance to the nearest wall and υ is the local kinematical viscosity of the fluid. Typically, in the DES simulation, a good mesh should have y^+ value in the order of unity.

3.8. Radiation Boundary Conditions

In current research, buffer zone boundary condition is used for outer boundary initialization and updating. The buffer zone is demonstrated in Fig. 3.2.

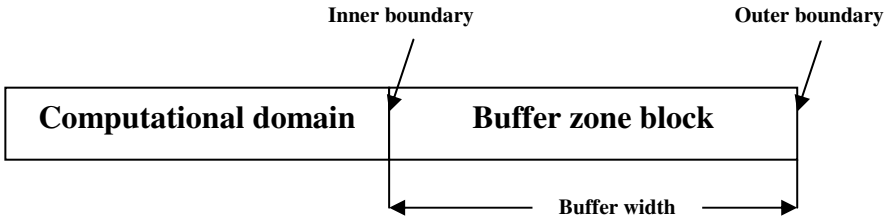

Figure 3.2: A demonstration of the buffer zone.

The computational grid is extended to create an extra domain, buffer zone, surrounding the main computational domain, and in the buffer zone the solution vector is explicitly damped after each time step using

$$\hat{Q}^{n+1} = Q^{n+1} - \sigma(Q^{n+1} - Q_{target}),$$
$$\sigma(x) = \sigma_{\max}\left|1 + \frac{x_b - L}{L}\right|^{\beta}, \tag{3.52}$$

where Q^{n+1} is the solution vector after each time step and Q_{target} is the expected value in the buffer zone. The damping coefficient σ varies smoothly according to the damping

function $\sigma(x)$, where L is the width of the buffer zone, x_b is the distance measured from the inner boundary of the buffer zone, and σ_{max}, β are coefficients which determine the shape of the damping function. In the present study, $\sigma_{max} = 1.0$ and $\beta = 2.5$ are used with a total number of 15 grid points employed in the buffer zone.

3.9. Interface Boundary Conditions

A structured grid usually has difficulties in solving finite difference equations at interface surfaces/lines, since the grid matrices are discontinuous along the interface where abrupt changes in the slope of a grid line may happen. Though the discontinuity can be avoided for very simple geometry by generating smooth mesh across multiple blocks, it is impossible for complex geometries such as landing gears. Conventionally, the grid matrices at the interface are often approximated to single values by averaging the left- and right-hand limits. This certainly introduces numerical errors, which cannot be well suppressed by high-order high-resolution finite difference schemes. A multiple block computing technique with characteristic interface conditions is developed to overcome these difficulties [104].The computational domain is decomposed into blocks along the interface lines, where the left and right blocks have the one-sided limits of the grid matrices treated separately, demonstrated in Fig. 3.3. High-order finite difference schemes are used in each block, which employ central differences on the interior nodes and one-sided differences on the near-boundary nodes. The differencing stencils do not cross the block interfaces. The isolated blocks then communicate with each other through characteristic waves transporting normal to the interface boundary.

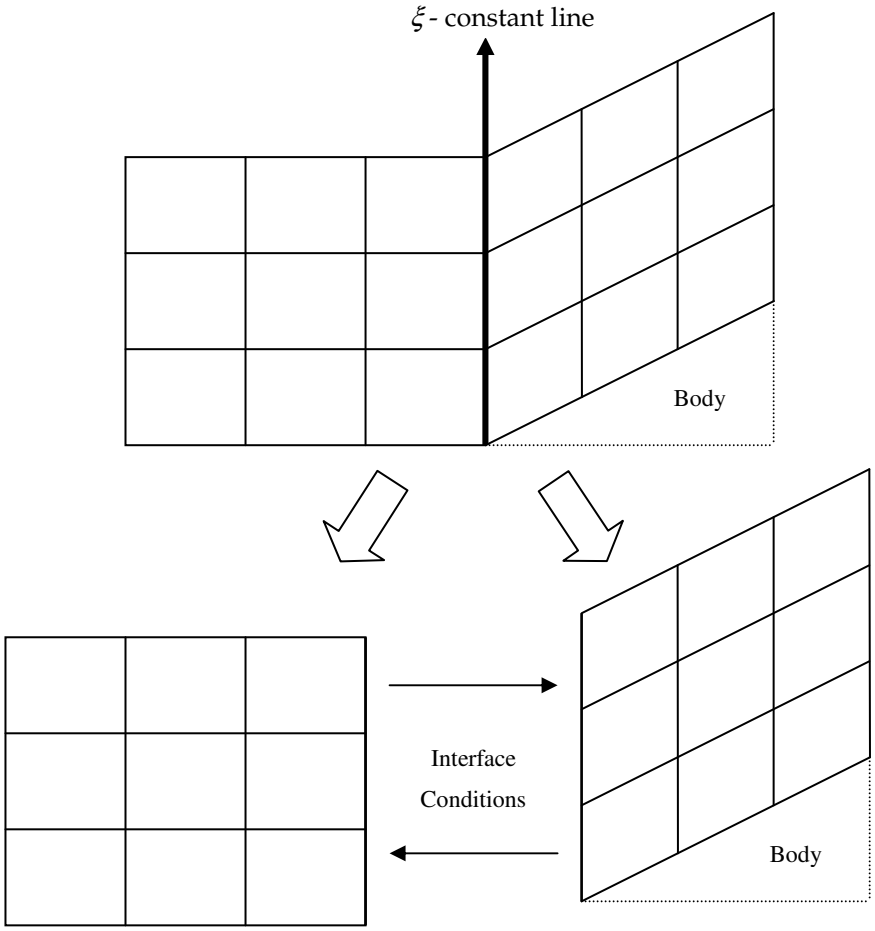

Figure 3.3: Decomposing a computational domain into isolated blocks.

The generalized governing equation Eq. (3.6) can be transformed into a characteristic form in the direction normal to the interface where for example ξ keeps a constant. The resulting equation can be derived using Eq. (3.7) as

$$\frac{\partial R}{\partial t} + \overline{\lambda}\frac{\partial R}{\partial \xi} = S_C\,, \tag{3.53}$$

where

$$\delta R = \overline{P}^{-1}\delta Q\,,\ \overline{\lambda}\frac{\partial R}{\partial \xi} = \overline{P}^{-1}(\xi_x\frac{\partial E}{\partial \xi} + \xi_y\frac{\partial F}{\partial \xi} + \xi_z\frac{\partial G}{\partial \xi})\,. \tag{3.54}$$

The source term S_C in Eq. (3.53) is given by

$$S_C = J\overline{P}^{-1}\left\{\hat{S}_V - [E\frac{\partial}{\partial\xi}(\frac{\xi_x}{J}) + F\frac{\partial}{\partial\xi}(\frac{\xi_y}{J}) + G\frac{\partial}{\partial\xi}(\frac{\xi_z}{J}) + \frac{\partial\hat{F}}{\partial\eta} + \frac{\partial\hat{G}}{\partial\zeta}]\right\}. \quad (3.55)$$

The corresponding convection speeds in Eq. (3.53) are expressed as

$$\overline{\lambda} = \begin{pmatrix} U & 0 & 0 & 0 & 0 \\ 0 & U & 0 & 0 & 0 \\ 0 & 0 & U & 0 & 0 \\ 0 & 0 & 0 & U + a_0\sqrt{\xi_x^2 + \xi_y^2 + \xi_z^2} & 0 \\ 0 & 0 & 0 & 0 & U - a_0\sqrt{\xi_x^2 + \xi_y^2 + \xi_z^2} \end{pmatrix}, \quad (3.56)$$

where

$$U = \xi_x u + \xi_y v + \xi_z w. \quad (3.57)$$

The matrix $\overline{P}^{-1}$ that transforms the conservative variables into the characteristic variables is given as

$$\overline{P}^{-1} = \begin{pmatrix} \vec{B}_0\cdot\vec{l}_x & (\gamma-1)\frac{u}{a_0^2}\tilde{\xi}_x & (\gamma-1)\frac{v}{a_0^2}\tilde{\xi}_x + \frac{\tilde{\xi}_z}{\rho} & (\gamma-1)\frac{w}{a_0^2}\tilde{\xi}_x - \frac{\tilde{\xi}_y}{\rho} & -\frac{\gamma-1}{a_0^2}\tilde{\xi}_x \\ \vec{B}_0\cdot\vec{l}_y & (\gamma-1)\frac{u}{a_0^2}\tilde{\xi}_y - \frac{\tilde{\xi}_z}{\rho} & (\gamma-1)\frac{v}{a_0^2}\tilde{\xi}_y & (\gamma-1)\frac{w}{a_0^2}\tilde{\xi}_y + \frac{\tilde{\xi}_x}{\rho} & -\frac{\gamma-1}{a_0^2}\tilde{\xi}_y \\ \vec{B}_0\cdot\vec{l}_z & (\gamma-1)\frac{u}{a_0^2}\tilde{\xi}_z + \frac{\tilde{\xi}_y}{\rho} & (\gamma-1)\frac{v}{a_0^2}\tilde{\xi}_z - \frac{\tilde{\xi}_x}{\rho} & (\gamma-1)\frac{w}{a_0^2}\tilde{\xi}_z & -\frac{\gamma-1}{a_0^2}\tilde{\xi}_z \\ \frac{a_0}{\rho}(\frac{\gamma-1}{2}M_\infty^2 - \frac{\vec{v}\cdot\vec{l}_\xi}{a_0}) & \vec{C}_+\cdot\vec{l}_x & \vec{C}_+\cdot\vec{l}_y & \vec{C}_+\cdot\vec{l}_z & \frac{\gamma-1}{\rho a_0} \\ \frac{a_0}{\rho}(\frac{\gamma-1}{2}M_\infty^2 + \frac{\vec{v}\cdot\vec{l}_\xi}{a_0}) & \vec{C}_-\cdot\vec{l}_x & \vec{C}_-\cdot\vec{l}_y & \vec{C}_-\cdot\vec{l}_z & \frac{\gamma-1}{\rho a_0} \end{pmatrix}$$

$$\vec{B}_0 = (1 - \frac{\gamma-1}{2}M_\infty^2)\vec{l}_\xi - \frac{1}{\rho}(\vec{v}\times\vec{l}_\xi),$$

$$C_\pm = \pm\frac{\vec{l}_\xi}{\rho} - \frac{\gamma-1}{\rho a_0}\vec{v},\ \vec{v} = (u,v,w)^T. \quad (3.58)$$

where $\vec{l}_x$, $\vec{l}_y$ and $\vec{l}_z$ are the unit vectors in the *x*, *y* and *z* directions, respectively, and $\vec{l}_\xi$ is the unit normal vector defined by

$$\vec{l}_{\xi} = \nabla\tilde{\xi} \equiv \nabla\xi / |\nabla\xi| . \tag{3.59}$$

Eq. (3.53) represents the physical waves with different convection speeds in the direction normal to the interface, in which wave direction can be determined by the sign of the convection speeds. Incoming waves calculated within an isolated block is inaccurate because of loss of the information outside the block. Therefore, incoming waves of one block should be corrected by the outgoing waves of the other adjacent block through the interface conditions. The strict interface condition is that the primitive variables on the left and the right side of the interface must be matched regardless of time. That is equivalent to

$$\frac{\partial R^L}{\partial t} = \frac{\partial R^R}{\partial t} . \tag{3.60}$$

Let

$$L = \overline{\lambda} \frac{\partial R}{\partial \xi}, \tag{3.61}$$

then the interface conditions can be expressed by the convection and source term as

$$L^L - S_C^L = L^R - S_C^R . \tag{3.62}$$

Finally, after the corrections with interface conditions, the primitive variables on the interface need to be refined by averaging the left- and right-hand values, which is dealing with the round off errors on separate blocks.

3.10. Parallel Implementation

SotonCAA has been written in FORTRAN using the Messenger Passing Interface (MPI) libraries for parallel execution on the distributed computing memories. Parallelization of the code is accomplished in a domain decomposition approach in

which the blocks of the computational domain are divided among the processors. A schematic representation of the parallel multi-block implementation is shown in Fig. 3.4. The figure depicts a domain composed of four blocks, split on to three processors. Memory is allocated for each block only on the processor to which it has been assigned. Along inter-block boundaries halo regions of ghost cells are defined to facilitate the data transfer between blocks. If the adjacent blocks are located on the same processor (e.g. block 2 and 3), the exchange of data along the boundary is accomplished by simply accessing the appropriate local memory. However, if the adjacent blocks are allocated on separate processors, then the exchange of data is accomplished using MPI.

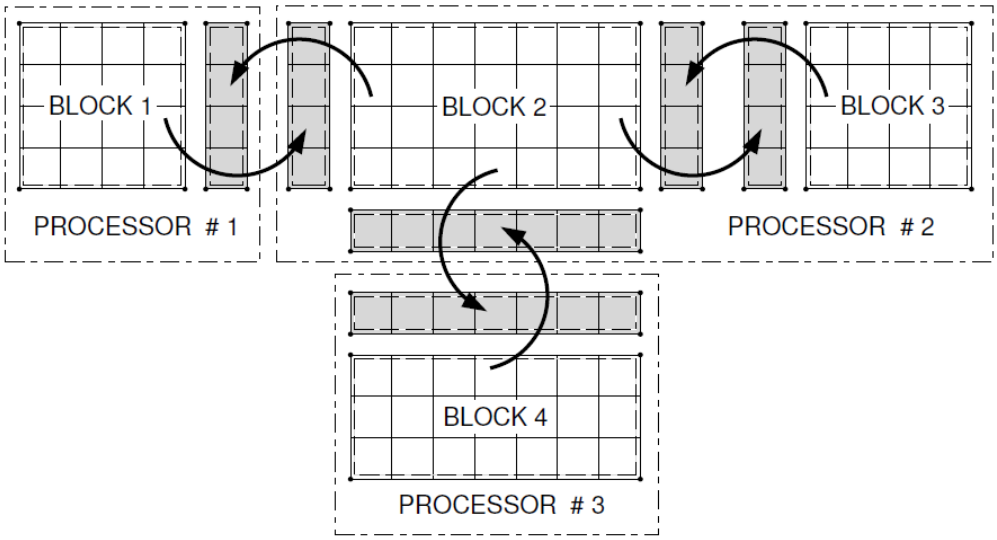

Figure 3.4: Schematic representation of inter-block communication.

3.11. Radiation Model

To resolve the acoustic field in the far field an integral technique, based on the Ffowcs Williams and Hawkings equation (FW-H) [17], has been implemented. The FW-H equation is an exact rearrangement of the Navier-Stokes equations and is appropriate for computing the acoustic field when solid boundaries play a direct role in the generation of sound. The solution of the FW-H equation is obtained in terms of volume and surface integrals and may be used to predict the far-filed acoustic signal based solely on near field data. The FW-H method has typically been applied by having the integration surface coincide with solid boundaries, but the method is still applicable when the

surface is off the body and permeable. Thus, unlike the Kirchhoff method [115], the FW-H equation is valid even if the integration surface lies in the non-linear region. This flexibility, coupled with the fact that the solution is often well approximated by the surface integrals alone, makes the FW-H method an attractive technique for predicting the far field acoustic signal. In the following, a derivation of the FW-H equation, as employed in the acoustic propagation code, is given.

The FW-H equation may be derived by considering a generic body with surface S, described by the equation $f_s = 0$, immersed in a fluid as shown in Fig. 3.5. If the body submerged in the fluid is replaced by fluid at rest ($p = p_o$, $\rho = \rho_o$ and $u_i = 0$), and the flow variables are regarded as generalized functions, the validity of the equations of fluid motion may be extended to all space through the use of the Heaviside function. The resulting equations may then be combined in the manner originally proposed by Lighthill to form an inhomogeneous wave equation valid throughout all space. This equation is known as the FW-H equation and in differential form may be written as

$$\left(\frac{1}{c_o^2}\frac{\partial^2}{\partial t^2}-\frac{\partial^2}{\partial x_i^2}\right)\left(c_o^2(\rho-\rho_o)H(f_s)\right)=\frac{\partial^2}{\partial x_i\partial x_j}\left(T_{ij}H(f_s)\right) -\frac{\partial}{\partial x_i}\left(L_i\delta(f_s)\right)+\frac{\partial}{\partial t}\left(U_n\delta(f_s)\right), \tag{3.63}$$

where

$$\begin{aligned} T_{ij} &= \rho u_i u_j - \tau_{ij} + \left((p-p_o)-c_o^2(\rho-\rho_o)\right)\delta_{ij}, \\ L_i &= L_{ij}\hat{n}_j = \left(\rho u_i\left(u_j - v_j\right) + p'_{ij}\right)\hat{n}_j, \\ U_n &= U_i\hat{n}_i = \left(\rho\left(u_i - v_i\right) + \rho_o v_i\right)\hat{n}_i. \end{aligned} \tag{3.64}$$

The first term T_{ij} is known as the Lighthill stress tensor, and represents the volume quadrupole sources. The components of T_{ij} are the Reynolds stresses, the viscous stresses and terms relating to entropy and fluid inhomogeneity. The second term L_i is a surface dipole. The first term relates to the flux of momentum across the surface S, while the second term $p'_{ij} = (p-p_o)\delta_{ij} - \tau_{ij}$ is the force per unit area applied over S. The remaining source term U_n is a surface monopole. It is composed of two components.

The first represents the mass flux through the surface, while the second is the equivalent mass flux due to the surface motion.

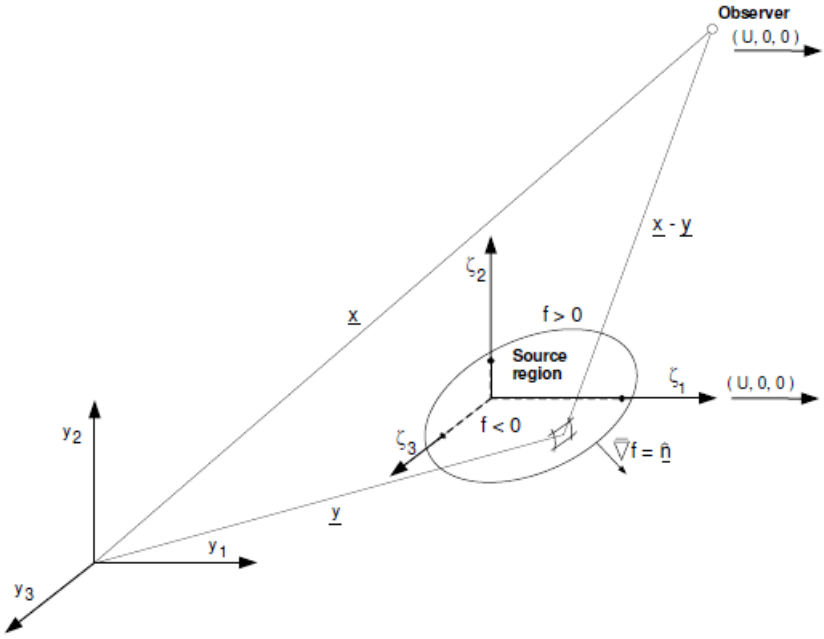

Figure 3.5: Coordinate system fixed in a surface.

Away from the source region Eq. (3.63) reduces to the homogeneous wave equation and the term $c_o^2(p-p_o)$ tends to the acoustic pressure. An integral formula expressing the solution to Eq. (3.63) may be obtained in terms of a Green's function $G(\mathrm{x},t\,|\,\mathrm{y},\tau)$ satisfying the equation

$$\left(\frac{1}{c_o^2}\frac{\partial^2}{\partial t^2}-\frac{\partial^2}{\partial x_i^2}\right)G(\mathrm{x},t\,|\,\mathrm{y},\tau)=\delta(\mathrm{x}-\mathrm{y})\delta(t-\tau), \tag{3.65}$$

for an impulsive point source. The Green's function $G(\mathrm{x},t\,|\,\mathrm{y},\tau)$ may be thought of as representing the response at x and time t due to an impulsive force at the point y and the time τ. The solution is formed by multiplying Equation (3.65) by the right-hand-side of Equation (3.63) at position y and time τ and integrating over all space and time, including the volume interior to S. Exploiting the sifting property of the Dirac delta

functions in Equation (3.65), an integral equation for the acoustic pressure p' at time t and position x may be written as

$$\begin{aligned} p'(\mathrm{x},t) = &\int_{-\infty}^{\infty} \iiint_V \left[G \frac{\partial^2}{\partial y_i \partial y_j} \left(T_{ij} H(f_s) \right) \right] dV(\mathrm{y}) d\tau \\ &- \int_{-\infty}^{\infty} \iint_V \left[G \frac{\partial}{\partial y_i} \left(L_i \delta(f_s) \right) - G \frac{\partial}{\partial \tau} \left(U_n \delta(f_s) \right) \right] dV(\mathrm{y}) d\tau \end{aligned} . \tag{3.66}$$

Assuming the volume sources are limited to a finite region of space, the spatial and temporal derivative may be moved from the source terms to the Green's function using partial integration to obtain

$$p'(\mathrm{x},t) = \int_{-\infty}^{\infty} \iiint_{V(\tau)} T_{ij} \frac{\partial^2 G}{\partial y_i \partial y_j} dV(\mathrm{y}) d\tau + \int_{-\infty}^{\infty} \iint_{S(\tau)} L_i \frac{\partial G}{\partial y_i} dS(\mathrm{y}) d\tau - \int_{-\infty}^{\infty} \iint_{S(\tau)} U_n \frac{\partial G}{\partial \tau} dS(\mathrm{y}) d\tau , \tag{3.67}$$

where the properties of the Heaviside function have been used to limit the first volume integral to the region external to S, and the sifting property of the Dirac delta function has been used to reduce the remaining volume integrals to surface integrals.

Equation (3.67) is the fundamental equation governing the generation of sound in the presence of solid boundaries. It is exact and applies to any region which is bounded by permeable surfaces in arbitrary motion. When the right-hand-side of the equation is known the pressure fluctuations in the sound field can be calculated. Substitution of a Green's function appropriate to the particular problem considered completes the solution. In this work the free space Green's function is used. The three-dimensional free space Green's function is

$$G_0(\mathrm{x},t \mid \mathrm{y},\tau) = \frac{\delta(g)}{4\pi r}, \tag{3.68}$$

where $g = \tau - t + r/c_0$ and $r = |\mathrm{x} - \mathrm{y}|$ is the distance between observer and source.

To obtain the specific formulation of the FW-H equation implemented numerically, we first recall the elementary symmetry properties of the free space Green's function

$$\frac{\partial G_0}{\partial t} = -\frac{\partial G_0}{\partial \tau} \text{ and } \frac{\partial G_0}{\partial x_i} = -\frac{\partial G_0}{\partial y_i}. \tag{3.69}$$

Using these properties the spatial and temporal derivatives of G_0 with respect to source coordinate y and time τ are replaced by derivatives with respect to observer coordinate x and time t. Then, as the integration is performed on the source coordinate y and time τ, the spatial and temporal derivatives may be moved out of the integrals to obtain

$$\begin{aligned} p'(\mathrm{x},t) = {} & \frac{\partial^2}{\partial x_i \partial x_j} \int_{-\infty}^{\infty} \iiint_{V(\tau)} T_{ij} \frac{\delta(g)}{4\pi r} dV(\mathrm{y}) d\tau - \frac{1}{c_0} \frac{\partial}{\partial t} \int_{-\infty}^{\infty} \iint_{S(\tau)} L_i \hat{r}_i \frac{\delta(g)}{4\pi r} dS(\mathrm{y}) d\tau \\ & + \int_{-\infty}^{\infty} \iint_{S(\tau)} L_i \hat{r}_i \frac{\delta(g)}{4\pi r^2} dS(\mathrm{y}) d\tau + \frac{\partial}{\partial t} \int_{-\infty}^{\infty} \iint_{S(\tau)} U_n \frac{\delta(g)}{4\pi r} dS(\mathrm{y}) d\tau \end{aligned}, \tag{3.70}$$

where $\hat{r}_i$ is the component of the unit vector $\hat{\mathrm{r}}$ in the x_i direction, $\hat{\mathrm{r}} = (\mathrm{x}-\mathrm{y})/|(\mathrm{x}-\mathrm{y})|$. The identity [116] below

$$\frac{\partial}{\partial x_i}\left(\frac{\delta(g)}{4\pi r}\right) = \frac{1}{c_0}\frac{\partial}{\partial t}\left(\frac{\hat{r}_i \delta(g)}{4\pi r}\right) - \frac{\hat{r}_i \delta(g)}{4\pi r^2}, \tag{3.71}$$

has been used to eliminate the spatial derivatives in the second source term. To evaluate the integrals over the delta functions it is convenient to introduce a coordinate system in which the surface $S(\tau)$ is stationary. In general, the surface may move arbitrarily and it would be appropriate to introduce a Lagrangian coordinate $\zeta_L(\mathrm{y},\tau)$. However, for the work undertaken here, it is sufficient to consider the surface to be rigid, and restrict our attention to a Cartesian coordinate system that simply translates with velocity U_s as indicated in Fig. 3.5. The Jacobian of the transform between the two Cartesian coordinates is taken to be unity, as is the ratio of the area elements $dS(\zeta_L)/dS(\mathrm{y})$. In the translating coordinate system the volume and surface integrals are independent of τ.

Therefore, the order of integration may be interchanged and the integration with respect to τ can be carried out to obtain the FW-H equation in source fixed coordinates

$$\begin{aligned} 4\pi p'(\mathrm{x},t) = & \frac{\partial^2}{\partial x_i \partial x_j} \iiint_V \left[\frac{T_{ij}}{r\,|1-M_r|} \right]_{\tau^*} dV(\zeta_L) + \iint_S \left[\frac{L_r}{r^2\,|1-M_r|} \right]_{\tau^*} dS(\zeta_L) \\ & + \frac{1}{c_0} \frac{\partial}{\partial t} \iint_S \left[\frac{U_n c_0 - L_r}{r\,|1-M_r|} \right]_{\tau^*} dS(\zeta_L) \end{aligned} , \qquad (3.72)$$

where $M_r = M_i r_i$ is the projection of the local surface Mach number $M_i = v_i / c_0$ in the radiation direction, $L_r = L_i \hat{r}_i$ and the notation $[\ ]_{\tau^*}$ indicates the quantity enclosed within the brackets is to be evaluated at position ζ_L and the retarded time

$$\tau^* = t - |\,\mathrm{x} - \mathrm{y}(\zeta_L, \tau^*)\,|/c_0 . \qquad (3.73)$$

To complete the derivation we note that as $r = |\,\mathrm{x} - \mathrm{y}\,|$ is a function of τ, the relation for retarded time $g = \tau - t + r/c_0$ may be used to show

$$\left.\frac{\partial}{\partial t}\right|_{\mathrm{x}} = \left[\frac{1}{1-M_r} \left.\frac{\partial}{\partial \tau}\right|_{\mathrm{x}} \right], \qquad (3.74)$$

which enables the time derivative to be taken inside the final integral, and evaluated analytically to obtain

$$\begin{aligned} 4\pi p'(\mathrm{x},t) = & \frac{\partial^2}{\partial x_i \partial x_j} \iiint_V \left[\frac{T_{ij}}{r\,|1-M_r|} \right]_{\tau^*} dV(\zeta_L) + \iint_S \left[\frac{\dot{U}_n + U_{\dot{n}}}{r(1-M_r)^2} \right]_{\tau^*} dS(\zeta_L) \\ & + \frac{1}{c_0} \iint_S \left[\frac{\dot{L}_r}{r(1-M_r)^2} \right]_{\tau^*} dS(\zeta_L) + \iint_S \left[\frac{L_r - L_M}{r^2(1-M_r)^2} \right]_{\tau^*} dS(\zeta_L) \\ & + \frac{1}{c_0} \iint_S \left[\frac{L_r\left(r\dot{M}_r + c_0 M_r - c_0 M^2\right)}{r^2(1-M_r)^3} \right]_{\tau^*} dS(\zeta_L) \\ & + \iint_S \left[\frac{U_n\left(r\dot{M}_r + c_0 M_r - c_0 M^2\right)}{r^2(1-M_r)^3} \right]_{\tau^*} dS(\zeta_L) \end{aligned} , \qquad (3.75)$$

where a dot indicates differentiation with respect to τ. Equation 2.75, with the volume quadrupole term neglected, is known as formulation 1A of Farassat [117]. It forms the basis of the acoustic propagation code and, except the neglecting of the quadrupole term, is exact and therefore valid both in the near and far field.

3.12. Summary

This chapter has presented details of the numerical methods employed in this research. Developing the whole SotonCAA code is long-term teamwork during past 10 years. Each researcher may have developed their own functionalities for specific cases. For the landing gear case, I implemented the artificial selective damping method to stabilize the simulation and generalized the 'CFDtoFWH' code to adopt the three-dimensional integration surface with arbitrary shape. The implementation of the function of artificial selective damping is provided in the Appendix B.

Chapter 4
Landing Gear Noise Prediction Using High-order Finite Difference Schemes

4.1. Introduction

Recently, numerical simulations that compute unsteady flows around landing gears have been attempted to investigate the noise sources and the radiated sound fields. A number of unsteady flow simulations have been performed for landing gear models at various levels of geometrical complexity. Most the flow simulations in the previous studies were based on the conventional CFD. The recent advances in high-order accurate, low dispersive and dissipative CAA techniques discussed in Chapter 3 were not attempted in those simulations. The implementation of the CAA methods may improve the fidelity and efficiency of landing gear flow and noise calculations, which is the scope of the current work.

In this chapter, the CAA/FW-H hybrid technique based on high-order finite difference schemes is applied for a two-wheel generic landing gear model, of which wind-tunnel test data were made available by Airbus. Compressible DES is performed by using 4th-order prefactored compact finite difference schemes and buffer-zone non-reflecting boundary conditions. The current simulation involves 1604 blocks of fully structured meshes where many of them have singular block interfaces across which the gradients of mesh surfaces are discontinuous. The characteristics-based block interface treatment is used in order to avoid the discontinuity problems associated with the high-order finite difference schemes. The details of the computed flow field are presented in this chapter, in which both the wheel surface pressure and the mean flow velocity field are compared with experimental data. The aerodynamic flow data are then used as source terms on the integration surface in a Ffowcs Williams and Hawkings (FW-H) solver to predict the far field noise levels and directivity patterns. The radiated noise in the far field is also compared with the experimental data. Individual contribution of

wheels, axle and strut to the total noise is investigated separately. In addition, the individual noise signals are analyzed in conjunction with the unsteady flow data from the corresponding components, which helps understand the physical mechanism of landing gear noise generation. The organization of the present chapter is as follows. In section 4.2, the model geometry and grid generation are described. Computation setup is presented in section 4.3. In section 4.4, the aerodynamic results are presented including mean flow comparisons and unsteady flow features. In section 4.5, the acoustic results are discussed, and the noise sources are investigated. Finally, a summary is made in section 4.6.

4.2. Model Description and Grid Generation

The simulated model is a scaled generic landing gear, including a main strut, an axle and two wheels. The scale approximately corresponds to 1:2.5 of a nose landing gear for Airbus A320 (wheel diameter of 300 mm and the main strut length of about 690 mm). The strut and axle are circular cylinders and the bottom of the strut is a hemi-sphere. The configuration of the current landing gear model is depicted in Fig. 4.1.

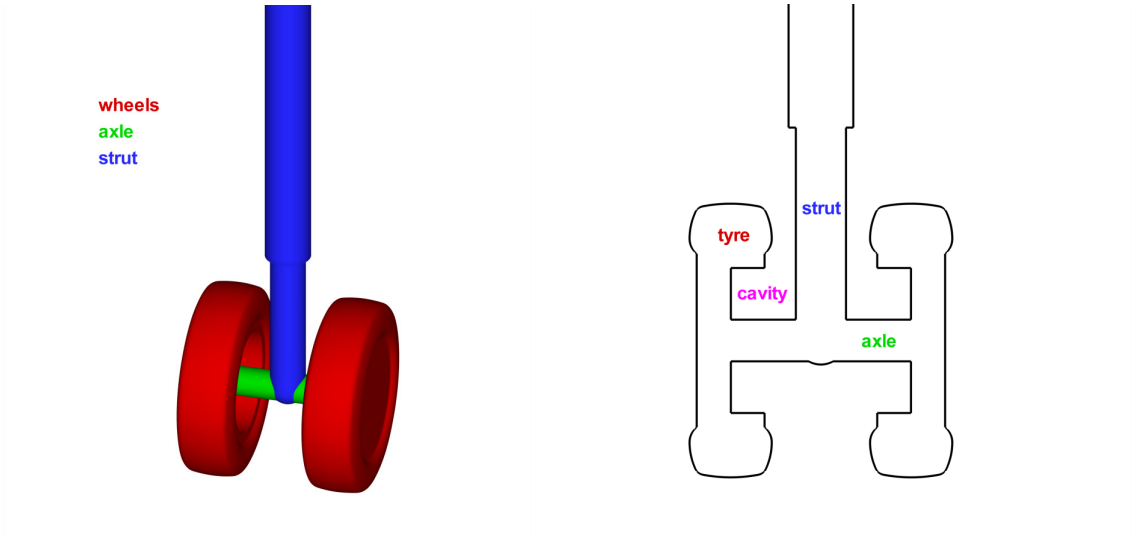

Figure 4.1: Drawings of the current two-wheel landing gear model.

The flow conditions in the simulation are provided from the aerodynamic measurement performed in the closed-section wind tunnel F2 [71] in Toulouse, France.

The acoustic measurement is operated in the CEPRA19 [7] wind tunnel in Saclay, France. The free-stream Mach number is 0.23, the air density is 1.18 kg/m^3 and the static temperature is 293.56 K.

The entire landing gear model is surrounded by a multi-block structured grid, which is generated using commercial software GRIDGEN [85]. Due to the geometric complexity, a total number of 1604 hexahedral blocks are generated to accommodate the landing gear model in a domain of 11D, 6D and 5D in the streamwise, vertical and spanwise direction, respectively, as described in Fig. 4.2. The wheel diameter (D) is used as a reference length in the followings.

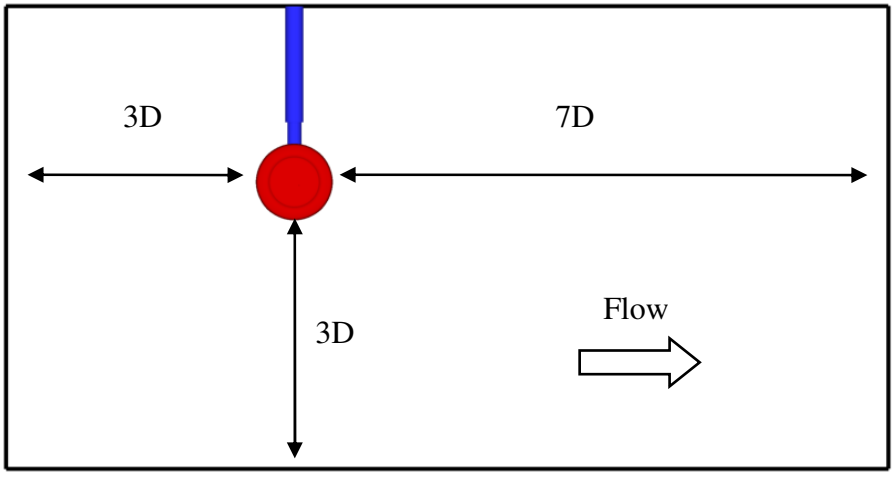

Figure 4.2: Schematic of the computational domain.

The grid is technically split into a near-wall RANS region and the outer LES region. Within the near-wall RANS region, the cells next to the wall surface have a thickness to wheel diameter ratio of 1×10^{-4} and are stretched on a growth ratio of 1.1. This wall-surrounding layer consists of 16 grid points normal to the surface and has very high cell aspect ratio. In the LES region, cubic cells are used in as much area as possible. The blocks that enclose the wheel surface have 122 cells distributed over the circumference. Each block in the computational domain is one-to-one connected, and communicates with characteristic interface conditions. Buffer zone boundary conditions are applied in the outer boundaries of the domain to remove the reflecting sound waves. The complete baseline grid has approximately 3.5 million grid points. Fig. 4.3 and 4.4 show the structured mesh topology on the z=0 and y=0 plane, respectively. During the

mesh construction, the stretching angle of the cells is controlled to be larger than 40 degree, to avoid the stability issue complained by the finite difference solver with sharp cell angles. Fig. 4.5 shows the surface meshes distributed over the landing gear walls. A refined grid is also tested in order to investigate the effect of grid resolution to the acoustic spectrum. The mesh refinement focuses mainly on the improvement of resolution on the wheel surface (from 122 to 240 cells on the circumference), keeping the same resolution in the direction normal to the wall, which results in 15.7 million cells in total.

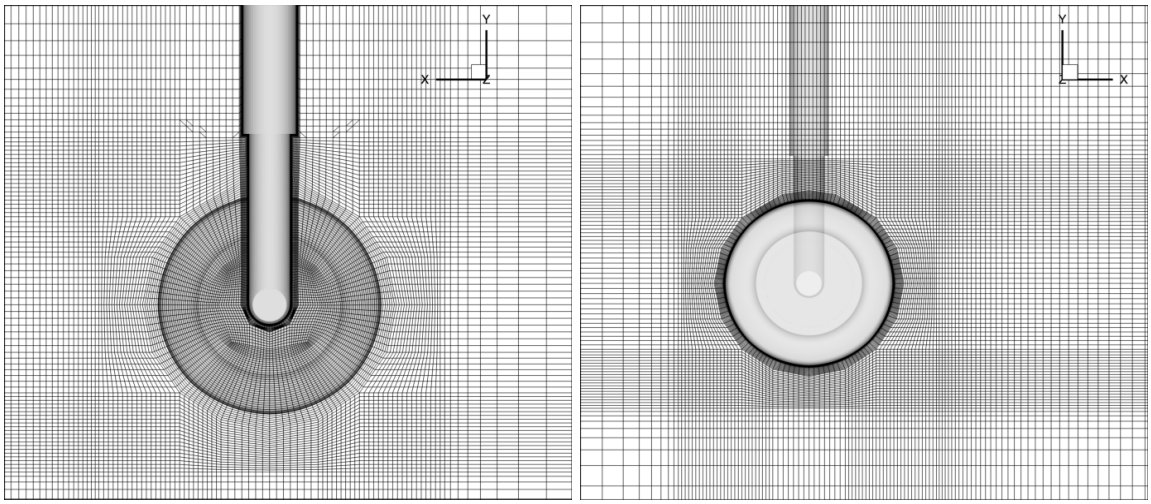

Figure 4.3: Structured mesh topology on the z=0 plane.

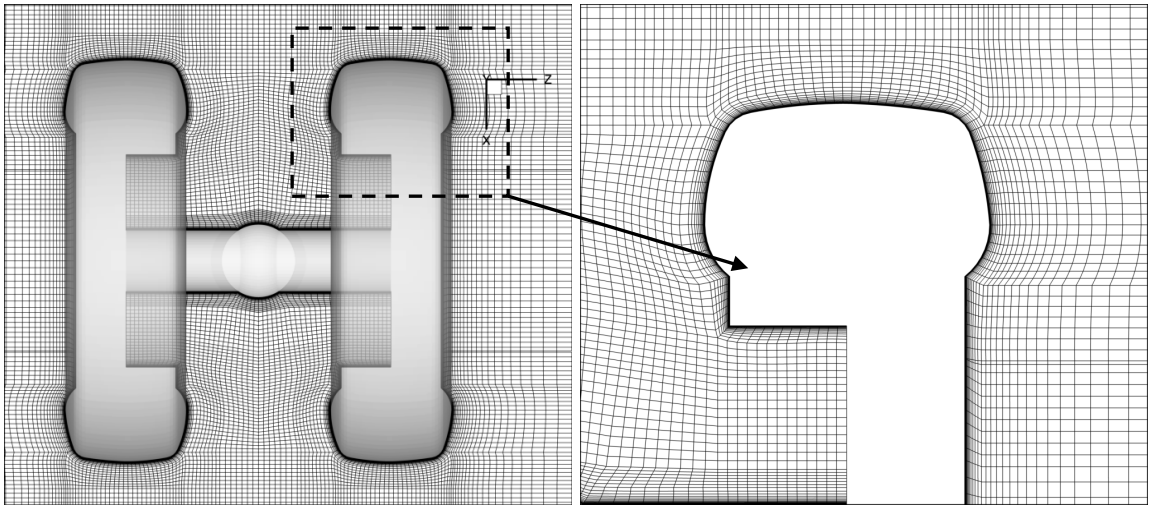

Figure 4.4: Structured mesh topology on the y=0 plane.

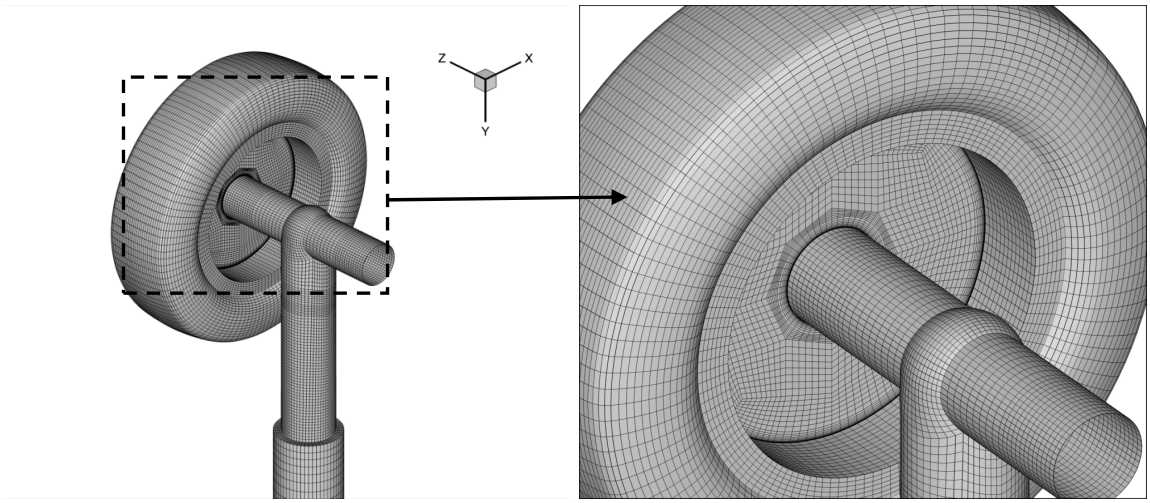

Figure 4.5: Surface mesh distributed over the landing gear walls.

4.3. Computational Setup

The current calculations are performed in a parallel computing cluster by using domain decomposition and Message Passing Interface (MPI) libraries. Dimensionless time step size of 0.001 normalized by the sound speed and wheel diameter is used, which corresponds to the CFL number of 8.2. The incoming flow is assumed fully turbulent and no laminar/turbulent transition is imposed in the simulation. Approximately 90000 time steps are required to reach a fully developed flow field from an impulsive initial condition used. The current calculations (on the baseline and the refined grid) are run in two supercomputing clusters Spitfire and IRIDIS3 available at the University of Southampton. The Spitfire cluster is provided by Microsoft Institute for High Performance Computing which was created at the University of Southampton in 2005. The IRIDIS3 cluster was launched in 2010 and is one of the largest and fastest supercomputers in UK, which offers 8064 processor-cores providing over 72TFlops and up to 32GB of memory per node. The calculations are parallelized over 48 and 256 processors in the Spitfire and the IRIDIS3 cluster, respectively. The baseline calculation runs up to around 200 time steps per physical hour in the Spitfire cluster and 1000 time steps per hour in the IRIDIS3 cluster. The refined calculation yields around 250 time steps per physical hour in the IRIDIS3 cluster.

In the radiation model, the FW-H surface is positioned to enclose as many noise potential sources as possible, which means it is normally an off-body permeable surface.

However, the risk of using permeable surface is that noise predictions might be contaminated by errors caused by large wake fluctuations passing through the surfaces [13]. To avoid this problem, the FW-H surface is placed on the landing gear solid surface in our simulation (exactly match the CFD surface grid). For low Mach numbers, the dipole sources are dominant over the quadruple sources. Therefore, it is reasonable that only the dipole surface sources are included in the far field noise predictions. In practice, the body-fitted FW-H surface is also useful to examine the noise contribution from each individual landing gear component. The velocity components on the solid surface are constantly zero, therefore only the pressure data are required in this work to calculate the radiated noise.

4.4. Aerodynamic Results

In this section, the results of time-averaged pressure and velocity are compared with the existing measurement data for the validation of the current calculation. Instantaneous flow characteristics are visualized and discussed afterwards in order to describe the noise generation mechanism.

4.4.1. Validation of Time-Averaged Flow Data

Time-averaged pressure distribution on the landing gear model surface is compared with the measurement data provided by Airbus France from the F2 wind tunnel test performed in [71]. The current surface pressure data are collected at the same locations of the 64 static pressure taps (shown in green) used in the F2 wind tunnel test as shown in Fig. 4.6. In the azimuthal direction, 0° indicates the direction of free-stream flow. The landing gear model was mounted upside-down in the F2 wind tunnel, and the left and right sides refer to the relative positions when the observer is facing the free-stream flow. The left wheel has 37 pressure taps (Nos. 1-37) around the tire circumference on the median plane of the wheel, 8 taps (Nos. 40-47) cross-aligned at the wheel top, and 2 taps on the horizontal plane near 0° (Nos. 38-39). The right wheel has 3 taps on the horizontal plane near 0° (Nos. 48-50). The axle contains taps in two sections at ±45.5 mm from the strut. The right section has one tap at 0° (No. 55). The left section has 4 taps at 0° (No. 51), 90° (No. 52), 180° (No. 53), and 270° (No. 54). The strut contains

taps in one circular section and in one straight line. The circular section is located at 120 mm below the axle, and it has 5 taps at 0° (No. 60), -45° (No. 59), -90° (No. 58), -135° (No. 57), and -180° (No. 56). The tap No. 60 is also the first tap of the straight line of 5 taps (Nos. 60-64) evenly spaced by 20 mm along the strut at 0° (stagnation line).

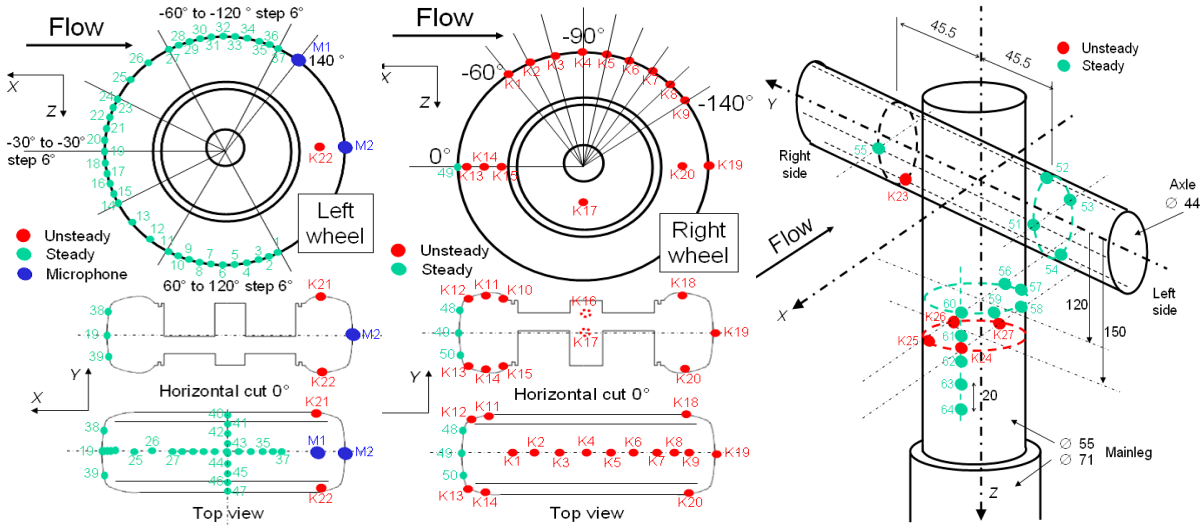

Figure 4.6: The location of pressure taps on left wheel, right wheel, axle and strut. (from Ref. [71])

Figure 4.7 shows the distribution of time-averaged pressure on the left wheel circumference from 120° to -120° (Nos. 1-37). The pressure levels match very well with the experimental data at most of the locations, except the tap No. 33 where a local discontinuity in pressure occurs in the experimental data. According to Fig. 4.6, the tap No. 33 is located at an angle of -96° on the left wheel, which is close to the top-side of the left wheel. Since there is no geometric discontinuity around that location, it is speculated that the discontinuity in mean pressure might be attributed to an artifact in the measurement. Two meshes provide similar time-averaged pressure distribution on the left wheel surface.

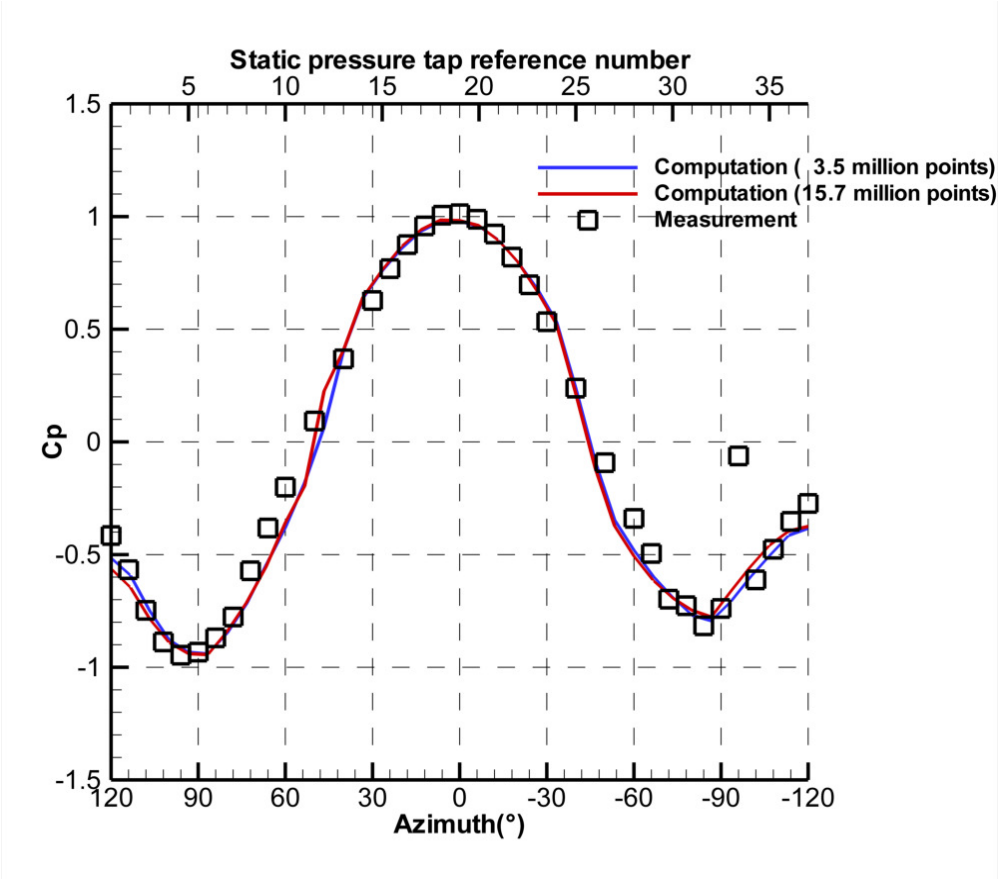

Figure 4.7: Time-averaged pressure distribution on the left wheel circumference.

Figure 4.8 shows the distribution of time-averaged pressure on the rest parts of the landing gear model (Nos. 38-64). The calculated pressure levels on the wheel surface (Nos. 38-50) match very well with the measurement data. There are some disagreements on the axle and the strut surface, especially at the tap No. 58. Referring to Fig. 4.6, No. 58 is located near a flow separation point. The disagreement may be due to the boundary layer tripping used in the experiment. The boundary layer tripping was implemented along the circular dots shown in Fig. 4.9 aligned at ±60° with respect to the free-stream direction. The disagreements on the axle and strut surface might be more related to the lack of numerical resolution. The refined mesh provides better comparisons with the measurement as expected.

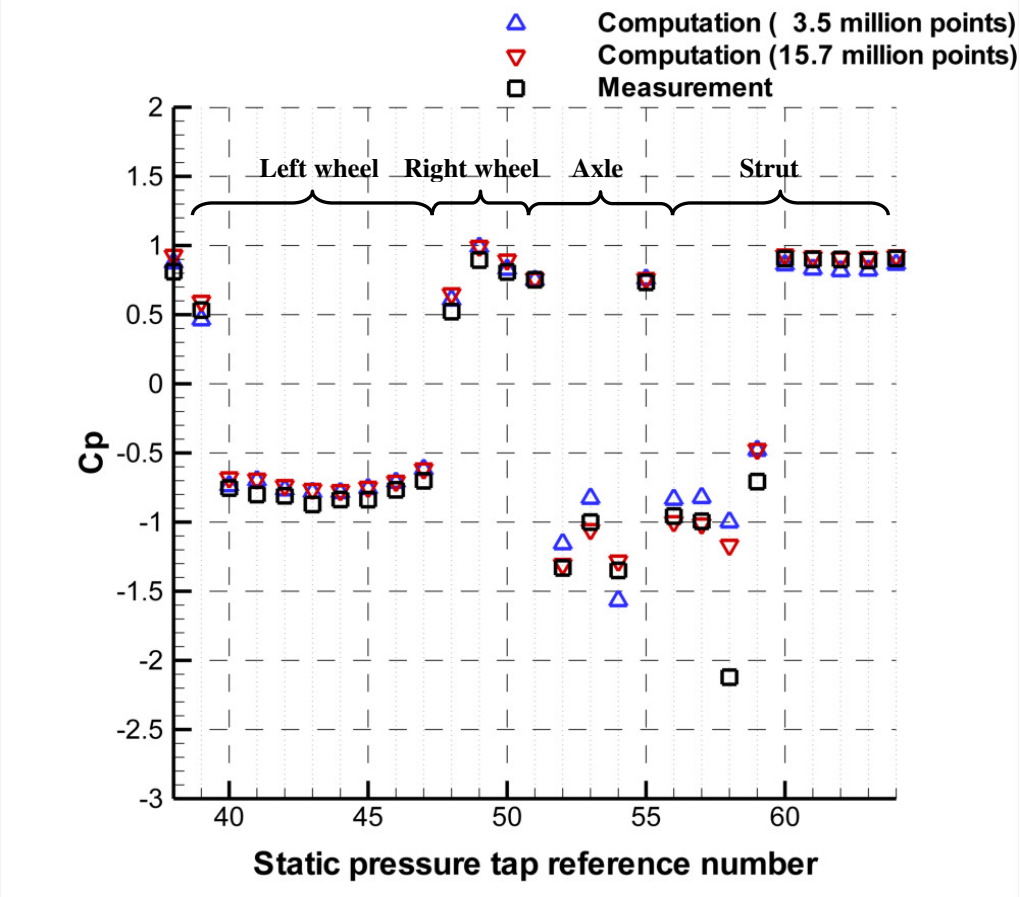

Figure 4.8: Time-averaged pressure distribution on the rest of the landing gear model.

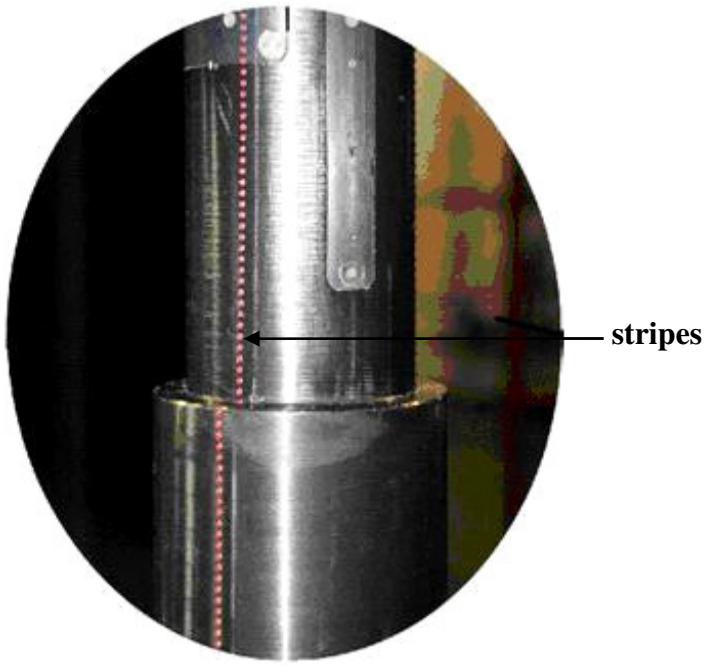

Figure 4.9: Boundary layer tripping in the F2 measurement (from Ref. [71]).

In the following section, the downstream flow field is presented based on the results from the refined grid, because strong numerical dissipation occurs in the wake region when coarse grid is used. Calculated mean velocities are compared with the existing particle image velocimetry (PIV) measurement data from [71] on two different horizontal planes in Figs. 4.10 and 4.11. The streamwise velocity contours are plotted at the top of the figures and the spanwise velocity contours are at the bottom. They show a reasonable agreement on the time-averaged velocity field in the downstream wake region of the wheels. It is noticeable that the areas in which separated flows merge behind the wheels are slightly different between the computation and the measurement. The computation has a relatively larger merging region with lower streamwise velocity and higher transverse velocity than the measurement does. The calculation also has relatively thicker boundary layers around the wheels, which might be due to numerical dissipation associated with the turbulence model and low-order wall boundary treatment used. The agreement between the calculation and the measurement improves significantly in the strut region as shown in Fig. 4.10 as the level of geometric complexity decreases.

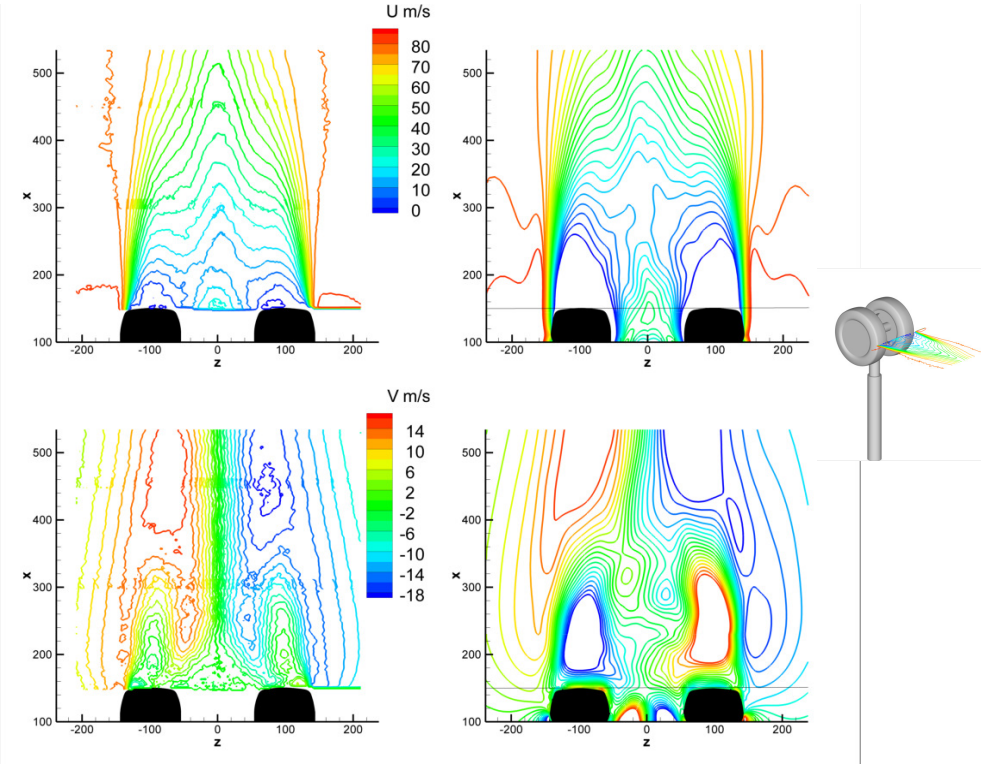

Figure 4.10: Time-averaged velocity contour plots on a horizontal plane bisecting the axle: PIV measurements (left) and current calculation (right).

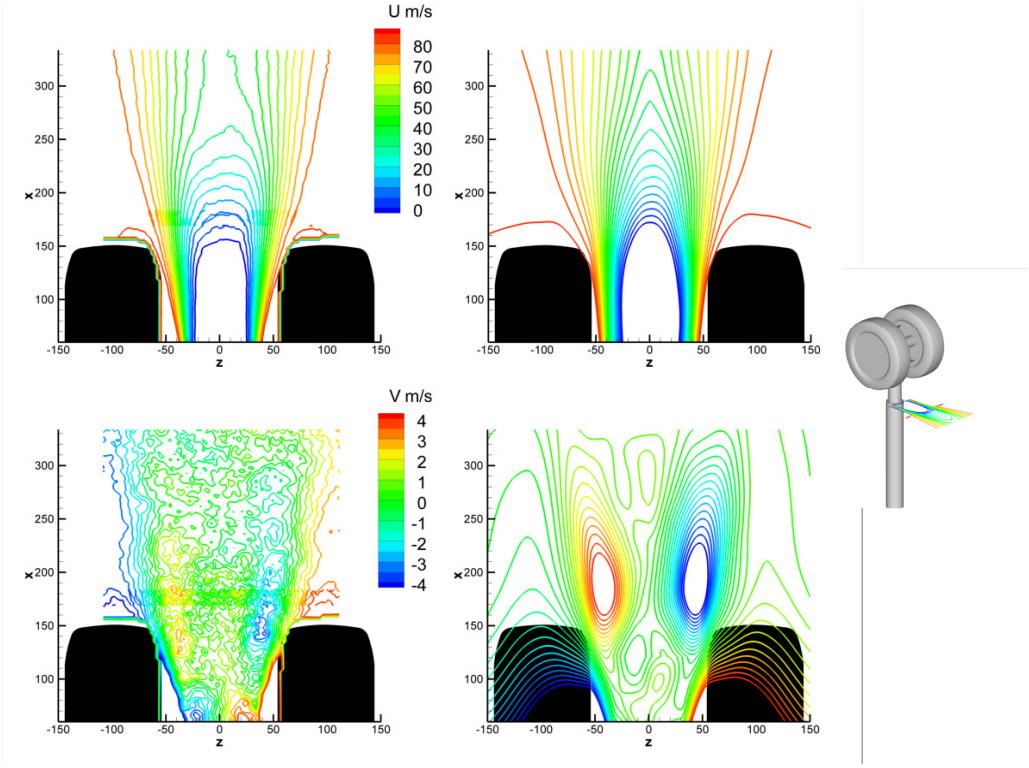

Figure 4.11: Time-averaged velocity contour plots on a horizontal plane crosscutting the strut: PIV measurements (left) and current calculation (right).

4.4.2. Investigation of Unsteady Flow Field

Landing gear aerodynamic noise is strongly correlated with the unsteady pressure fluctuations on the landing gear surfaces. Therefore, investigating the unsteady flow field around the landing gear model can help understanding the noise mechanism. The unsteady surface pressures were monitored in the computation and compared with the experimental data collected by the unsteady pressure sensors distributed on the wheel and strut surfaces (see Fig. 4.6). The power spectral density (PSD) comparisons at different unsteady pressure sensor positions (K14 and K24) are depicted in Figs. 4.12 and 4.13. K14 is located on the front shoulder of the right wheel, and K24 is located on the strut in front of the incoming flow. Good agreements (tonal peaks are well captured) can be found up to 1-2 kHz in the frequency range, above which energy fall-off occurs in the computation. This frequency cut-off is common in the landing gear computation [5, 6, 84, 86, 87], and is caused by grid resolution combined with the numerical dissipation induced by the numerical methods. The discrepancy below 200 Hz is also

expected, since a high-pass filter has been applied on the experimental data for the frequencies below 200 Hz resulting low PSD levels from the measurement.

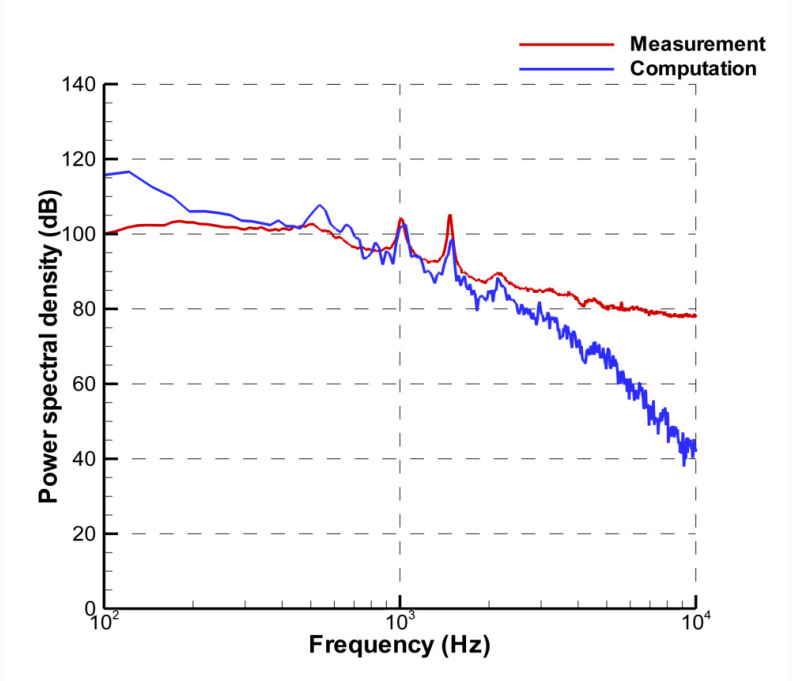

Figure 4.12: Surface pressure PSD comparisons at K14.

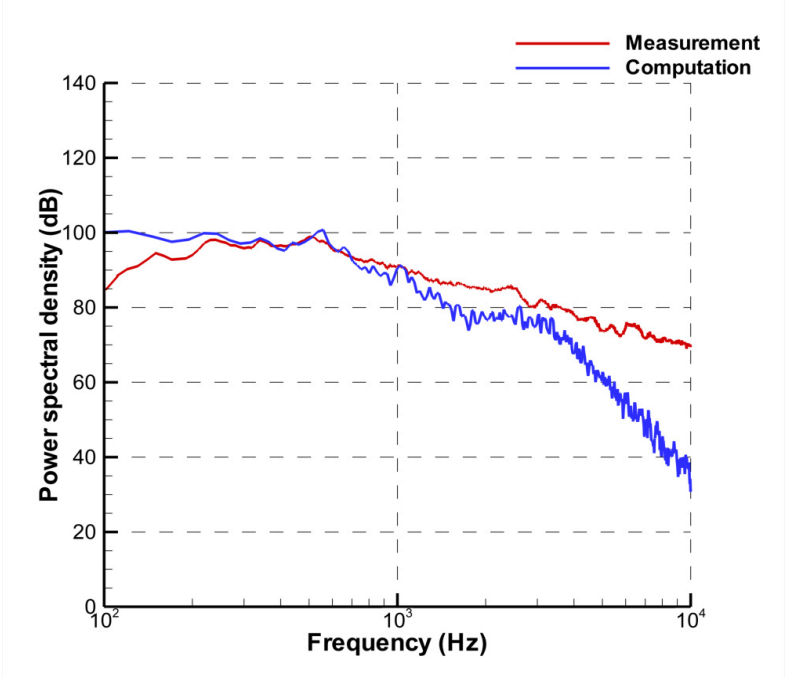

Figure 4.13: Surface pressure PSD comparisons at K24.

Figure 4.14 and 4.15 show instantaneous contour plots of velocity magnitudes on two different horizontal planes and two vertical planes, respectively. The velocity magnitude is defined as

$$Umag = \sqrt{u^2 + v^2 + w^2}\ , \tag{4.1}$$

where u, v, and w denote velocity components in the streamwise, spanwise and vertical directions respectively. In some plots, the right wheel of the landing gear has been removed for a clear view in between the wheels. Figure 4.14(a) visualizes a large irregular wake generated by the two wheels and the axle, and Fig. 4.14(b) shows a rather regular vortex shedding from the strut (a circular cylinder). It is made clear in Fig. 4.15 that the scale of wake turbulence from the wheels is larger than that from the axle and the strut, which may suggest that the wheels are the primary source of low frequency noise. Three-dimensional vortical structures of the flow are shown in Fig. 4.16, which indicates fully three-dimensional broadband noise generation of the complex geometry. The pressure coefficient is defined as

$$Cp = \frac{2(p - p_\infty)}{\rho U_\infty^2 D}\ , \tag{4.2}$$

where p is the instantaneous pressure, p_∞ is the ambient pressure, ρ is the density, and U_∞ represents the free-stream velocity. It should be noted that there is a significant drop in numerical resolution in the far wake after 2.5 times of the wheel diameters from the strut.

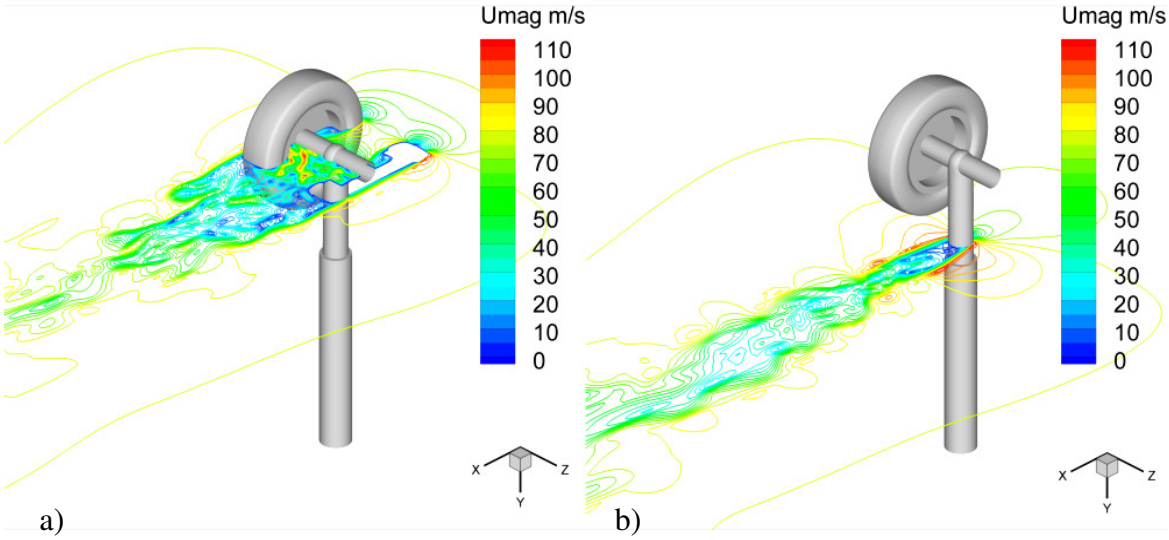

Figure 4.14: Instantaneous contour plots of velocity magnitudes on two horizontal planes: a) bisecting the axle and b) crosscutting the strut.

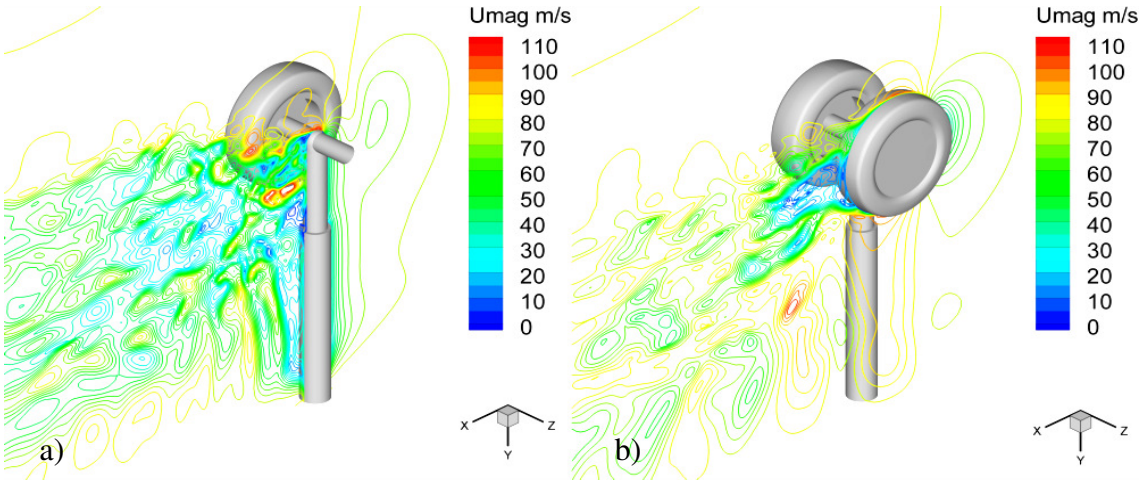

Figure 4.15: Instantaneous contour plots of velocity magnitudes on two vertical planes: a) bisecting the strut and b) bisecting the right wheel.

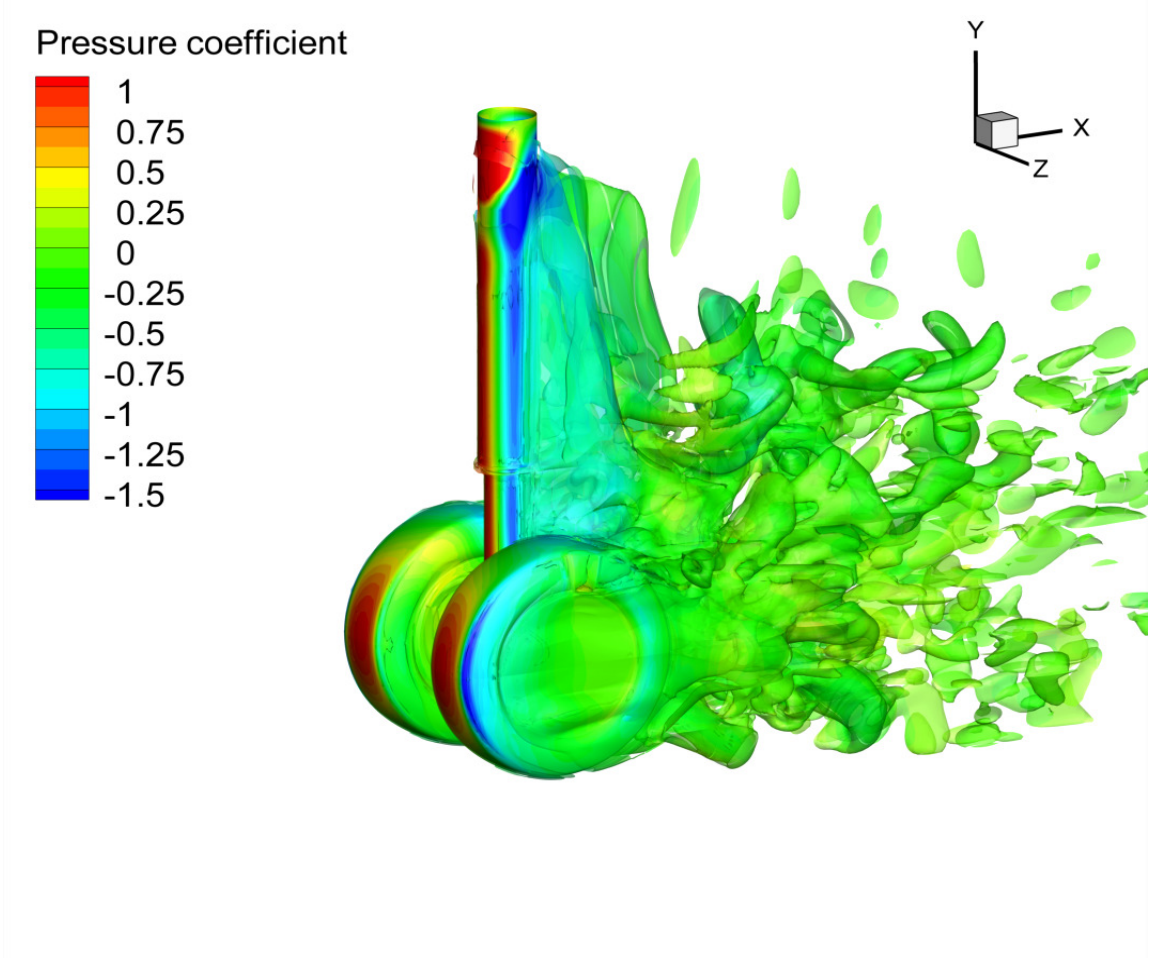

Figure 4.16: Three-dimensional iso-vorticity contour-surfaces colored by pressure coefficient.

Figure 4.17 shows an instantaneous plot of pressure coefficients and streamlines on a horizontal plane bisecting the axle and on the landing gear surface. It is conjectured from Fig. 4.17 that the axle/strut junction between the wheels may be the secondary source of noise. The recirculation zone forming a large vortex inside the front area of the wheel cavity is observed to cause strong flow impingement onto the front surface of the axle. The impingement with unsteadiness in the vicinity may significantly contribute to the noise.

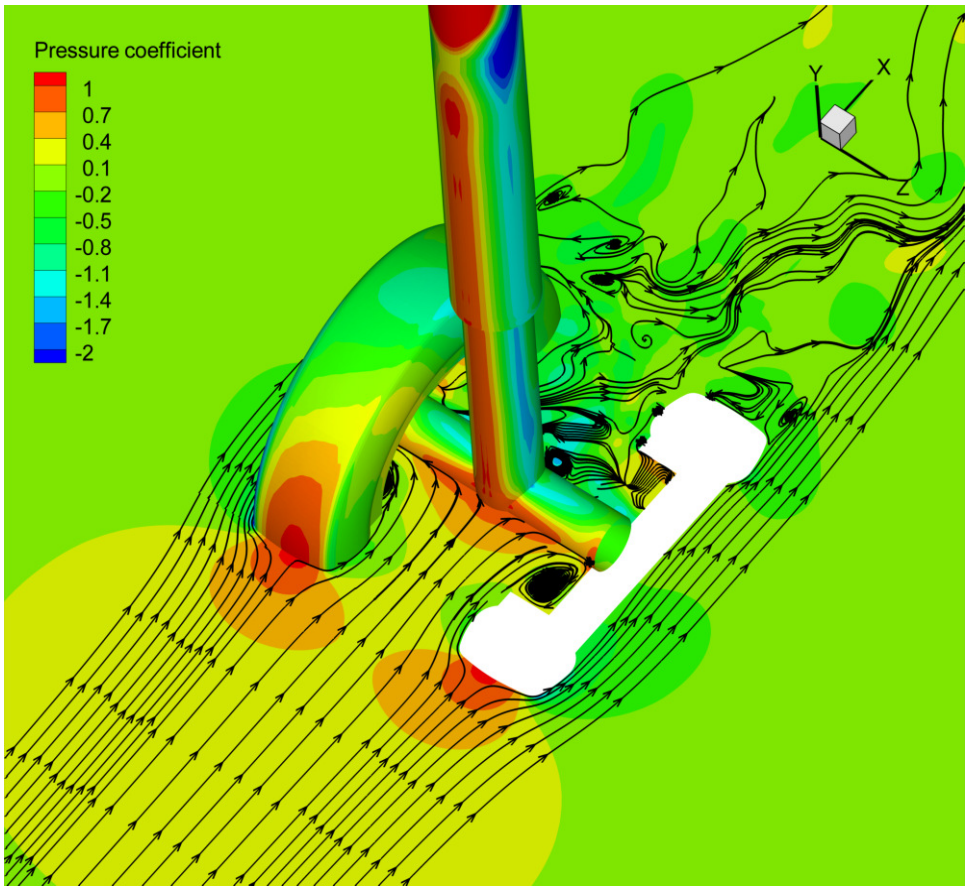

Figure 4.17: Contour plots of pressure coefficients with streamlines around the landing gear.

In order to estimate the level of unsteadiness in the flow, the following quantity is defined:

$$I = \frac{1}{N}\sum_{i=0}^{N}(p_i - \overline{p})^2 / p_\infty^2 , \tag{4.3}$$

where I denotes dimensionless intensity of pressure fluctuation, N is the number of samples, p is the instantaneous pressure, $\overline{p}$ represents the time-averaged pressure, and p_∞ is the ambient pressure. This measure of pressure fluctuations is useful to identify potentially significant noise source regions particularly around the body surfaces. Figure 4.18 reveals some local spots where the high level of pressure fluctuations dominates. The level of pressure fluctuations is highest in the vicinity of the impingement region mentioned in the above, which suggests that the axle may potentially be a major noise

contributor to the landing gear noise. A further investigation on this is detailed in the next section.

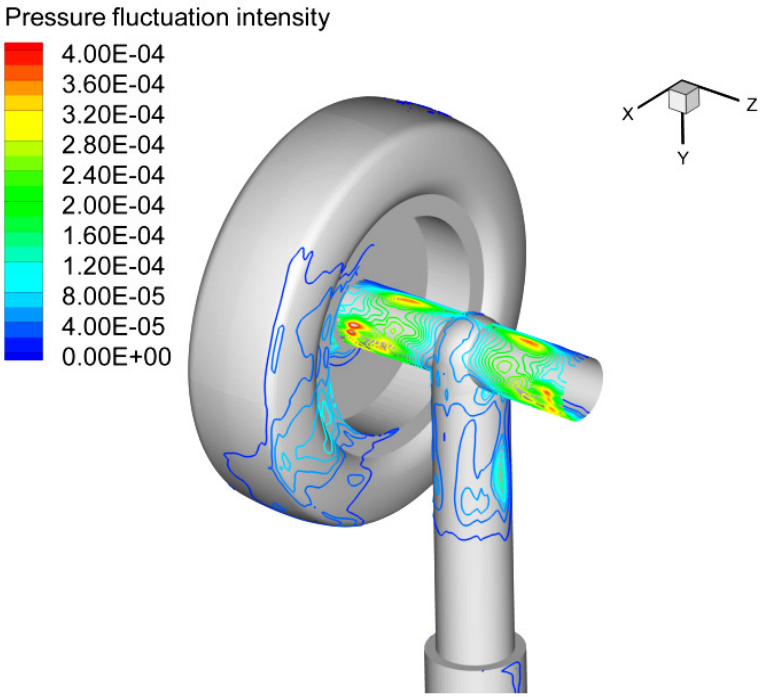

Figure 4.18: The intensity of pressure fluctuations by Eq. (4.3) on the axle and strut surfaces.

4.5. Acoustic Results

The FW-H calculations are performed and the radiated sound is discussed in this section. The resulting sound spectra are produced based on 7 groups of 1024 samples of surface pressure data (7168 samples in total). Each data group is treated by Hann's window [118] ensuring zero mean in the data prior to Fast Fourier Transform (FFT). The frequency bin width is 11Hz. The results of the 7 data groups are then averaged to get a statistically converged spectrum (ensemble average).

4.5.1. Comparison with Experiment

Power spectral density (PSD) levels are compared between the current computation and the CEPRA19 anechoic wind tunnel measurement in Ref. [7]. Figure 4.19 demonstrates the microphone setup in the wind tunnel for the far field acoustic signal collection. Two

microphone arcs are fixed 6000 mm away from the model, and 12 microphones are positioned every 10° along each arc (from 30° to 140° in the azimuthal direction). There are two additional microphone arrays and the distance between the microphone arrays and the landing gear model is 2000 mm.

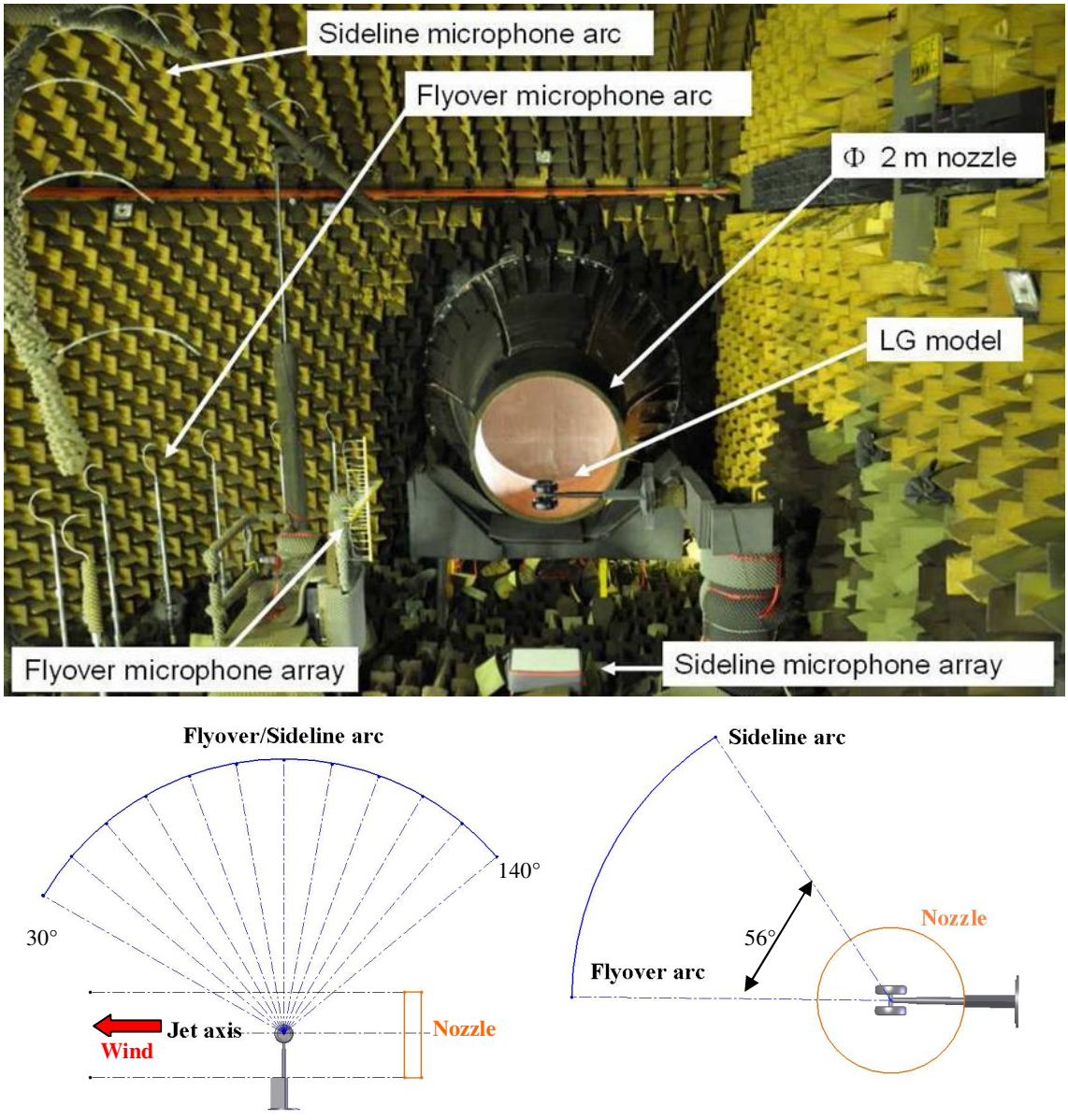

Figure 4.19: Microphone setup for the measurement of far field acoustic signal. (from Ref. [7])

For accurate comparison with the current calculation, the experimental data are corrected from the background noise, the atmospheric absorption and the refraction through the open-jet wind tunnel [119]. Figure 4.20 compares the PSD levels between

the computation and CEPRA19 measurement on the far field flyover microphone arc at 140° in the azimuthal direction. Good agreement is achieved in the frequency range from approximately 200 Hz to 2 kHz. The discrepancy in the very low frequency range (below 200 Hz) is due to the high-pass filter applied on the experimental data for the frequencies below 200 Hz. The energy fall-off occurs in the mid to high frequency range around 2 kHz is caused mainly by numerical dissipation associated with the grid density as well as the numerical methods. Cells with high aspect ratio within the RANS region might not have been effective enough to capture high wave-number components particularly in the circumferential direction.

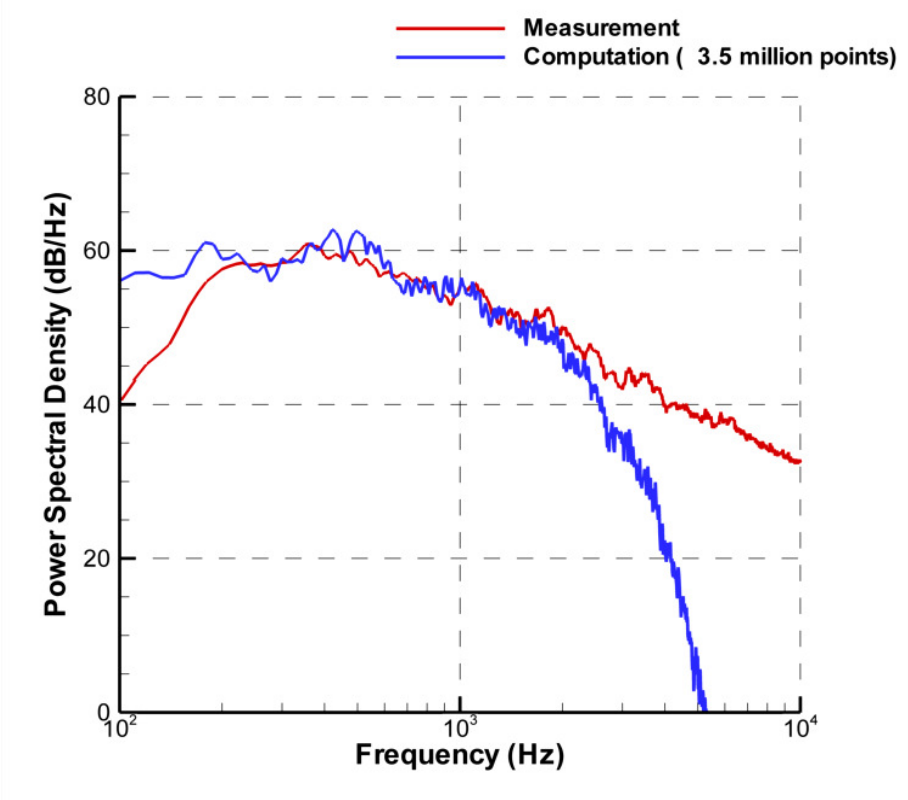

Figure 4.20: PSD comparison on the far field flyover microphone arc at 140°.

To investigate the effect of grid density on the acoustic spectrum, a grid refinement is made in the circumferential direction as mentioned in section 4.2. The number of grid points around the wheel circumference is increased from 122 to 240, resulting in the total grid points of 15.7 million. Major parameter changes after the grid refinement are shown in Table 4.1.

Table 4.1: Comparison between the baseline and the refined grids.

	Baseline grid	Refined grid
Total number of grid points	3.5 million	15.7 million
Number of grid points over the wheel circumference	122	240
Minimum wave length captured on wheel surface (assuming 10 PPW)	77.2 mm	39.2 mm
Maximum resolvable frequency	4.4 kHz	8.6 kHz

Figure 4.21 shows the improvement of acoustic prediction by using the refined grid. The microphone is at the same position as that used in Fig. 4.20. The fall-off frequency, after using the refined grid, is delayed from 2 kHz to 4 kHz approximately. Figure 4.22 shows additional PSD plots from two other microphones: one at the far field sideline arc (140°) and the other at the center of the sideline array, respectively. In general, the calculated PSD levels from the refined grid agree well with the measurement over a frequency range up to approximately 4 kHz. The tonal frequency peaks are also accurately predicted as shown in Fig. 4.22(b).

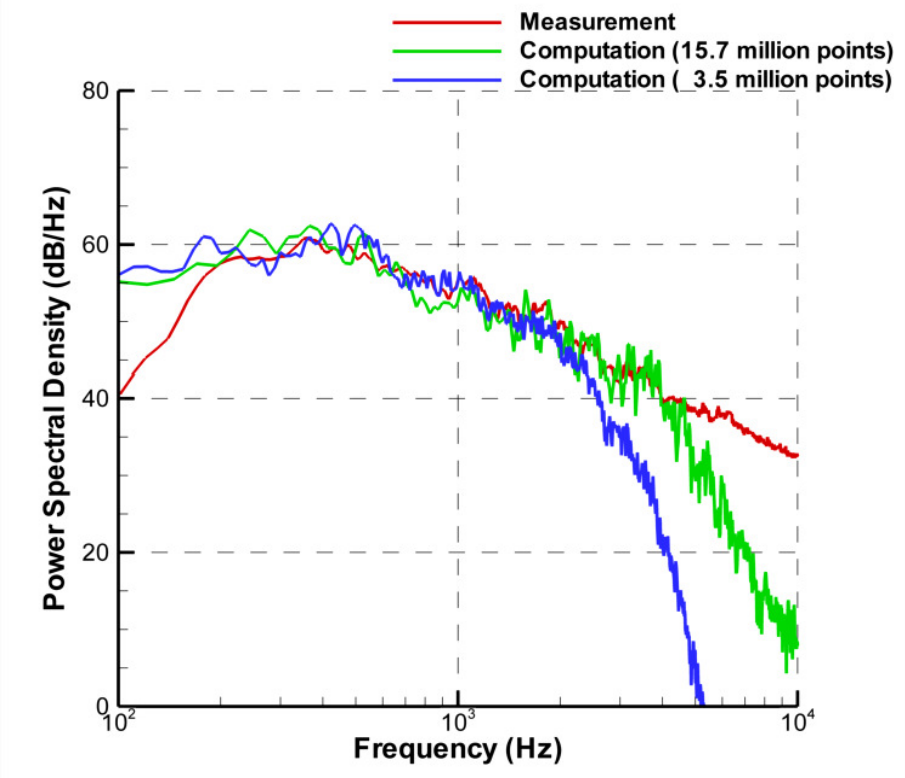

Figure 4.21: PSD comparison on the far field flyover microphone arc at 140°.

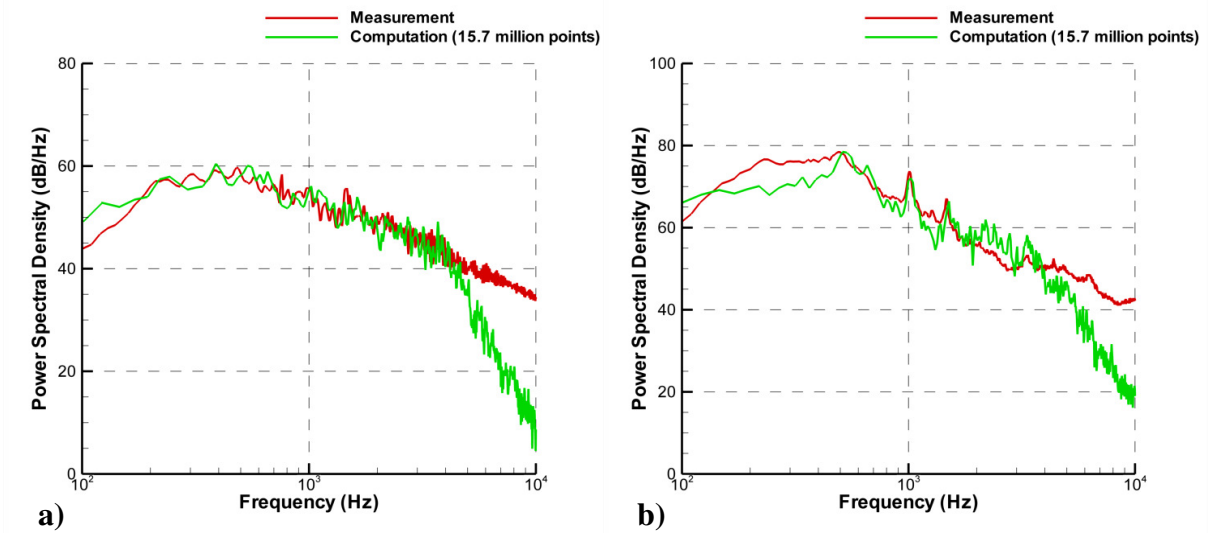

Figure 4.22: PSD comparisons: a) on the far field sideline microphone arc at 140°; b) at the center of the sideline microphone array.

It is shown that the current methodology and grid used offers accurate acoustic prediction up to a frequency of about 4 kHz. It is necessary to investigate on the effect of the energy fall-off at 4 kHz in the spectrum on the accuracy of overall sound pressure level (OASPL) prediction, i.e. as to whether the energy in the frequency spectrum above 4 kHz contributes significantly to the OASPL. Figure 4.23 shows the comparison of OASPL profiles obtained by the current prediction and the reference measurement across a range of different microphone locations. It can be seen from Fig. 4.23 that the far field OASPL prediction is generally in good agreement with the measurement, within 2 dB of deviation. This suggests that most of the noise source is prevalent up to 4 kHz and the energy fall-off at the frequency does not make a significant impact on the overall sound prediction. It should be noted that the OASPL agreement seems to get better towards the upstream direction as shown in Fig. 4.23.

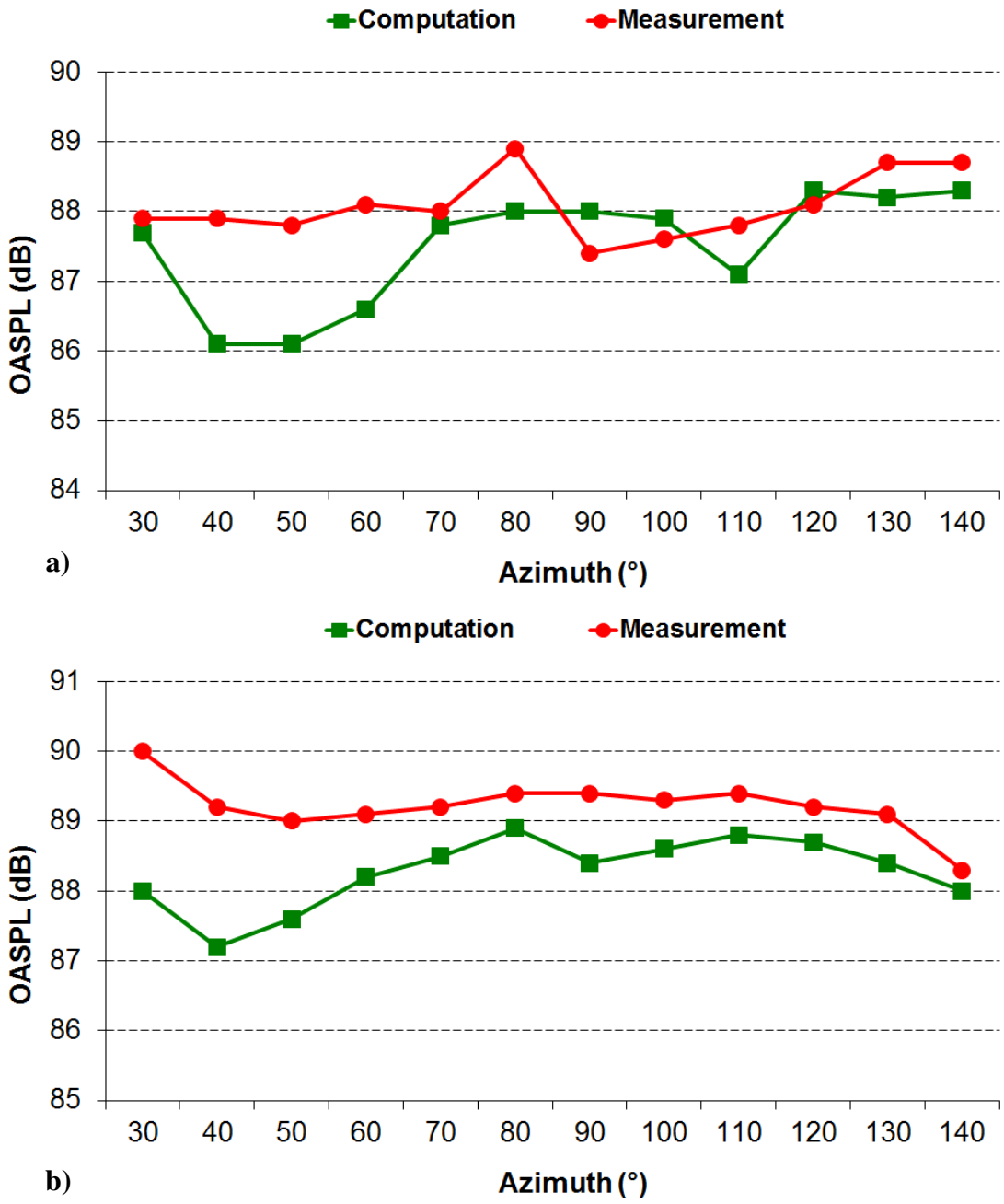

Figure 4.23: Far field OASPL comparisons on a) flyover and b) sideline microphone arcs.

4.5.2. Noise Sources Identification

In this work, noise contribution from each individual gear component is investigated by applying the on-body FW-H surface to axle, strut and wheel separately in an independent manner. This approach does not take into account the effect of interference from the other components that are excluded from the FH-W surface used for one

component. Therefore, there exists a certain level of uncertainty in this approach but it may well be used as a reasonable tool to compare noise contribution from different parts of the landing gear. Figure 4.24 shows the locations at which the far field OASPL of each component is calculated in flyover and spanwise directions, 20 diameters away from the landing gear axle center.

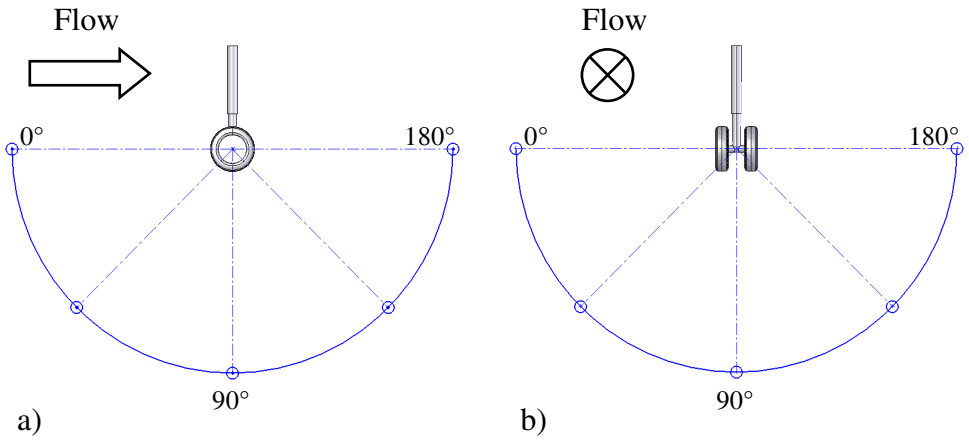

Figure 4.24: Far field observer positions in a) flyover and b) spanwise directions.

Figure 4.25 presents the contribution of each individual landing gear component to OASPL at various azimuthal locations indicated in Fig. 4.24. The individual contributions are compared with the original OASPL that included all the components. The wheels, which have the largest exposed area to the incoming flow, turn out to be prevalent as expected in almost all directions except around 90 degrees where the axle becomes dominant over the wheels by 2 to 3 dB. It is believed that the strong axle noise is attributed to the high intensity of pressure fluctuations on the axle surface discovered at the end of section 4.4 (Fig. 4.18). The contribution of the strut is generally weaker than the other components; however it radiates relatively strong noise towards 0 and 180 degrees in Fig. 4.24-a) as well as -b) which indicates a typical dipole sound pattern due to its cylindrical shape.

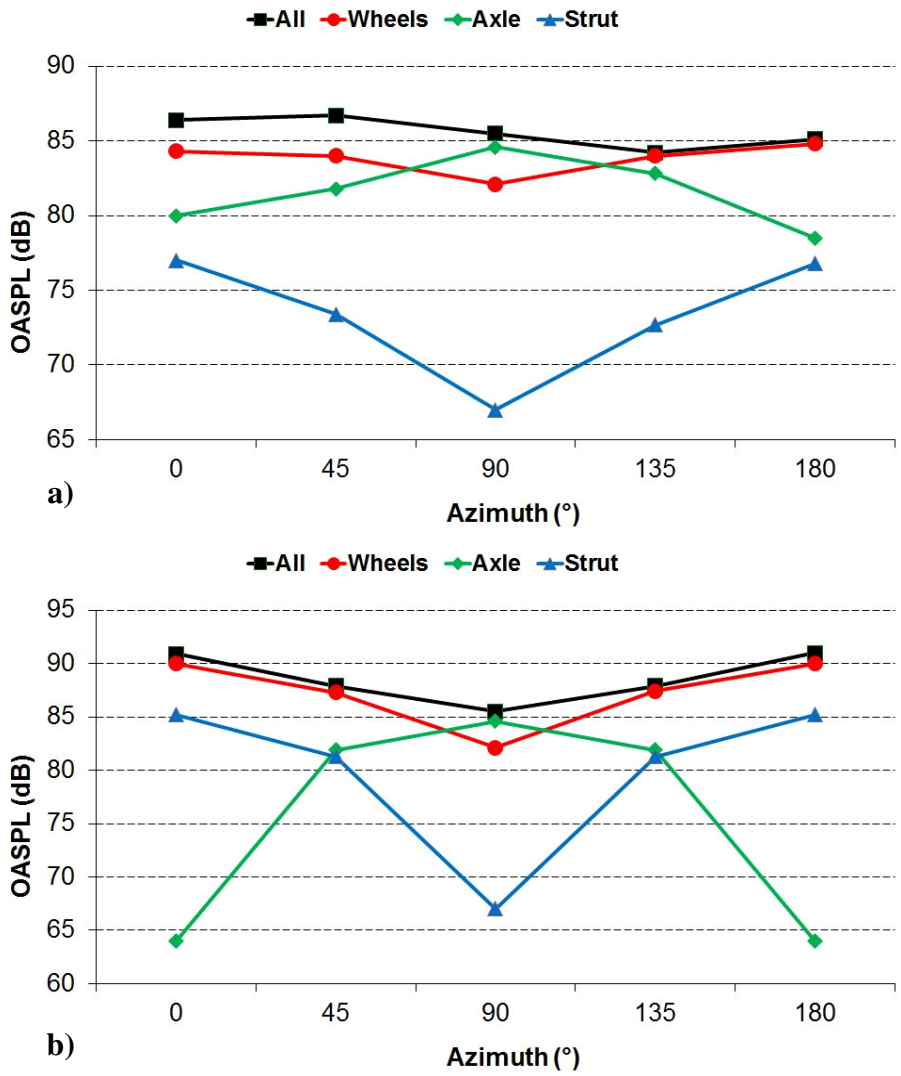

Figure 4.25: The noise contribution from landing gear component in a) flyover and b) spanwise directions.

4.6. Summary

The high-order computation of landing gear noise is presented in this chapter. It is demonstrated that a multi-block structured grid combined with high-order finite differencing schemes and a novel block-interface condition leads to reliable aeroacoustic solutions in such a highly complex geometry. Both aerodynamic and acoustic results compare well with the existing wind tunnel measurement data provided by Airbus France for the 1:2.5 scaled model of an A320 noise landing gear at the free-stream Mach number of 0.23. Narrow band acoustic PSD (power spectral density) spectra are well predicted in a frequency range up to 4 kHz for this particular landing

gear model. Although the baseline grid with 3.5 million points was suitable for mean aerodynamics, the refined grid with 15.7 million points was required to increase the highest resolved frequency range in the acoustic PSD spectra from 2 to 4 kHz. The increased frequency range is shown to be sufficient for accurate prediction of OASPL (overall sound pressure level) within 2 dB deviation from the experimental measurement. The investigation of individual gear components suggests that the wheels emit most of the noise in general but the axle contributes significantly in the direction straight down to the ground (overhead direction from an observer). The axle noise, which is associated with strong surface pressure fluctuations due to impinging flows separated from the wheels, may be potentially higher than the wheel noise in that particular direction.

Chapter 5
Landing Gear Noise Prediction Using Low-order CFD

In this chapter, the commercial engineering simulation software FLUENT [120] is used for a conventional CFD study of the two-wheel generic landing gear model. The model is identical to that described in Chapter 4 so that the numerical comparison between the high-order SotonCAA code and the conventional CFD method can be performed. The FLUENT CFD solver coupled with the built-in FW-H solver is used to calculate the sound radiation following the hybrid acoustic prediction strategy. The organization of the present chapter is as follows. In section 5.1, the computational setup is presented, in which the computing efficiencies are investigated by the comparison between SotonCAA and FLUENT. The details of the FLUENT-computed flow field are presented in section 5.2, compared with both experimental data and the results from SotonCAA. In section 5.3, the acoustic results are discussed, and the landing gear model is decomposed to individual components for noise sources identification. Finally, a summary is made in section 5.4.

5.1. Computational Setup

The grid in the FLUENT simulation is identical to the baseline (coarse) grid used in Chapter 4, which has approximately 3.5 million grid points with 122 cells distributed over the wheel circumference. The cell next to the wall has a thickness to wheel diameter ratio of 1×10^{-4} and is extruded using a growth ratio of 1.1. This wall-surrounding layer consists of 16 cells normal to the wall which intends to capture the boundary layer and results in a y^+ value mostly below 10, see Fig. 5.1. The red spots (high y^+ value) at the junction of the axle and the wheel-inside wall are the result of the relatively coarse mesh distribution in the turbulent inactive area. The red spots in the other areas indicate the high flow speed regions where flow accelerations and

separations occur. The flow conditions are initialized as the same as those used in Chapter 4, i.e. with freestream velocity of 78 m/s, the air density of 1.18 kg/m^3 and the static temperature of 293.56 K. It should be mentioned that all the FLUENT/SotonCAA comparisons given in this chapter are based on the same baseline (coarse) grid.

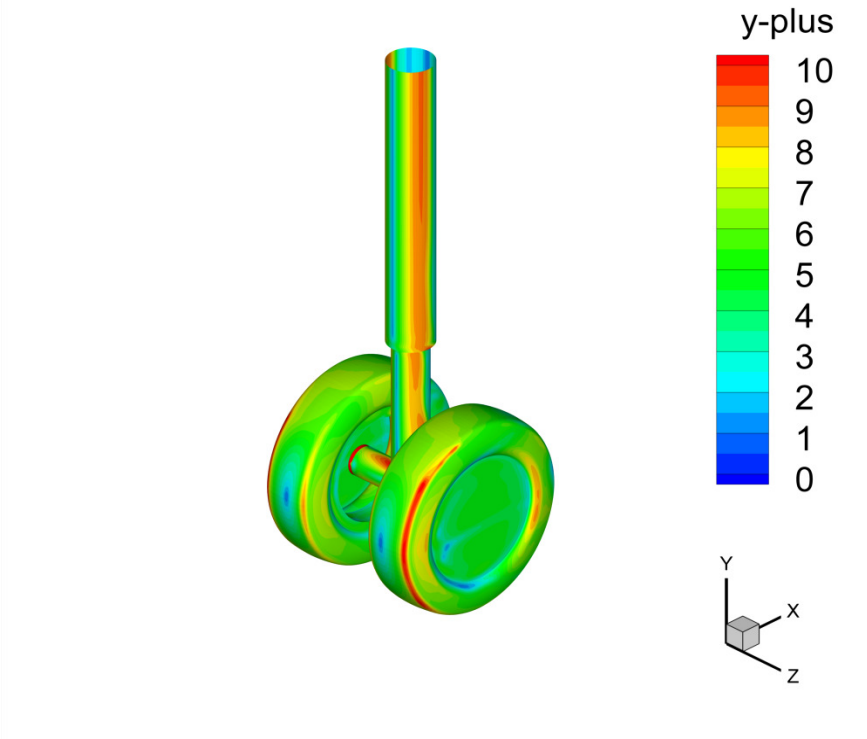

Figure 5.1: y^+ distributions over the landing gear surface.

FLUENT (version 6.3.26) is based on the finite volume methods and has various flow modeling capabilities and a separate module for acoustic calculations. The compressible Navier-stokes equations are solved by the three-dimensional, double precision, pressure-based unsteady solver with second-order accurate schemes in space and time, see Table 5.1.

Table 5.1: Discretization schemes used in FLUENT.

Variable	Scheme
Pressure	Second order
Momentum	Second order upwind
Modified turbulent viscosity	Bounded central differencing
Energy	Second order upwind

The turbulence model in the simulation is DES with S-A one equation model adopted in the RANS region. The velocity inflow condition specifies the incoming flow speed and temperature at the inflow boundary. The symmetry boundary conditions are applied on the top, bottom and side boundaries of the computational domain. The pressure far field boundary condition is used for the outflow, which uses characteristic information (Riemann invariants) to determine the flow variables at the outflow boundary.

The FLUENT simulation is performed on the Spitfire cluster, utilizing a total of 16 processors (restricted by the FLUENT user license). Initially, a steady-state computation is carried out to obtain a fully developed flow field and to investigate the grid quality for the turbulence model. Subsequently, the time-accurate computation is started with time step size of 3×10^{-5} second, during which a particle in the free-stream would travel a distance of one wheel diameter in about 130 time steps. Table 5.2 compares the computing efficiencies between FLUENT simulation and the high-order SotonCAA simulation. For stability reasons, SotonCAA requires smaller time step size in the time advancement. Thus, it takes relatively longer computing time for the flow developing than that in FLUENT, though the computing cost for each time step is much smaller.

Table 5.2: The computing efficiencies on the different platforms.

	FLUENT	SotonCAA	
Computing platforms	Spitfire	Spitfire	IRIDIS3
Total number of processors	16	48	256
Time step size (second)	3×10^{-5}	8.8×10^{-7}	8.8×10^{-7}
physical time per step (hour)	0.1	0.005	0.001
Computing cost for a particle traveling a distance of one wheel diameter (hour)	15.4	21.7	4.3

5.2. Aerodynamic Results

In this section, the results of time-averaged pressure and velocity are compared with the measurement data for the validation of the FLUENT simulation. Instantaneous flow

characteristics are visualized and discussed afterwards in order to investigate the noise generation mechanism.

5.2.1. Validation of Time-Averaged Flow Data

The current surface pressure data are collected at the same locations of the 64 static pressure taps used in the F2 [71] wind tunnel test as shown in Fig. 4.6. Figure 5.2 shows the distribution of time-averaged pressure on the left wheel circumference from 120° to -120° (Nos. 1-37), with SotonCAA results plotted in blue and FLUENT results plotted in red. In general, the pressure levels calculated from FLUENT match very well with the experimental data. Slightly over predictions of the pressure levels can be spotted around the stagnation area (Nos. 15-24) of the left wheel surface, and under prediction of the pressure level occurs at -90° (No. 32) on the left wheel, which is around the top-side of the left wheel.

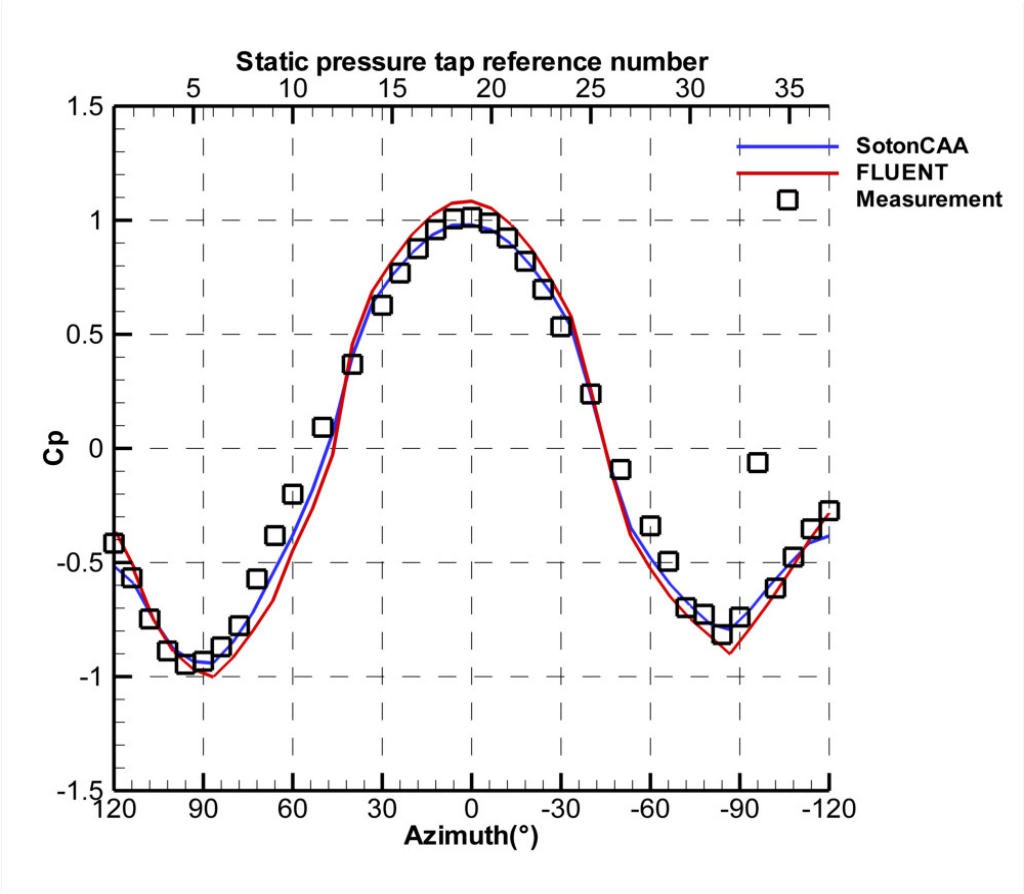

Figure 5.2: Time-averaged pressure distribution on the left wheel circumference.

Figure 5.3 shows the distribution of time-averaged pressure on the rest parts of the landing gear model (Nos. 38-64). Good agreement of pressure levels between FLUENT and measurement can be found at most of the positions. Over predictions occur consistently at the stagnation areas of the wheel surface (Nos. 49, 50) and of the strut surface (Nos. 60-64). We can notice that FLUENT makes a better prediction than SotonCAA at the tap No. 58, where potential flow separations happen. Overall, the time-averaged pressure on the landing gear surface calculated from SotonCAA has a relatively better agreement with the measurement than that from FLUENT. However, the better predictions from FLUENT near the flow separation regions suggest that FLUENT may have more solid performance on the no-slip wall condition and turbulence treatment close to the wall.

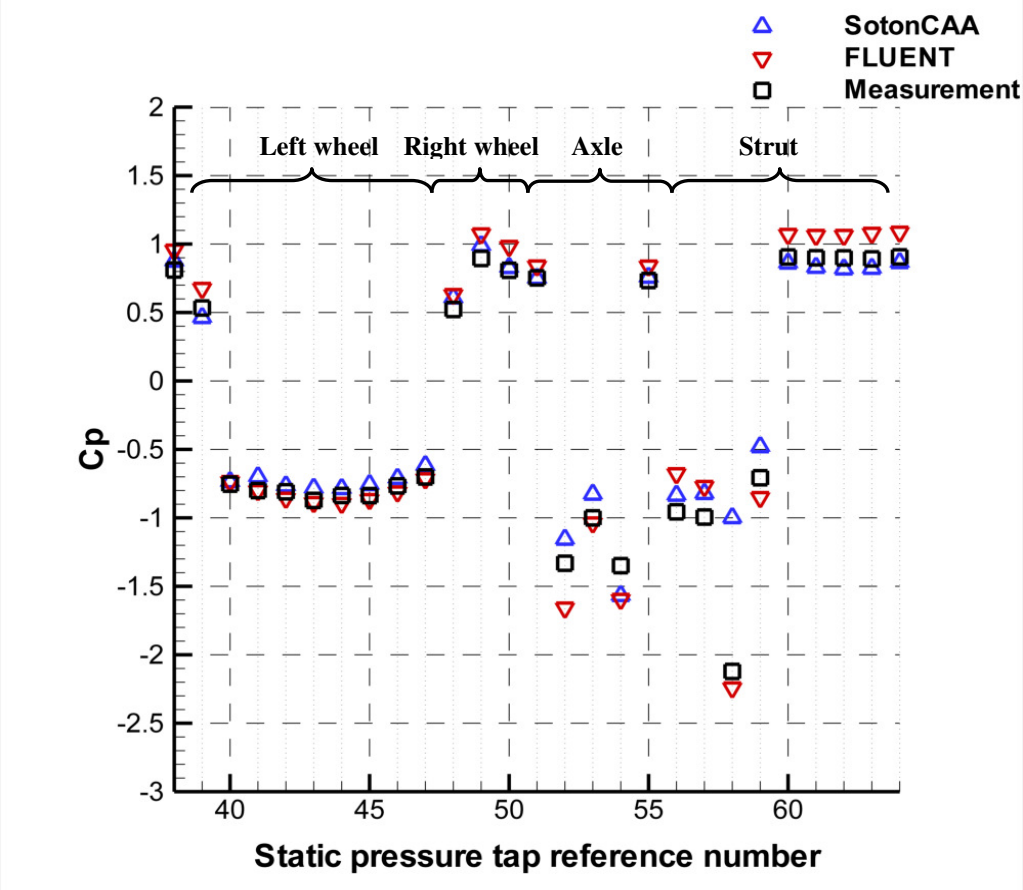

Figure 5.3: Time-averaged pressure distribution on the rest of the landing gear model.

Calculated mean velocities are compared with the PIV measurement [71] data on two different horizontal planes in Figs. 5.4 and 5.5. The streamwise velocity contours are plotted at the top of the figures and the spanwise velocity contours are at the bottom.

They show a good agreement on the time-averaged velocity field in the downstream wake region of the wheels. FLUENT velocity field does not have the larger merging region, with lower streamwise velocity and higher transverse velocity, which exists in the SotonCAA simulation shown in Fig. 4.10, and compares better with the measurement in the wake region of the wheels where the level of geometric complexity is very high. The difference in the velocity field between FLUENT and SotonCAA is believed to be the result of the varied performances of the finite volume and finite difference methods on complex geometries. The high-order CAA code is highly sensitive to the grid quality, especially to the grid with high level of geometric complexity. Therefore, the artificial dissipation and filtering schemes and low-order wall boundary treatments are adopted to maintain the numerical stability of the algorithms, which possibly induces strong numerical dissipation in the highly complex wake region. The finite volume based solver with the low-order discretizations is more adaptive and tolerant to complex geometries, and may have less stability requirement that introduces high numerical dissipations.

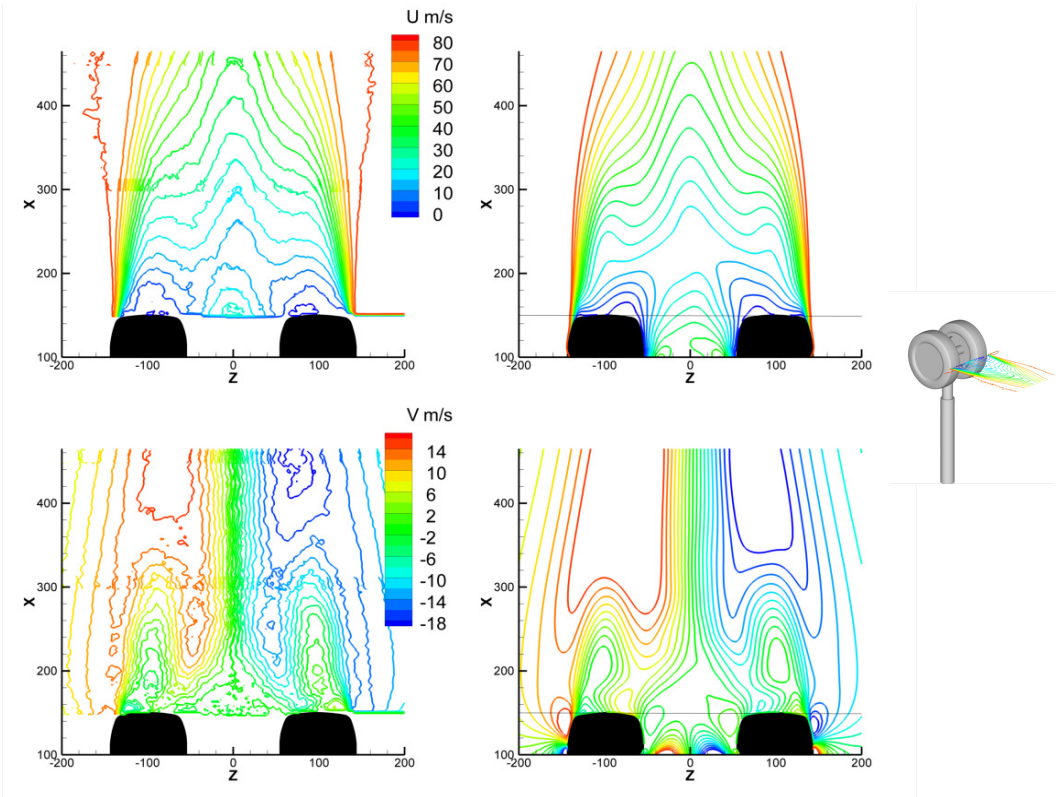

Figure 5.4: Time-averaged velocity contour plots on a horizontal plane bisecting the axle: PIV measurements (left) and current calculation (right).

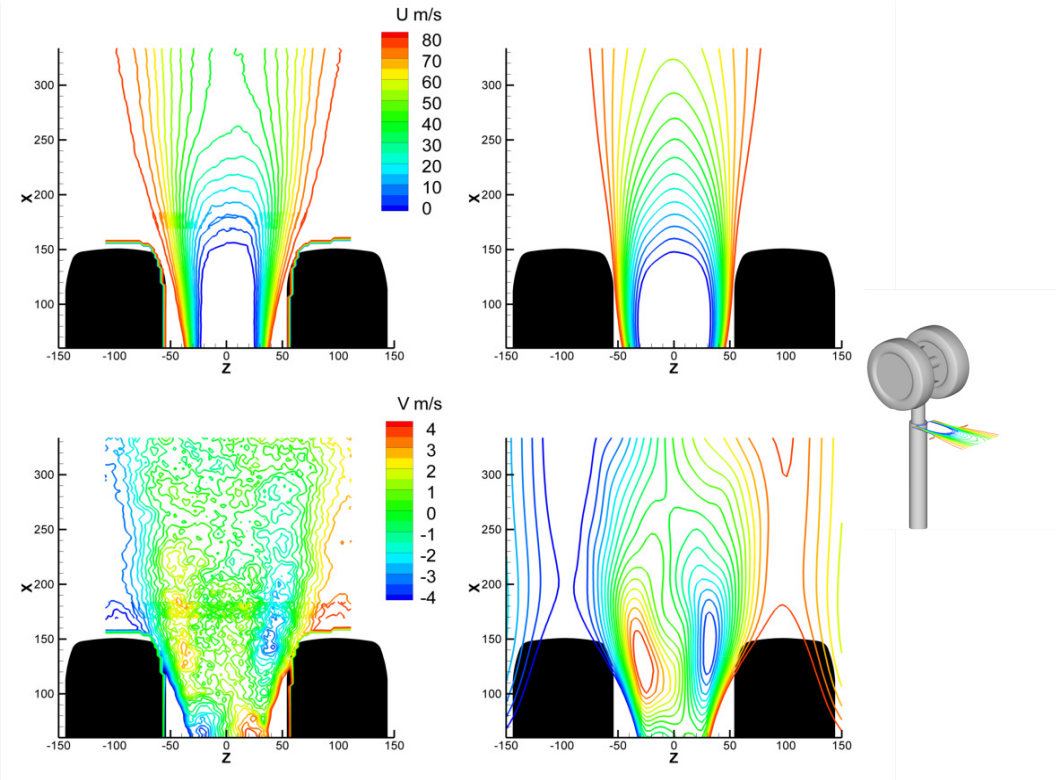

Figure 5.5: Time-averaged velocity contour plots on a horizontal plane crosscutting the strut: PIV measurements (left) and current calculation (right).

5.2.2. Investigation of Unsteady Flow Field

Landing gear aerodynamic noise is the result of the pressure fluctuations within the time-dependent unsteady flow. Therefore, investigating the unsteady flow field around the landing gear model can help understanding the flow related noise mechanism. Figure 5.6 and 5.7 show the instantaneous contour plots of velocity magnitudes and vorticity magnitudes on two different horizontal planes, respectively. The velocity magnitude is defined in Eq. (4.1). The vorticity measures the local rotation of fluid flow, the magnitude of which is defined

$$\Omega = \sqrt{\left(\frac{\partial w}{\partial y} - \frac{\partial v}{\partial z}\right)^2 + \left(\frac{\partial u}{\partial z} - \frac{\partial w}{\partial x}\right)^2 + \left(\frac{\partial v}{\partial x} - \frac{\partial u}{\partial y}\right)^2}, \tag{5.1}$$

where u, v, and w denote velocity components in the x, y and z direction respectively. The right wheel of the landing gear has been removed for a clear view in between the wheels. Figure 5.6(a) and 5.7(a) visualize a large irregular wake generated by the two

wheels and the axle. Strong vortex structures can be spotted in the cavities between the wheels and the axle. Figures 5.6(b) and 5.7(b) show a rather regular vortex shedding from the strut (a circular cylinder). Figure 5.8 and 5.9 show instantaneous contour plots of velocity magnitudes and vorticity magnitudes on two different vertical planes, respectively. It is made clear in Fig 5.9 that strong wake turbulences are generated from the wheels and the axle, which may be the potential noise sources. The scale of wake turbulence from the wheels is larger than that from the axle, which may suggest that the wheels are the primary source of low frequency noise. Three-dimensional vortical structures of the flow are shown in Fig. 5.10, which indicates fully three-dimensional broadband noise generation of the complex geometry.

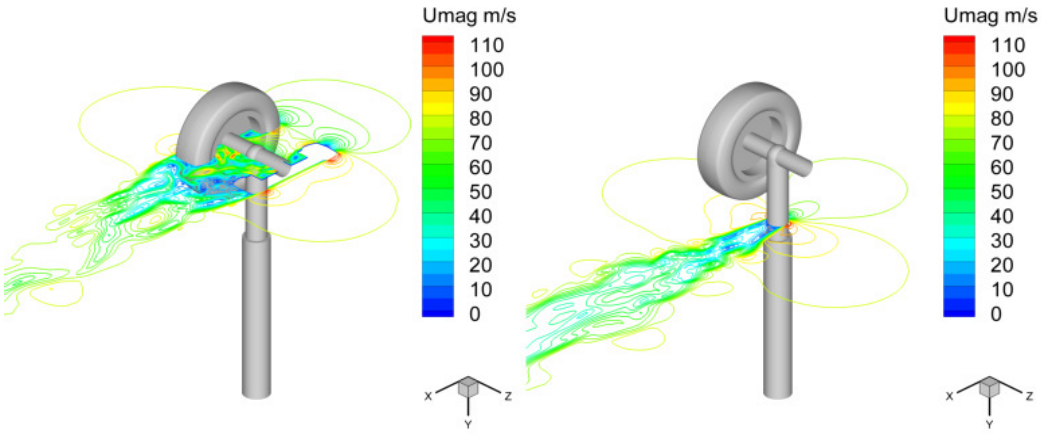

a) b)

Figure 5.6: Instantaneous contour plots of velocity magnitudes on two horizontal planes: a) bisecting the axle and b) crosscutting the strut.

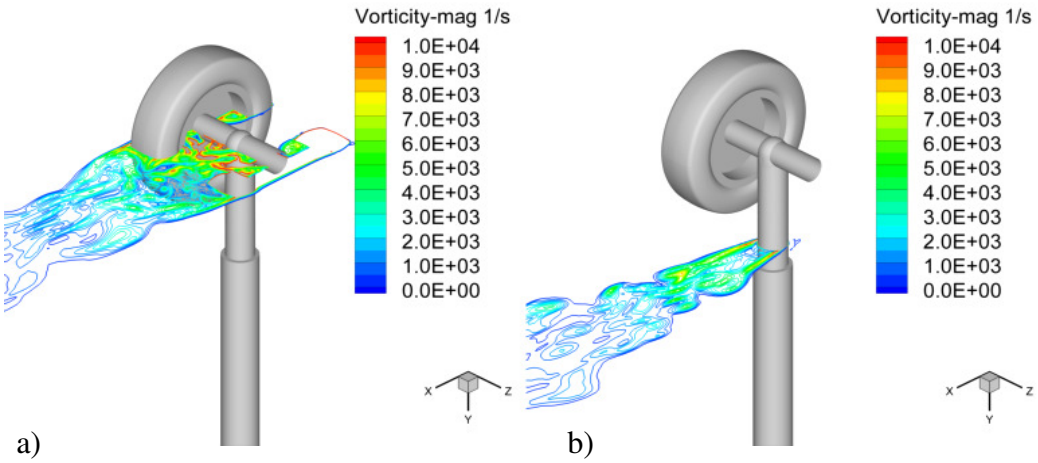

Figure 5.7: Instantaneous contour plots of vorticity magnitudes on two horizontal planes: a) bisecting the axle and b) crosscutting the strut.

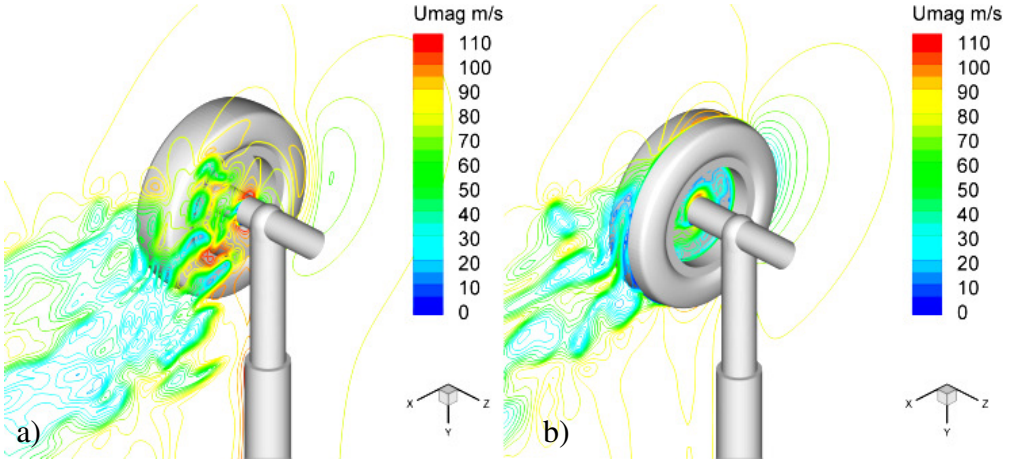

Figure 5.8: Instantaneous contour plots of velocity magnitudes on two vertical planes: a) crosscutting the axle and b) bisecting the left wheel.

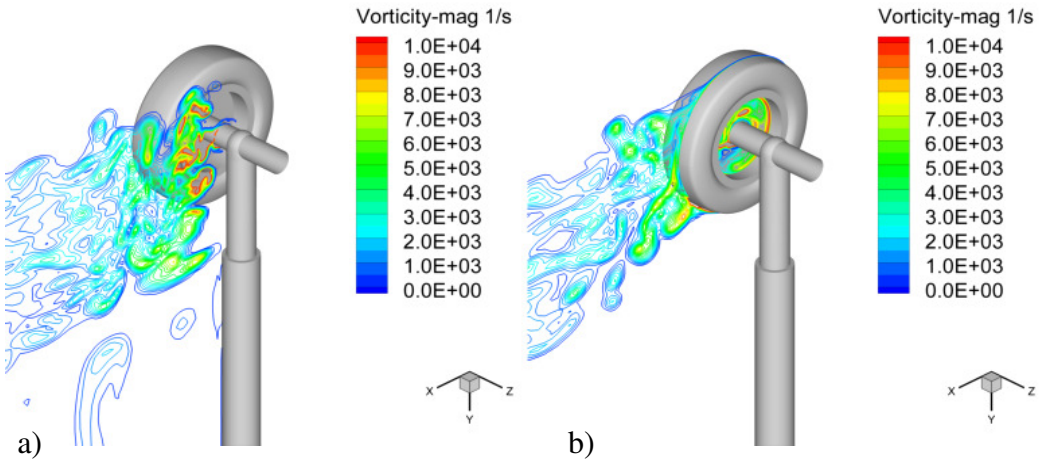

Figure 5.9: Instantaneous contour plots of vorticity magnitudes on two vertical planes: a) crosscutting the axle and b) bisecting the left wheel.

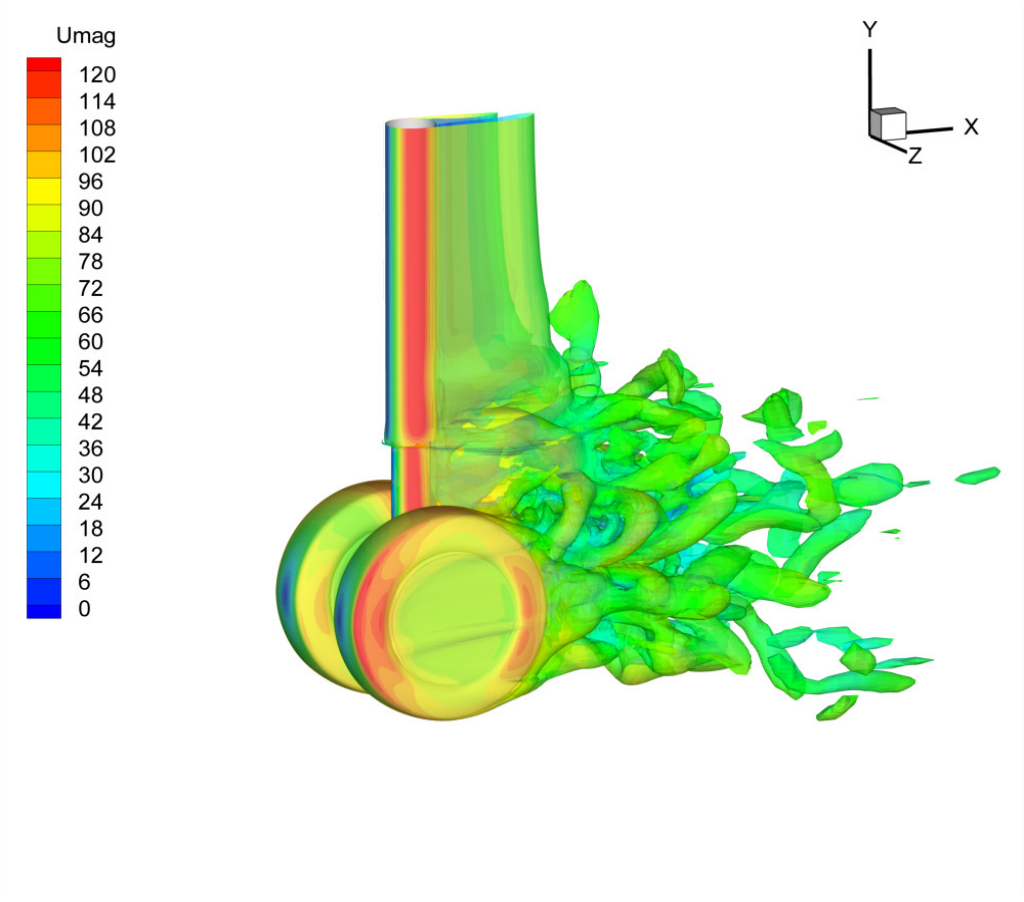

Figure 5.10: Three-dimensional iso-vorticity contour-surfaces colored by velocity magnitude.

Figure 5.11 shows an instantaneous plot of pressure coefficients and streamlines on a horizontal plane bisecting the axle and on the landing gear surface. Similar to the

findings in Chapter 4, the recirculation zone forming a large vortex inside the front area of the wheel cavity is observed to cause strong flow impingement onto the front surface of the axle. The flow separations and interactions after the impingement with unsteadiness in the vicinity may significantly contribute to the noise.

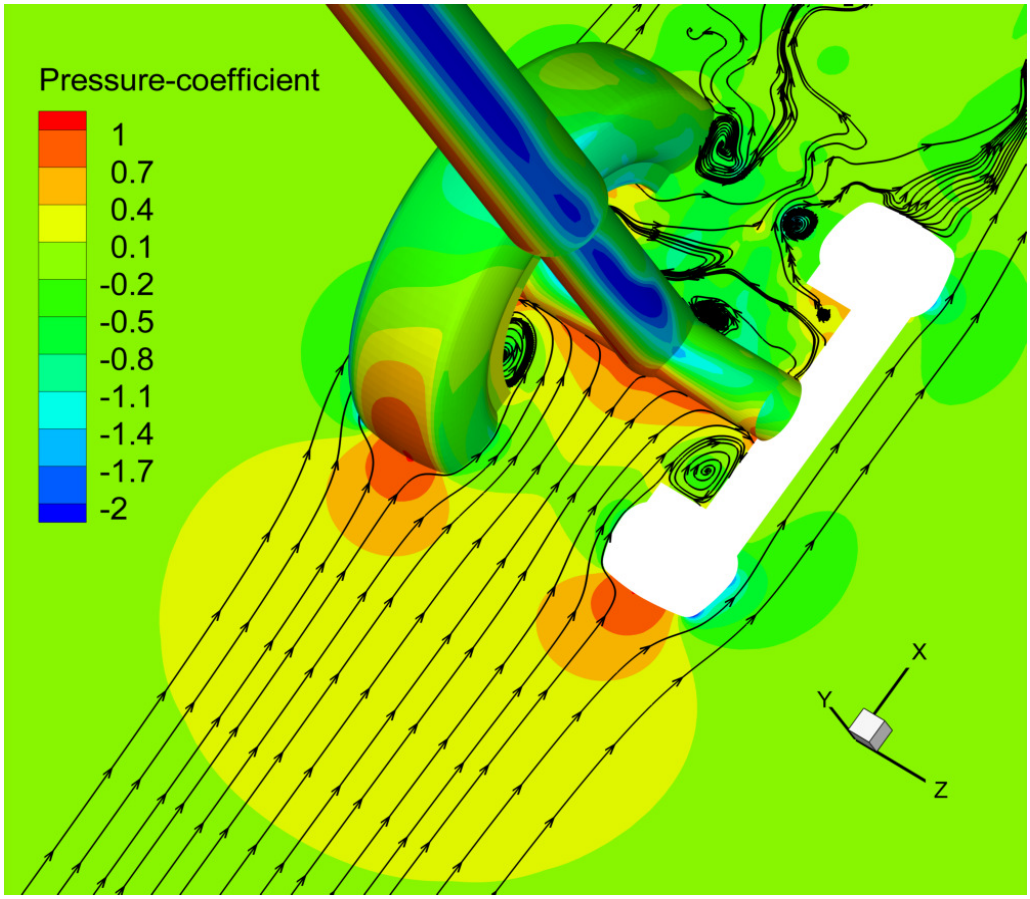

Figure 5.11: Contour plots of pressure coefficients with streamlines around the landing gear.

The levels of the unsteadiness of the flows are estimated by investigating the statistical measure of the flow velocity magnitude in the vicinity of the landing gear surfaces, shown by the root mean square of the velocity magnitude in Figs 5.12 and 5.13. The root mean square of the velocity magnitude is defined as

$$U_{RMS} = \sqrt{\frac{U_1^2 + U_2^2 + \cdots + U_n^2}{n}}, \tag{5.2}$$

where U is the velocity magnitude, and n is the sample number.

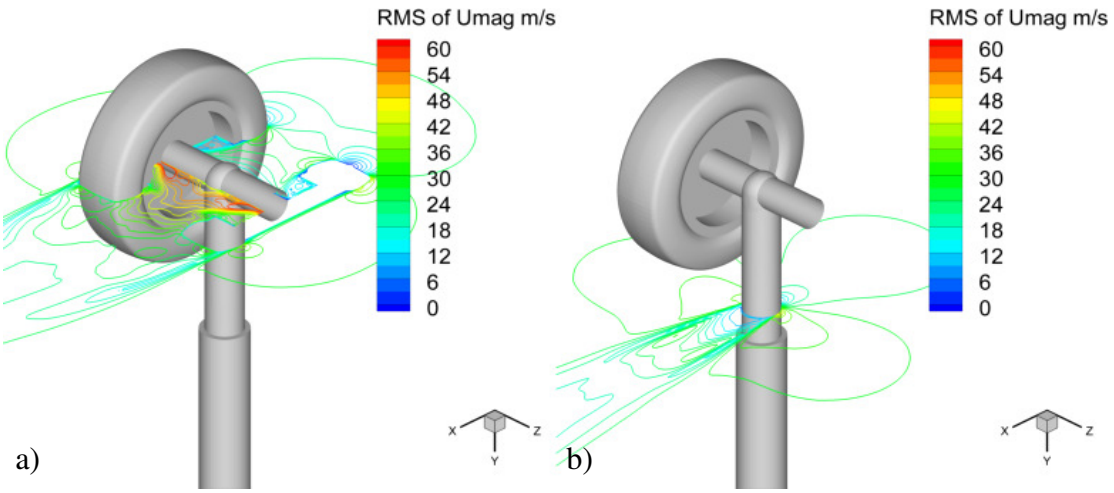

Figure 5.12: Contour plots of root mean square of the velocity magnitude on two horizontal planes: a) bisecting the axle and b) crosscutting the strut.

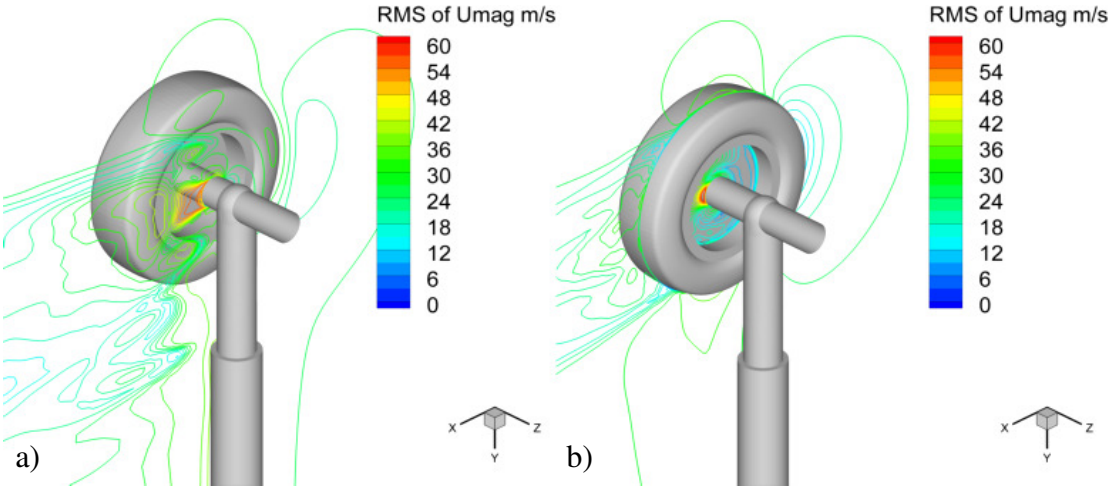

Figure 5.13: Contour plots of root mean square of the velocity magnitude on two vertical planes: a) crosscutting the axle and b) bisecting the left wheel.

The level of root mean square of the velocity magnitude is the highest in the vicinity of the impingement region mentioned in the above, which suggests that the axle may potentially be a major noise contributor to the landing gear noise. This is consistent with the findings in Chapter 4. A further investigation on acoustic field is followed in the next section.

5.3. Acoustic Results

The FW-H calculations are performed and the radiated sound is discussed in this section. The resulting sound spectra are produced based on 5 groups of 2048 samples of surface pressure data (6144 samples in total with 50% overlapping). Each data group is treated by the same Hann's window as used in Chapter 4 before FFT. The frequency bin width is 16 Hz. The results of the 5 data groups are then averaged to get a statistically converged spectrum.

5.3.1. Sampling Frequency Effect

As mentioned in section 5.1, the computations from FLUENT and SotonCAA have different time step sizes. This time step size difference therefore results in different sampling frequencies, which finally determine different frequency ranges resolved in the acoustic spectra. The acoustic signals are collected every step in FLUENT which has the sampling frequency of 33.3 kHz, and are collected every 100 steps from SotonCAA which has the sampling frequency of 11.4 kHz. In order to make a convictive comparison of the acoustic spectra with different sampling frequencies of each method, we have to evaluate the sampling effect on the final spectra. This effect is investigated by comparing the acoustic spectra from SotonCAA computations using two different sampling frequencies, 49.6 kHz vs. 11.4 kHz, shown in Fig. 5.14. We can notice that although the maximum resolvable frequency is increased by using higher sampling frequency, the major part of the PSD levels in the effective frequency range (which is more related to the numerical methods and grid density, refer to Fig. 4.21) are little affected. Therefore, the sampling frequency effect on the PSD levels is limited.

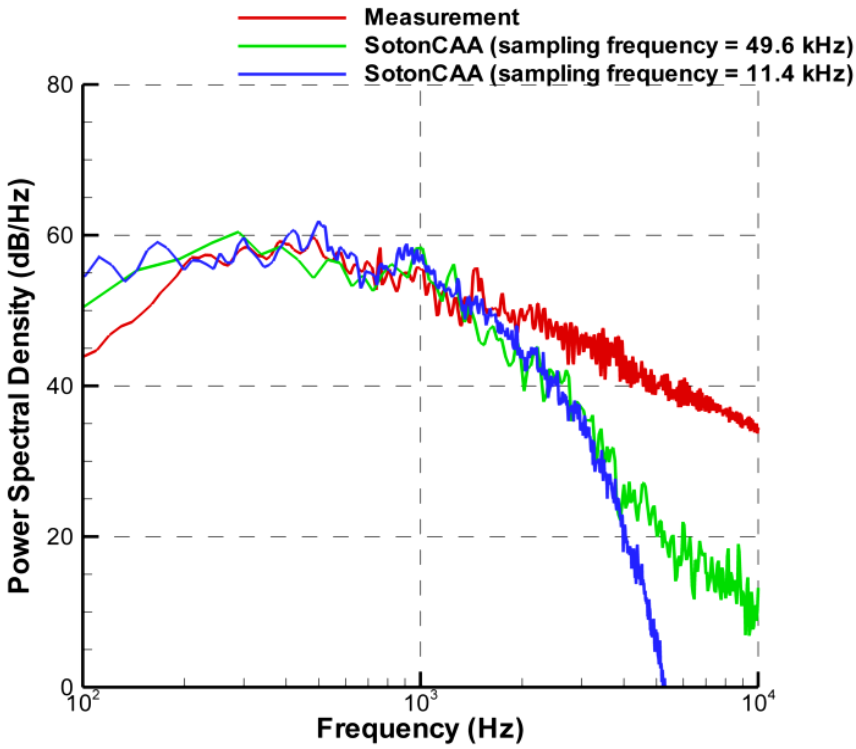

Figure 5.14: Sampling effect on the PSD levels.

5.3.2. Comparison with Experiment

Power spectral density (PSD) levels are compared among the measurement, FLUENT computation and SotonCAA computation in this section. Figures 5.15 and 5.16 compare the PSD levels between the computations and the measurement on the far field flyover microphone arc (shown in Fig. 4.19) and far field sideline microphone arc respectively. Both signals are collected at 140° of each arc in the azimuthal direction. The PSD predictions from FLUENT have the similar energy fall-off in the mid to high frequency range, which is consistent with the findings that the energy fall-off is caused by the grid density and numerical methods. Given the same grid, FLUENT predicts relatively lower PSD levels than SotonCAA does, in the effective frequency range up to 4 kHz. The under predictions are possibly due to the low-order discretization characteristics of FLUENT solver, since the sound related pressure fluctuations are small and sensitive to the discretizaton scheme accuracy.

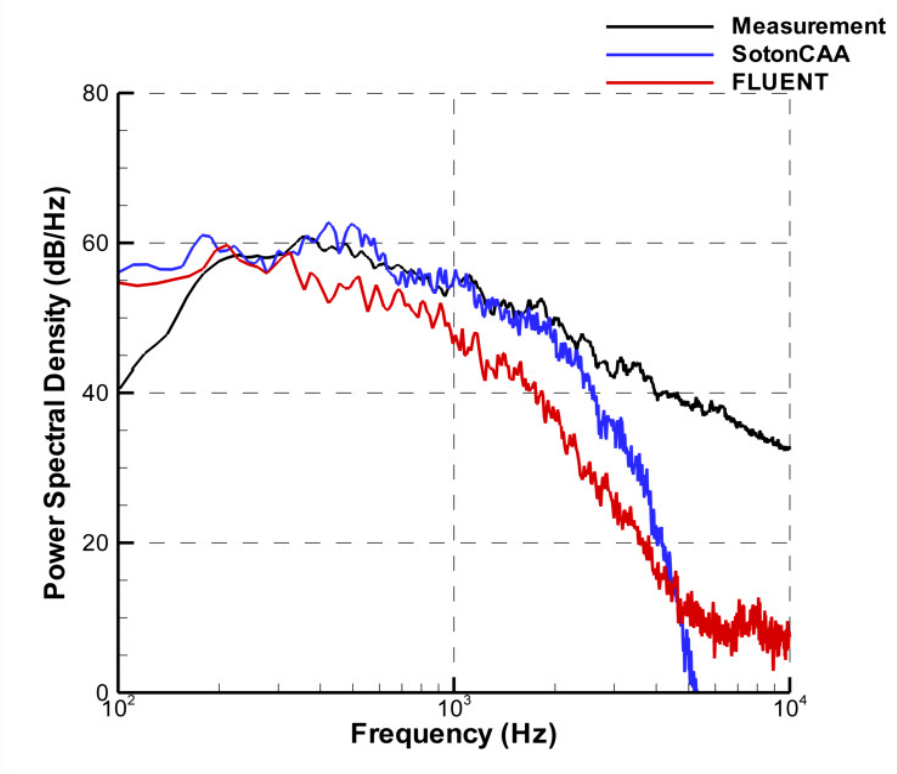

Figure 5.15: PSD comparison on the far field flyover microphone arc at 140°.

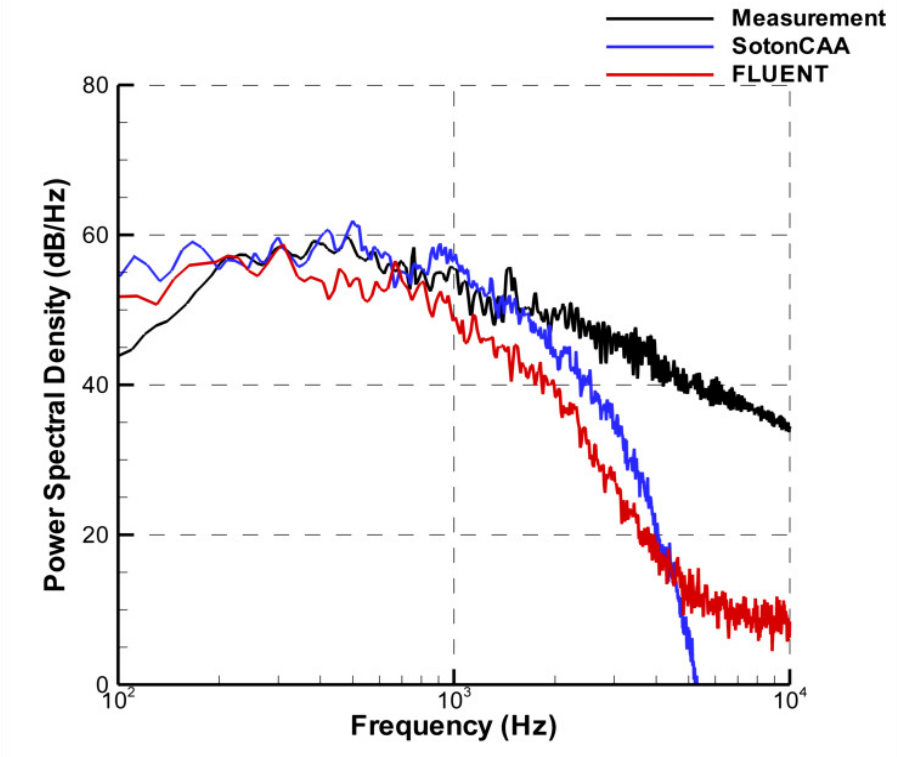

Figure 5.16: PSD comparison on the far field sideline microphone arc at 140°.

Figure 5.17 shows the comparisons of OASPL profiles obtained by the two computations and the reference measurement across a range of different microphone locations. It is clear that SotonCAA performed consistently better on all microphone locations. The OASPL prediction from the low-order schemed FLUENT has approximately 4 dB deviation with the measurement; while the high-order schemed SotonCAA has a better OASPL prediction with deviation less than 2 dB.

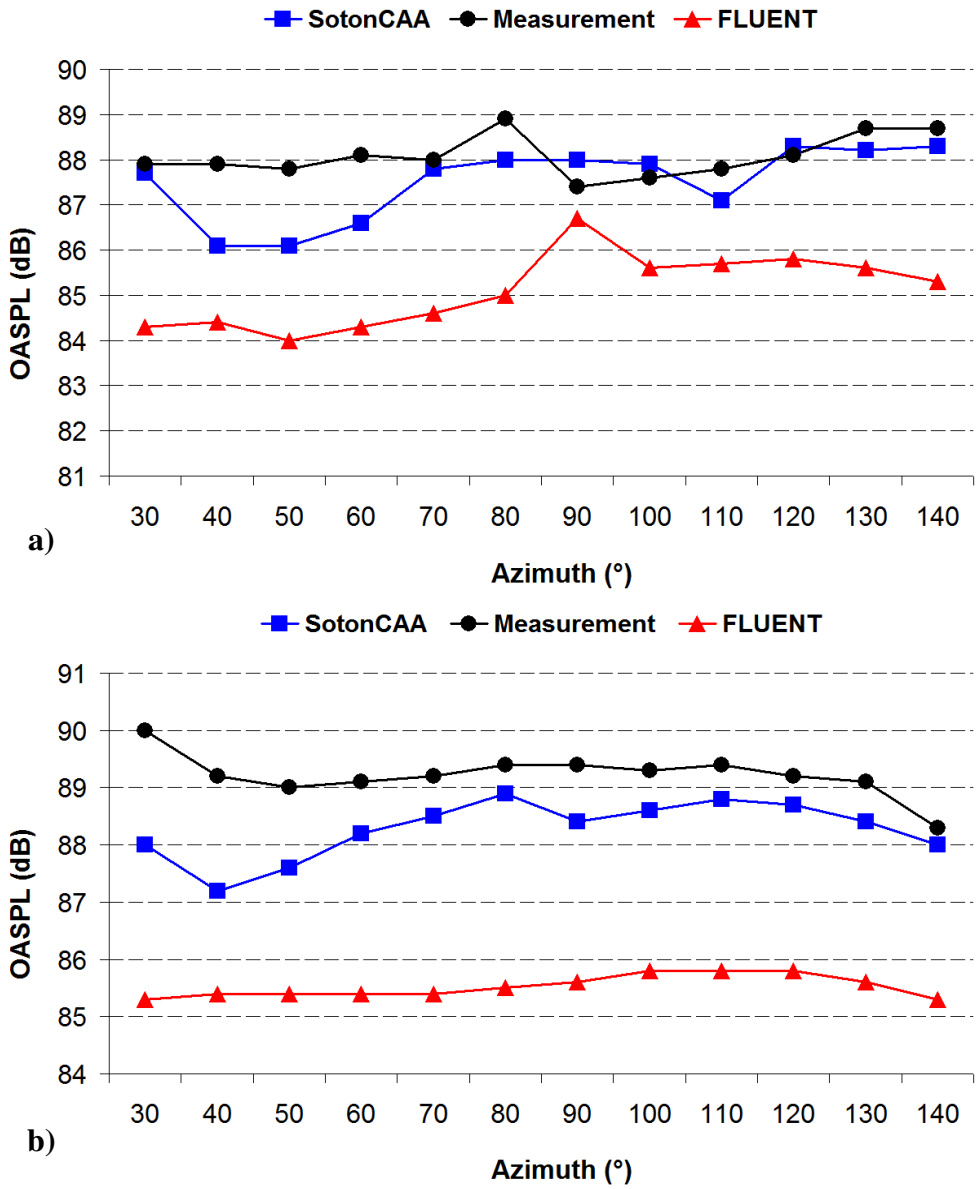

Figure 5.17: Far field OASPL comparisons on a) flyover and b) sideline microphone arcs.

5.3.3. Noise Sources Identification

The FW-H surface in FLUENT is decomposed in the same manner as shown in SotonCAA simulation to investigate component's contribution to the total noise. The surface divisions and observation positions are described in section 4.5.2. Figure 5.18 presents the contribution of each individual landing gear component to OASPL at various azimuthal locations indicated in Fig. 4.24.

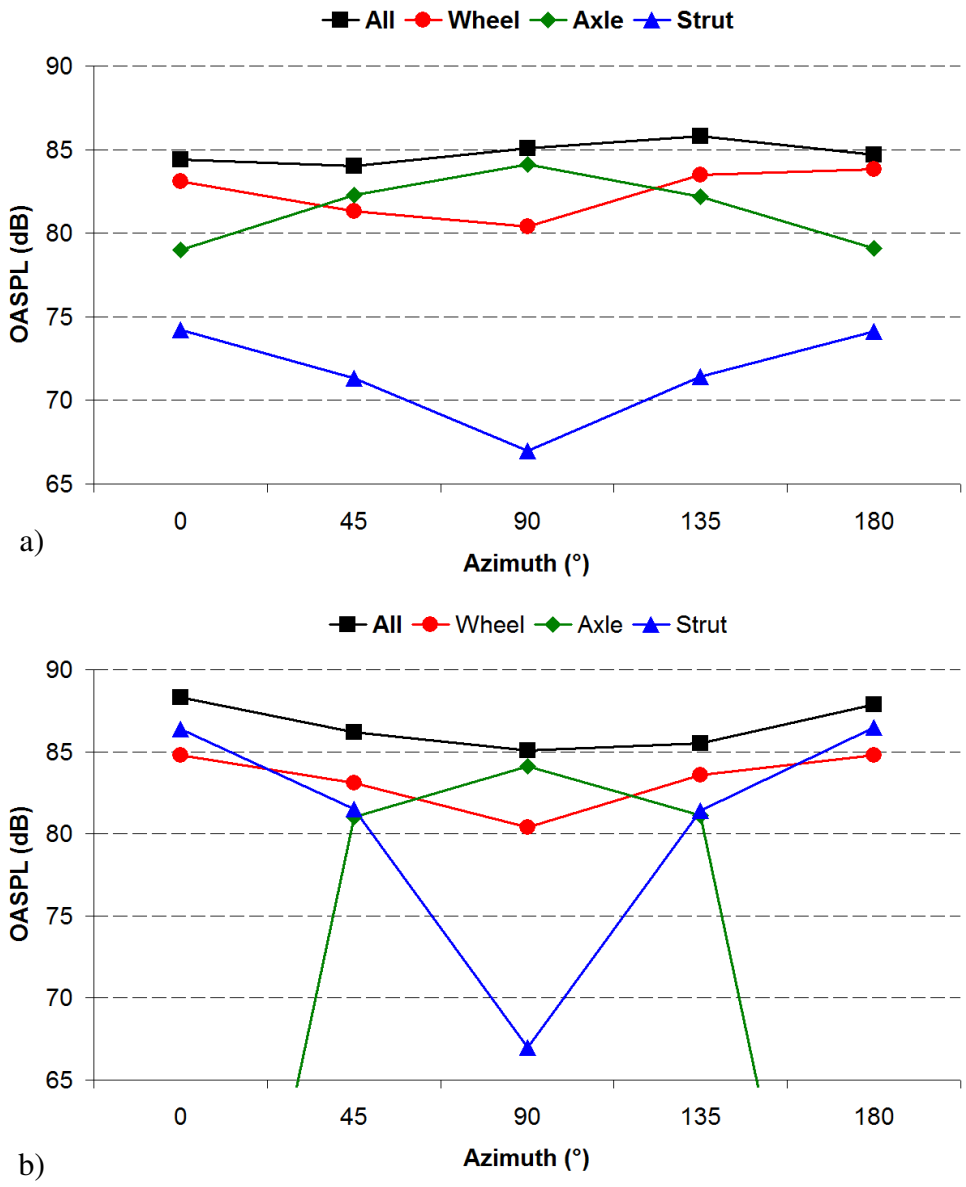

Figure 5.18: Noise contribution of each landing gear component in a) flyover and b) spanwise directions.

Similar to the findings in Chapter 4, the wheels are the primary noise sources in almost all directions. The axle is another major noise contribution in the flyover direction, especially in the overhead direction where the noise level is the highest among the three major components. The strut generally contributes weaker noise than other landing gear components in the flyover direction. The cylinder shape of the strut radiates relatively strong noise energy in the spanwise direction. The differences of noise directivity between FLUENT and SotonCAA computations are spotted at the wing sides in the spanwise direction, where the strut is the noisiest component of the landing gear from FLUENT; while the wheels are the dominant noise contributors from SotonCAA.

5.4. Summary

The comparison study of the landing gear noise prediction using FLUENT is presented in this chapter. The same baseline grid and flow conditions described in SotonCAA simulations are used in current simulation. The unsteady flow field is calculated by the FLUENT Navier-Stokes solver using second-order schemes. The time history of the unsteady surface pressure is collected to predict the far field noise with the FLUENT built-in FW-H solver. Both FLUENT and SotonCAA simulations obtain good agreements with the measurement on the time-averaged aerodynamic variables. The far field noise level predictions from SotonCAA are in good agreement with the measurement data with less than 2 dB deviation. However, the ability of FLUENT in predicting sound radiation is limited by the inherently low-order numerical discretizations, which under-predict the OASPL by approximately 4 dB. It is clearly shown that the CAA based method SotonCAA would be in preference to the conventional CFD method in predicting aerodynamic noise. By investigating the noise contribution from individual components, both computations agree that the wheels are the most significant noise sources, and the axle is another major noise source, around which the strong flow-body interaction noise is generated.

Chapter 6
Isolated Wheel Noise Prediction Using Low-order CFD

In this chapter, the noise radiation from an isolated wheel with high level of details is computed using the FLUENT package. This study was performed before the two-wheel landing gear simulations, not only to provide experience in applying hybrid method to predict the far field noise generated by complex geometries, but also to investigate the noise generation mechanism from the major component of landing gears. In section 6.1, the model geometry and grid generation are described. Computational setup is presented in section 6.2. The aerodynamic flow field and the acoustic results are discussed in sections 6.3 and 6.4 respectively, followed by the summary in section 6.5.

6.1. Model Description and Grid Generation

The simulated model is a scaled (1:3) isolated undercarriage wheel with detailed hub configuration. The wheel model has a diameter of 480 mm and a depth of 186 mm, depicted in Fig. 6.1.

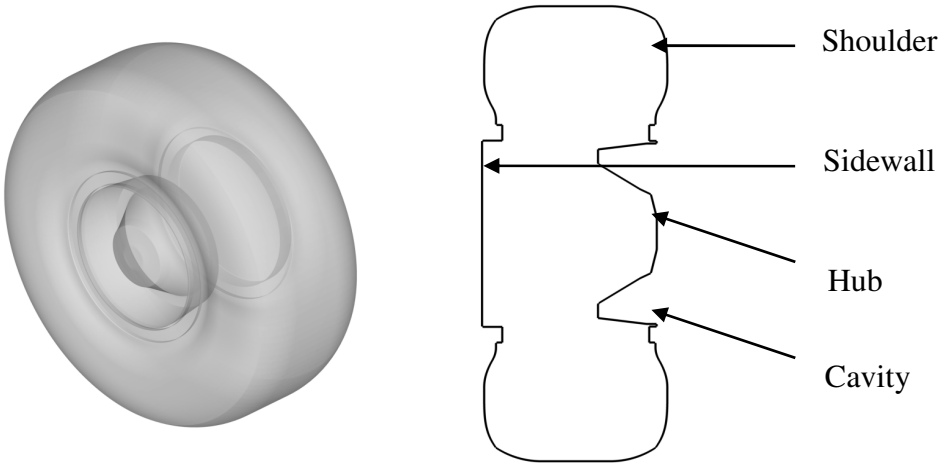

Figure 6.1: Drawings of the current isolated wheel model.

The entire single wheel model is surrounded by a multi-block structured grid, built in GRIDGEN [85]. A total number of 409 hexahedral blocks are generated to accommodate the wheel model in the centre of a domain of 13.5D, 9.6D and 6.8D in the streamwise, vertical and spanwise directions respectively, as shown in Fig. 6.2. The wheel diameter (D) is used as a reference length, and the flow is following the Z axis.

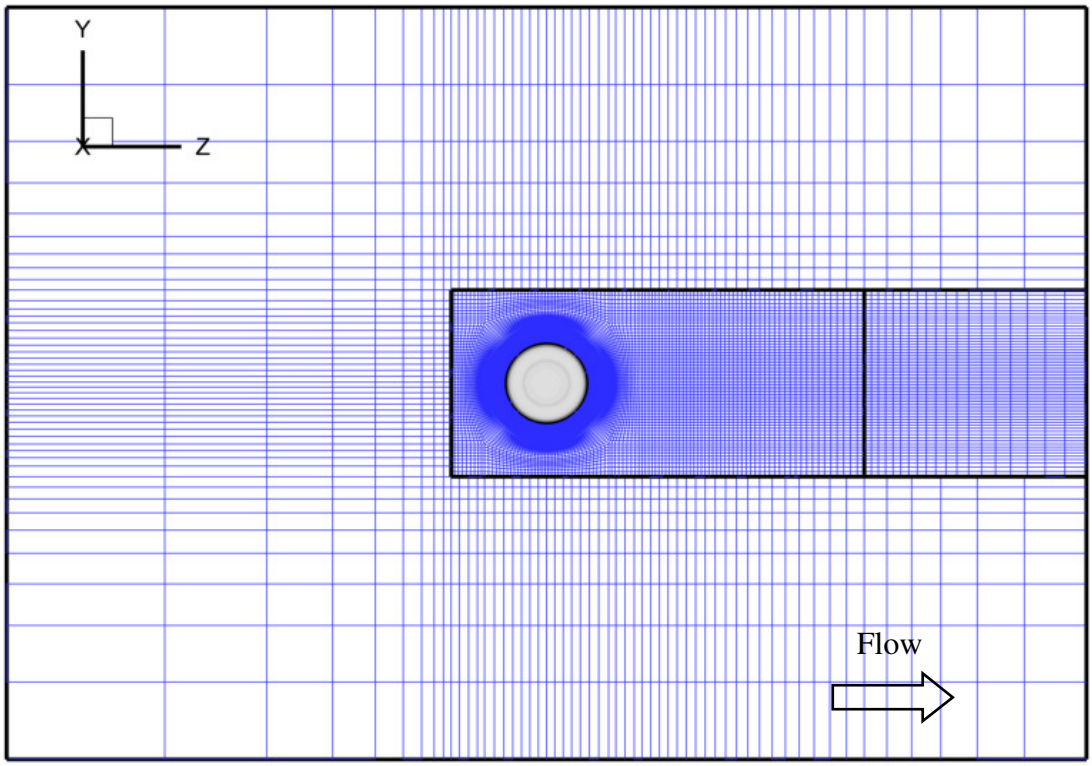

Figure 6.2: Schematic of the computational domain.

The grid is technically split into a near-wall RANS region and the outer LES region. Within the near-wall RANS region, the cells next to the wall surface have a thickness to wheel diameter ratio of 2×10^{-5} and are stretched on a growth ratio of 1.1. This wall-surrounding layer consists of 16 grid points normal to the surface and has very high cell aspect ratio. In the LES region, cubic cells are used in as much area as possible. The blocks that enclose the wheel surface have 160 cells distributed over the circumference. The patched mesh structure is adopted to reduce the total number of grid points. Fine grid blocks are built near the wheel surface and in the wake region of the wheel, while relatively coarse grid blocks are used to fill the rest of the computational

domain. The complete grid has approximately 3.9 million grid points. Figure 6.3 shows the surface meshes distributed over the solid wall of the wheel.

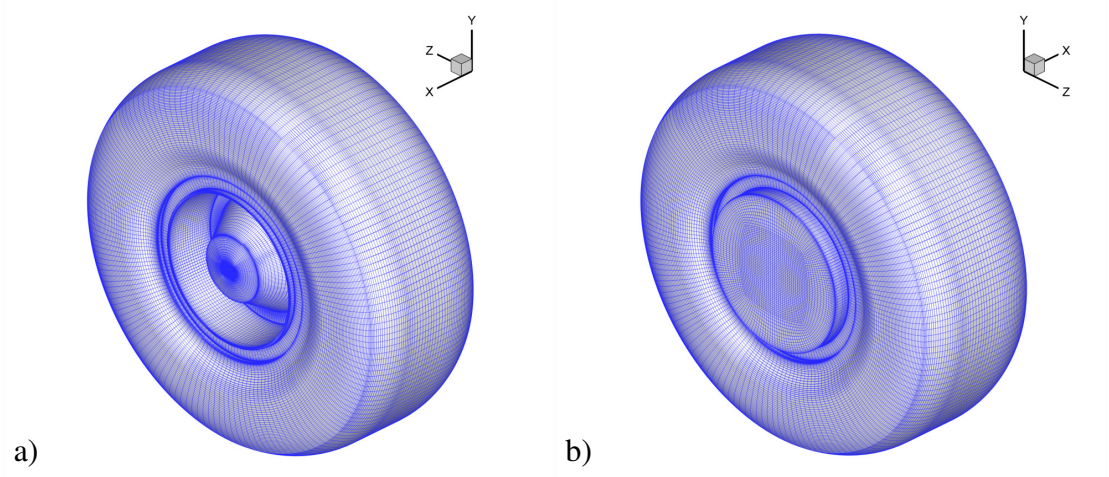

a) b)

Figure 6.3: Mesh distribution over the isolated wheel surface on a) hub-side and b) sidewall-side.

6.2. Computational Setup

The compressible Navier-stokes equations are solved by the three-dimensional, double precision, pressure-based unsteady solver in FLUENT (version 6.3.26) with second-order accurate schemes in space and time, see Table 6.1.

Table 6.1: Discretization schemes used in FLUENT.

Variable	Scheme
Pressure	Second order
Density	Second order upwind
Momentum	Second order upwind
Modified turbulent viscosity	Bounded central differencing
Energy	Second order upwind

The turbulence is simulated by using DES with S-A one equation model. The velocity inflow condition specifies the incoming flow speed and temperature at the inflow boundary, which are 85 m/s and 288 K respectively (It should be mentioned that there were no experimental data available when conducting this simulation. Therefore a typical aircraft landing speed was chosen in current study. Later experiments were

performed with lower incoming flow velocity up to 40m/s, which makes quantitative computation/measurement comparisons impossible.). The pressure far field boundary condition is used at the remaining boundaries of the computational domain. Current simulation is performed on the Spitfire cluster, utilizing a total of 16 processors. Initially, a steady-state computation is carried out to obtain a fully developed flow field and to investigate the grid quality for the turbulence model. As shown in Fig. 6.4, most parts of the wheel surface have considerably small y^+ value of below 3, and the highest level of y^+ value is less than 10.

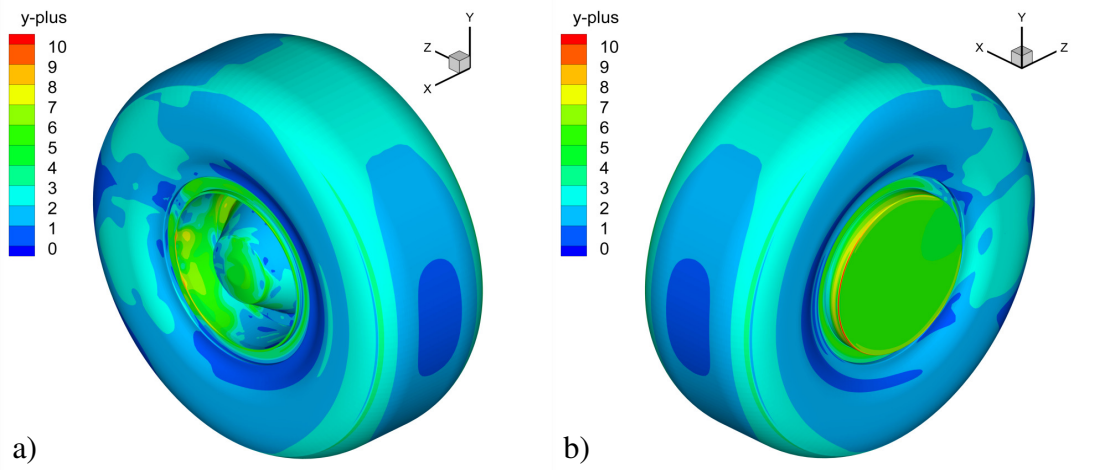

Figure 6.4: y^+ distributions over the isolated wheel surface on a) hub-side and b) sidewall-side.

The time-dependent unsteady computation is started with time step size of 3×10^{-5} second, with which a particle in the freestream would travel a distance of one wheel diameter in about 190 time steps.

6.3. Aerodynamic Results

6.3.1. Mean Flow Features

The aerodynamic forces on the isolated landing gear wheel are monitored during the simulation. The aerodynamic coefficients are determined by the dimensionless forces using the dynamic pressure $1/2\rho U^2$ and a reference area A, where U denotes the free-stream flow velocity and A is the product of the wheel diameter and the wheel depth,

which corresponds to the wheel projection area in streamwise direction. Figures 6.5 and 6.6 show the time history of drag and lift forces during a computing period of 0.207 second. The time-averaged drag and lift coefficients are 0.239 and 0.097 respectively. It is an interesting finding that positive lift force is generated from this isolated wheel surface, the geometry of which is symmetric in the lift direction.

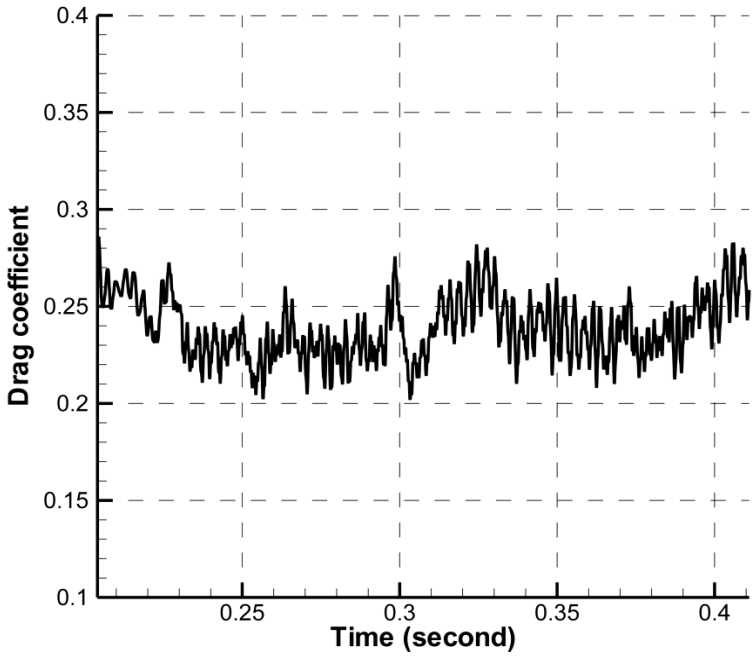

Figure 6.5: History of the drag coefficient.

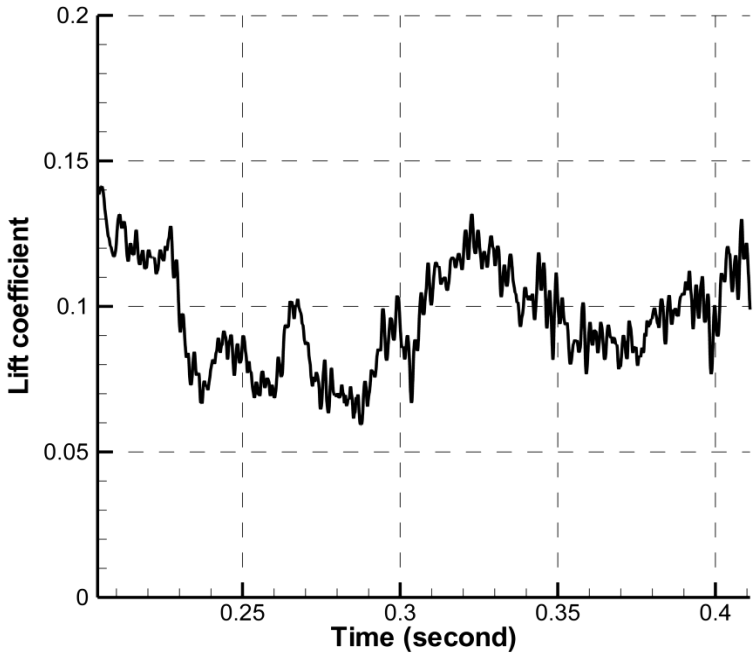

Figure 6.6: History of the lift coefficient.

Figure 6.7 shows the mean vertical velocity field on the median wheel plane. The asymmetry of the velocity field in the wake region is apparent, where the separated flow from the wheel upper shoulder has a larger recirculation zone than that from the lower shoulder. The corresponding asymmetric pressure distributions on the rear surface of the wheel, that pressure from the lower surface is higher than that from the upper surface, consequently contribute to upward lift force, shown in Fig. 6.8.

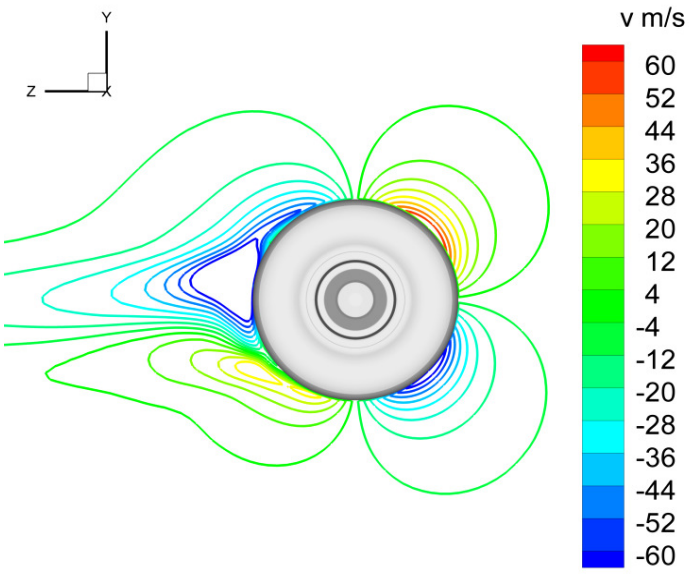

Figure 6.7: Mean vertical velocity field on the median wheel plane.

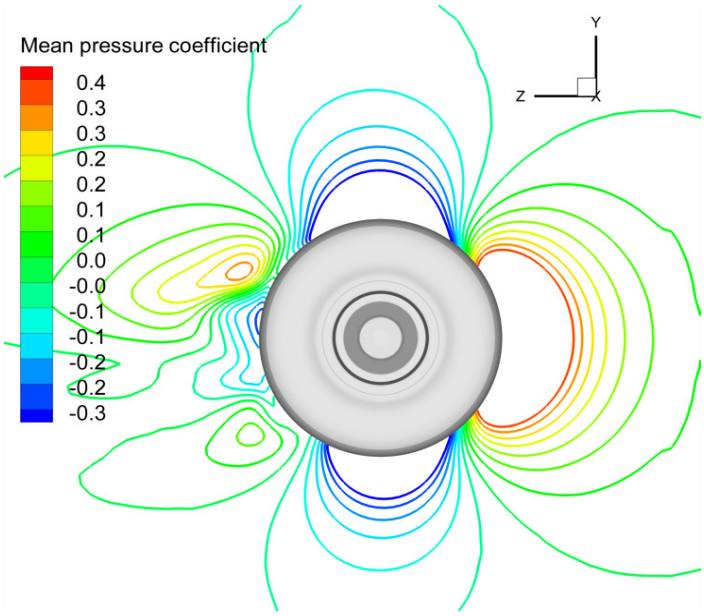

Figure 6.8: Mean pressure distributions on the median wheel plane.

The mean flow streamlines on the median wheel plane are plotted in Fig 6.9, and compared with the PIV measurement performed in the 2.1 m×1.7 m wind tunnel at University of Southampton [8], of which setup is demonstrated in Fig. 6.10.

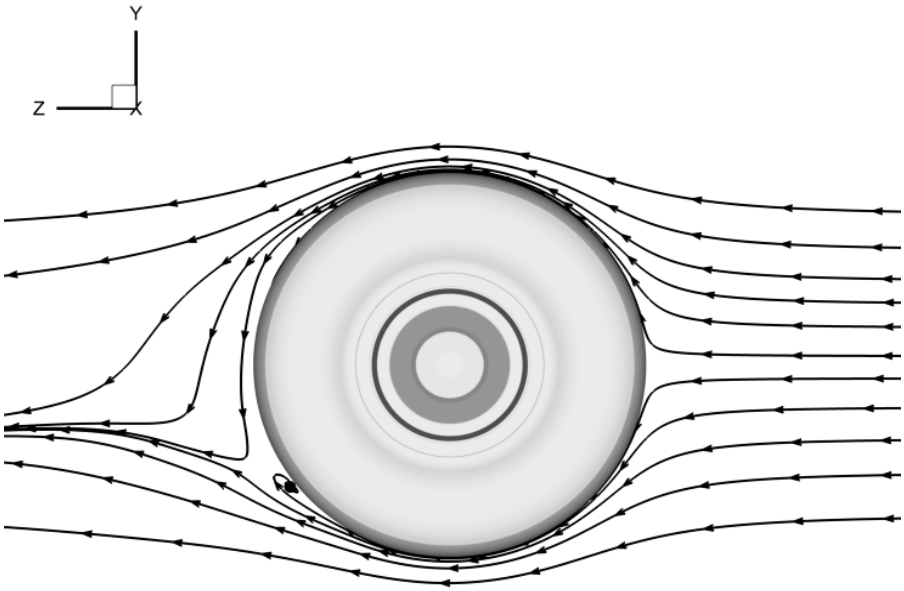

Figure 6.9: Mean flow streamlines on the median wheel plane.

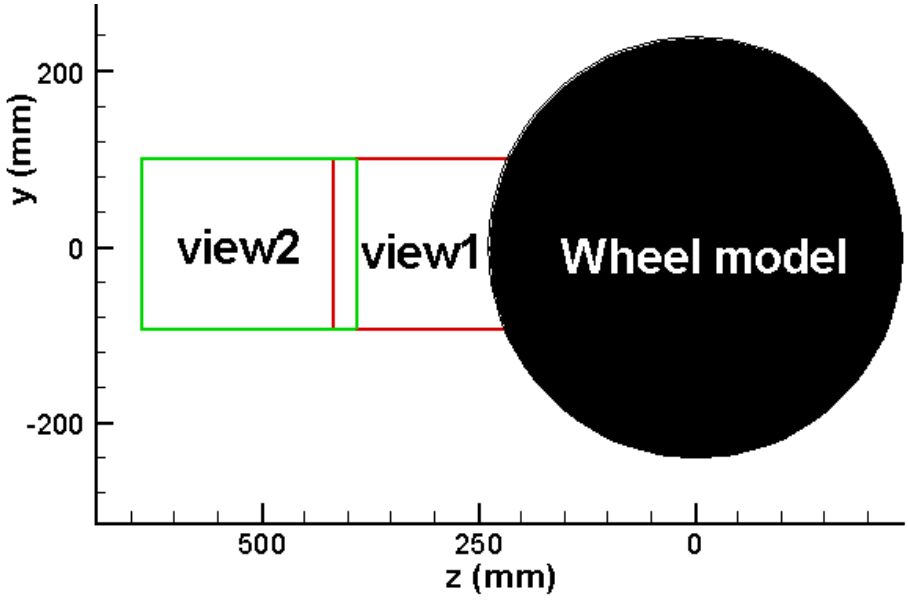

Figure 6.10: A schematic of the PIV setup.

Figure 6.11 and 6.12 show the PIV measurement results at two different flow speeds, 20 m/s and 40 m/s respectively. Good agreements of the asymmetry of the mean flow in the wake region have been obtained between the computation and the measurement. The distance, which the flow reattachment shifts from the wheel centerline, is relative to the flow speed: the higher the flow speed is the longer distance

the flow reattachment shifts. The mechanism of the flow asymmetry would be investigated in the next section.

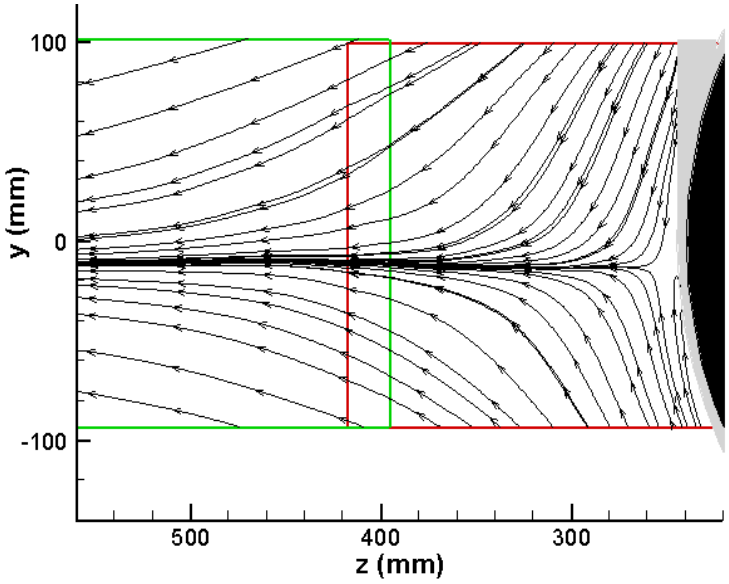

Figure 6.11: PIV mean flow streamlines in the wake region of the wheel at 20m/s.

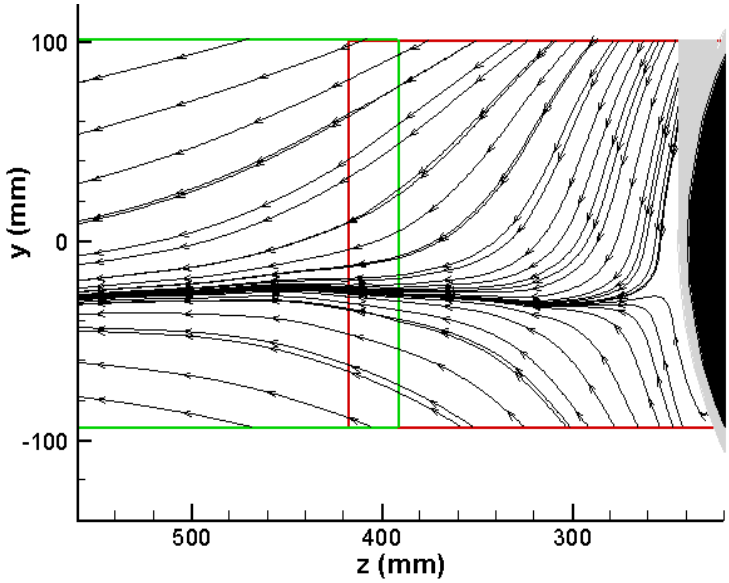

Figure 6.12: PIV mean flow streamlines in the wake region of the wheel at 40m/s.

6.3.2. Instantaneous Flow Field

The instantaneous pressure coefficients contours over the isolated wheel surface are shown in Fig. 6.13, viewed from different sides. The high level pressure at the front of

wheel surface represents the stagnation area of the flow. High pressure levels can also be spotted around the cavity-boundary and sidewall, which could be caused by the strong flow-body interactions in the downstream. The low pressure area at the edge of the wheel front shoulder indicates where the flow separations occur.

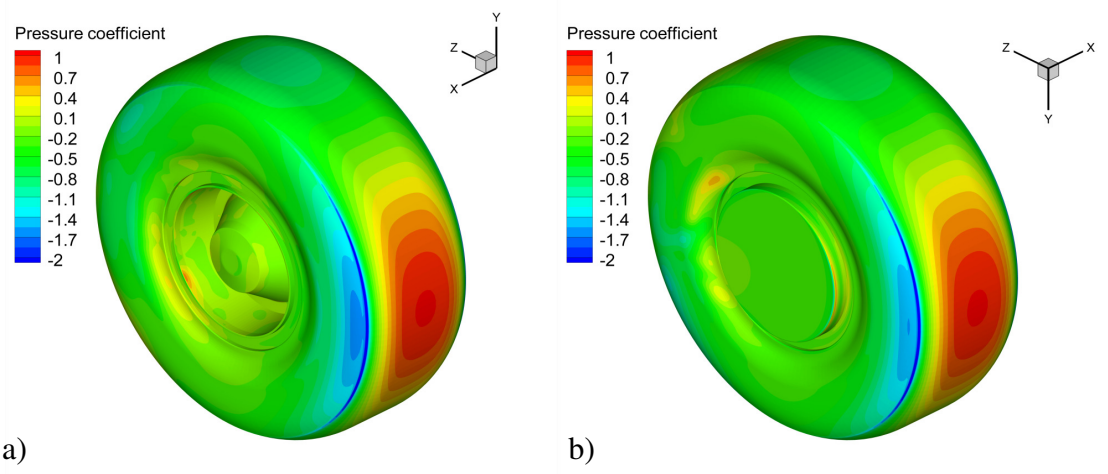

Figure 6.13: Instantaneous pressure coefficient contours on a) hub-side and b) sidewall-side.

The geometrical asymmetry of the wheel in the spanwise direction has generated highly turbulent flow with a lot of small vortex features. Figure 6.14 visualizes these vortex structures on the horizontal plane bisecting the wheel. On the hub-side, the separated flow from the front shoulder is obstructed by the extruded edge of the wheel inner cavity, where a small portion of the flows circulate in the small gap between the front shoulder and the edge, and the rest of the flows carry on with slight diversion off the wheel surface. Large scales of vortices are formed in the cavity when the slowed flows pass by and interact with the hub surface. On the sidewall-side, the upstream flows impinge on the sidewall, and generate strong vortices in the gap between the front shoulder and the sidewall. The attached flows on the sidewall surface separate later at the sidewall edge and reattach the wheel rear shoulder with high flow speed. The separated flows on the sidewall-side therefore possess higher velocity than that from the hub-side, and tend to roll towards the hub-side in the spanwise direction, see Fig. 6.15.

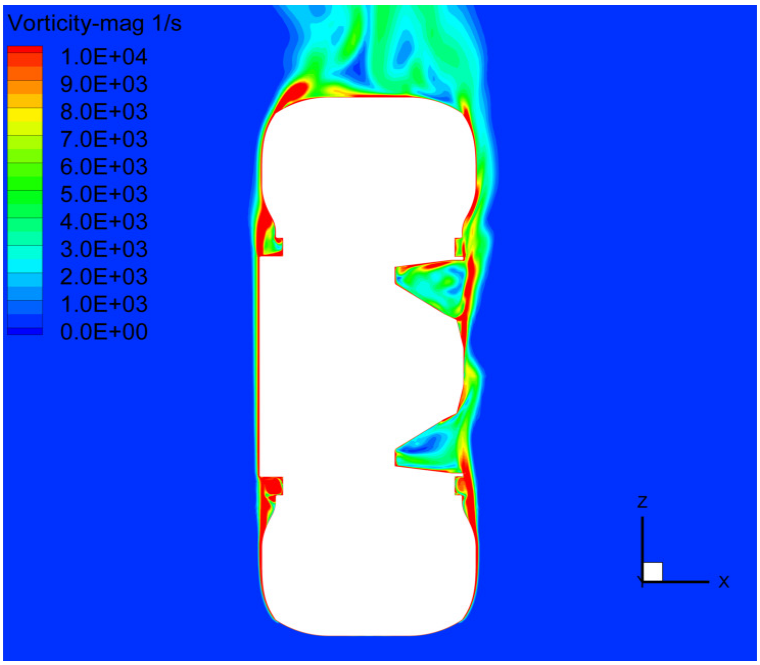

Figure 6.14: Vorticity contours on the horizontal plane bisecting the wheel.

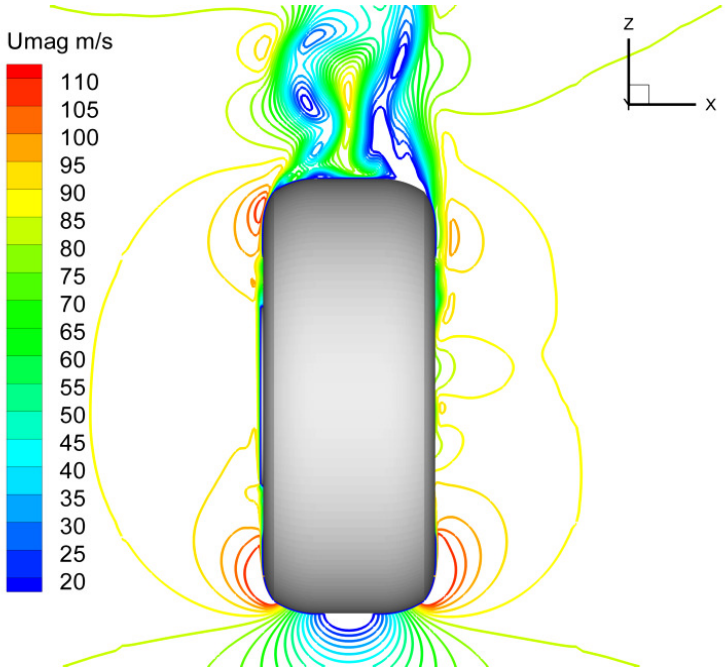

Figure 6.15: Contours of velocity magnitude on the horizontal plane bisecting the wheel.

Figure 6.16 visualizes the three-dimensional flow features using instantaneous iso-vorticity contours colored by velocity magnitude. It is clear that strong vortices originate from the hub-side of the wheel due to the flow-hub-cavity interactions. These vortices further interact in the wake leading to highly unsteady flow field. The asymmetric spanwise flow motions in the wake have complicated influence on the flow

features in the vertical direction, due to the three-dimensional characteristics of the turbulent flow, and therefore are possibly the reason that asymmetric flow features appear in the vertical direction.

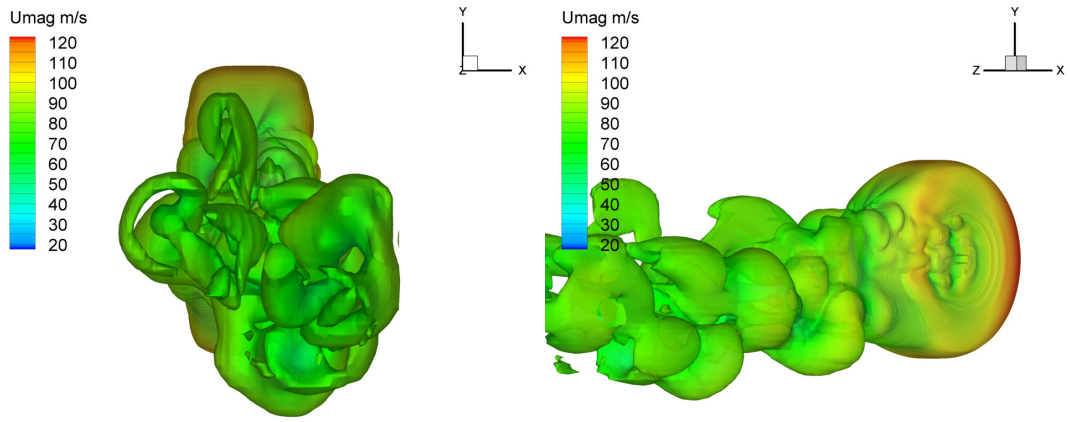

a) b)

Figure 6.16: Instantaneous iso-vorticity contours colored by velocity magnitude: a) rear view; b) side view.

6.4. Acoustic Investigations

6.4.1. Noise Sources Identification

For convenience of investigating the noise sources of the isolated landing gear wheel, a total number of 6 probes are positioned on the hub-side of the wheel to monitor the unsteady surface pressure, of which the positions are described in Fig. 6.17. Probe a, is placed on the front shoulder of the wheel, where initial flow separations may occur. Probes b and c are located on the upper and lower shoulders of the wheel, respectively. Probes d and e are on the hub and cavity-boundary respectively, where the flow interactions with solid surface may happen. Probe f is located on the rear shoulder, where upstream flows would reattach the wheel surface.

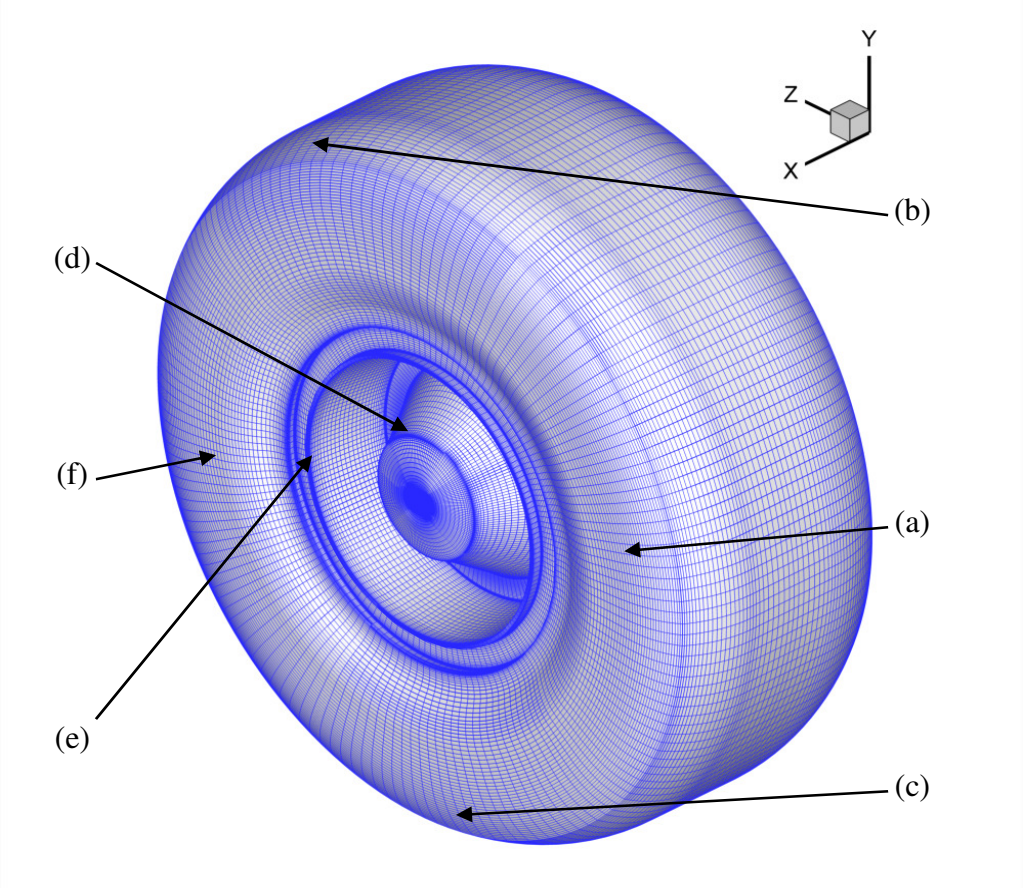

Figure 6.17: Monitor positions over the isolated landing gear wheel surface.

Figures 6.18-6.23 show the pressure fluctuations and corresponding frequency spectra at the monitor points. Although the unsteady fluctuation signal collected from each probe is generally broadband, several tonal peaks are still observable.

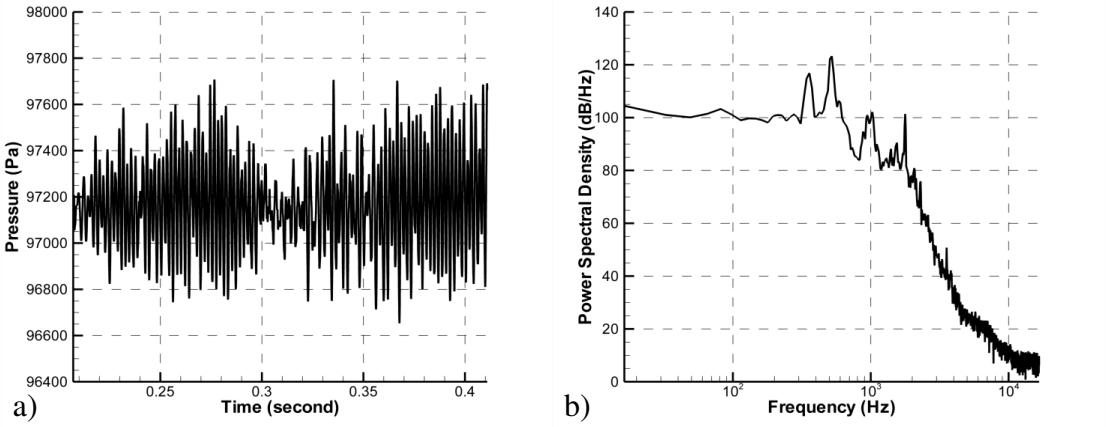

Figure 6.18: Plots of pressure fluctuation (a) and corresponding spectrum (b) at Probe a.

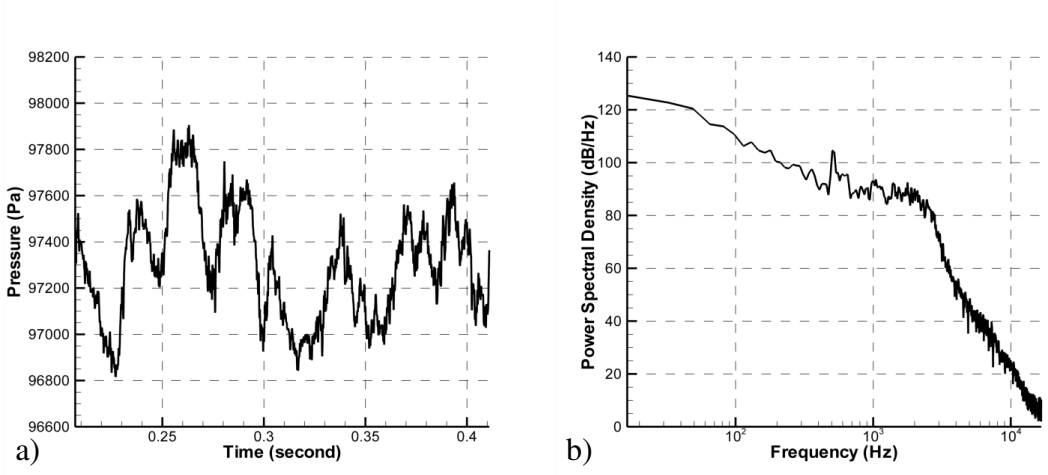

Figure 6.19: Plots of pressure fluctuation (a) and corresponding spectrum (b) at Probe b.

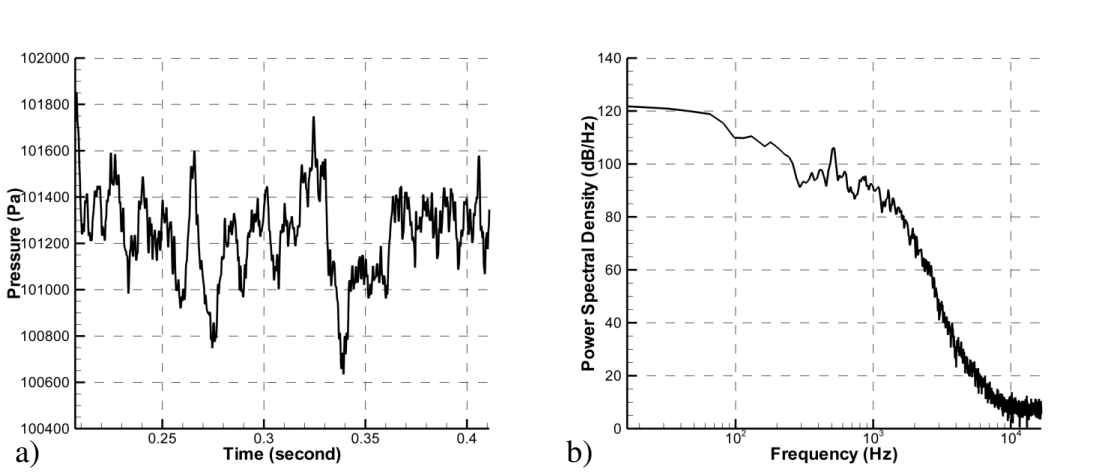

Figure 6.20: Plots of pressure fluctuation (a) and corresponding spectrum (b) at Probe c.

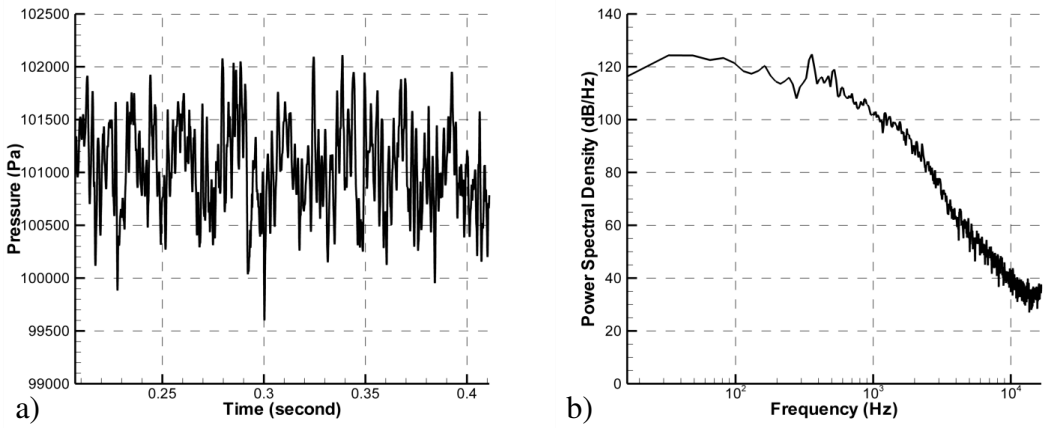

Figure 6.21: Plots of pressure fluctuation (a) and corresponding spectrum (b) at Probe d.

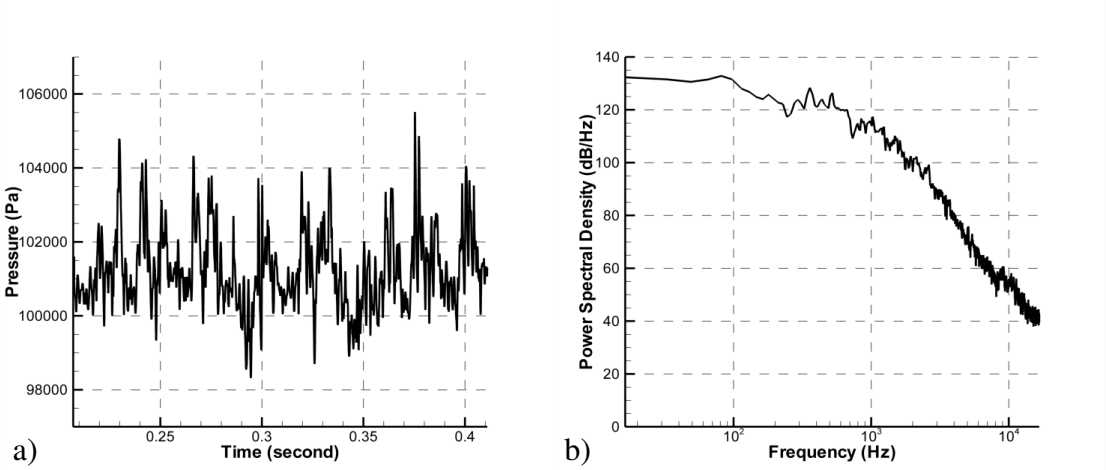

Figure 6.22: Plots of pressure fluctuation (a) and corresponding spectrum (b) at Probe e.

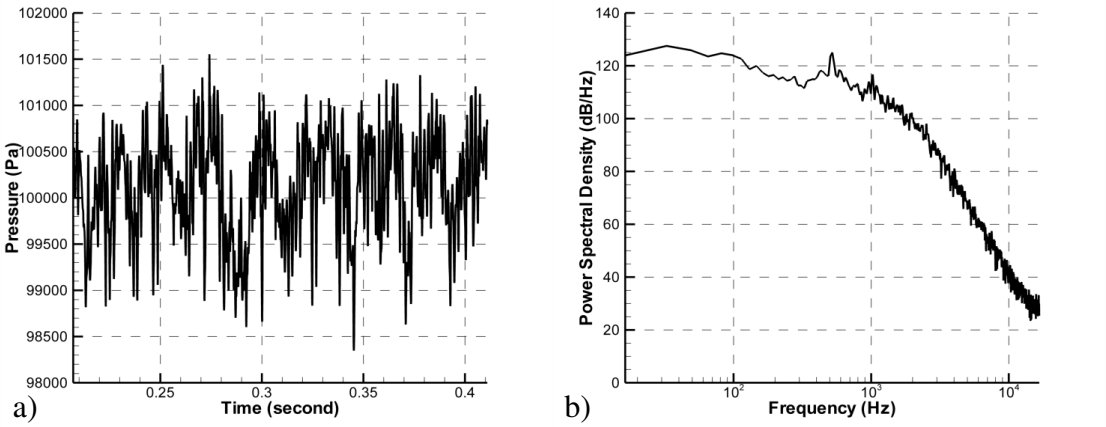

Figure 6.23: Plots of pressure fluctuation (a) and corresponding spectrum (b) at Probe f.

The frequency spectrum at the front shoulder of the wheel (Probe a) shows clear peaks at frequencies of 355 Hz, 522 Hz, 1020 Hz and 1780 Hz approximately, which are consistent with the peaks in the frequency spectrum of drag force, shown in Fig. 6.24. The other peaks at higher frequencies (multiples of the frequency of 1780 Hz) are believed to be numerical artifacts with resonance frequencies. The pressure fluctuations at upper and lower shoulders (Probe b and c) have similar frequency spectra with the same 522 Hz peak. The spectra at hub and cavity boundary (Probe d and e) suggest that the flow-hub-cavity interaction is associated with the tonal noise at 355 Hz and 522 Hz. The peaks at 522 Hz and 1020 Hz are dominant in the spectrum at the flow reattachment region on the rear shoulder. All the peak frequencies are associated with strong flow

alterations, such as flow separations and flow reattachment, which could be the potential tonal noise sources.

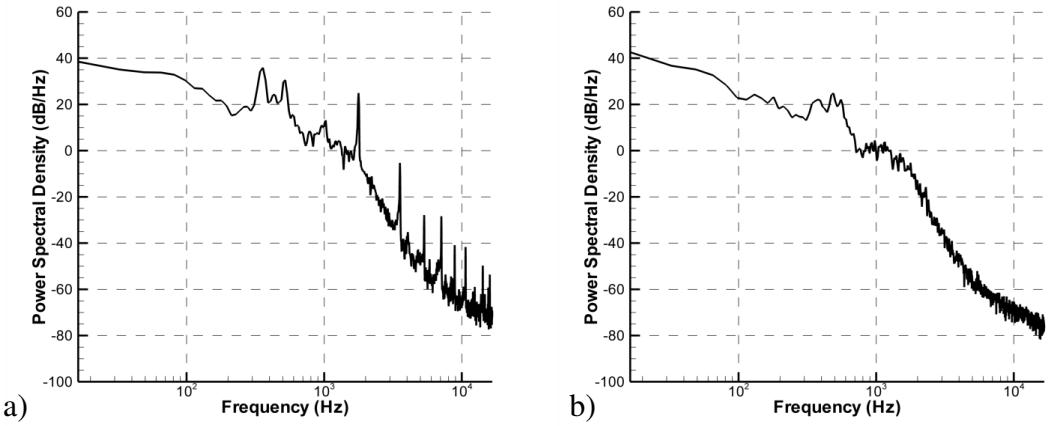

Figure 6.24: The frequency spectra of aerodynamic forces: a) drag; b) lift.

6.4.2. Far Field Noise

The FW-H integration surface is placed on the solid wheel surface to predict the far field noise. The resulting sound spectra are produced based on 5 groups of 2048 samples of surface pressure data (6144 samples in total with 50% overlapping). Each data group is treated by the Hann's window before FFT. The frequency bin width is 16 Hz. The results of the 5 data groups are then averaged to get a statistically converged spectrum. A total number of 72 receivers are evenly positioned around a circle of radius 100 m on the vertical plane (cutting the free-stream), depicted in Fig. 6.25.

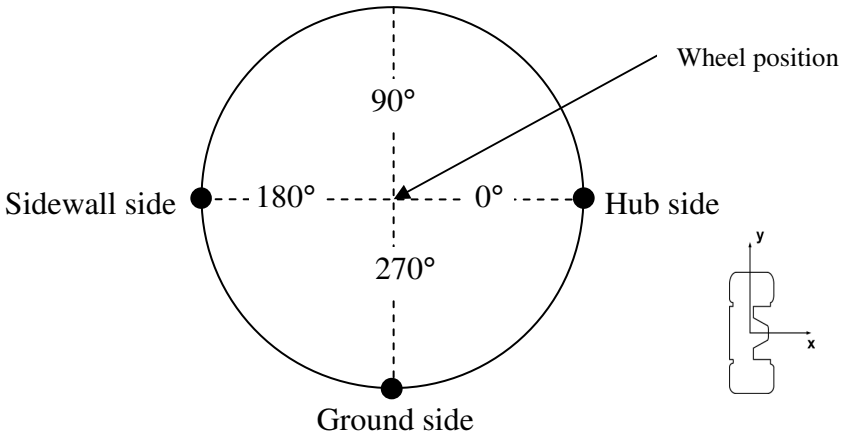

Figure 6.25: Drawings of the far field receiver positions.

Figure 6.26 shows the noise radiations from the isolated wheel, in terms of sound pressure level (SPL), towards the hub side, ground side and side-wall side respectively. Strong tonal noises are observable at 355 Hz, 522 Hz, and 1780 Hz, the frequencies of which are highly relative to the aerodynamic forces especially the drag force. 1780 Hz seems to be the most significant component in the spanwise direction. The agreement with the peak frequency recorded in the pressure fluctuations at the front shoulder suggests that this 1780 Hz tonal noise is possibly related to the vortex shedding of the separated flows off the front shoulder of the wheel. 522 Hz is the dominant frequency as the noise radiates towards the ground, and is the second significant peak in the hub side spectrum. Consistent with the peak frequency in the pressure fluctuations at the hub and cavity boundary, this 522 Hz frequency is believed to be highly related with the complex flow-hub-cavity interactions. The other peaks at higher frequencies (multiples of the frequency of 1780 Hz) are believed to be numerical artifacts with resonance frequencies. The directivity pattern is depicted in Fig. 6.27, showing that the isolated landing gear wheel radiates relatively stronger noise in the spanwise direction, due to the generally thin shape and the existence of detailed structures (hub-cavity and sidewall) in the spanwise direction.

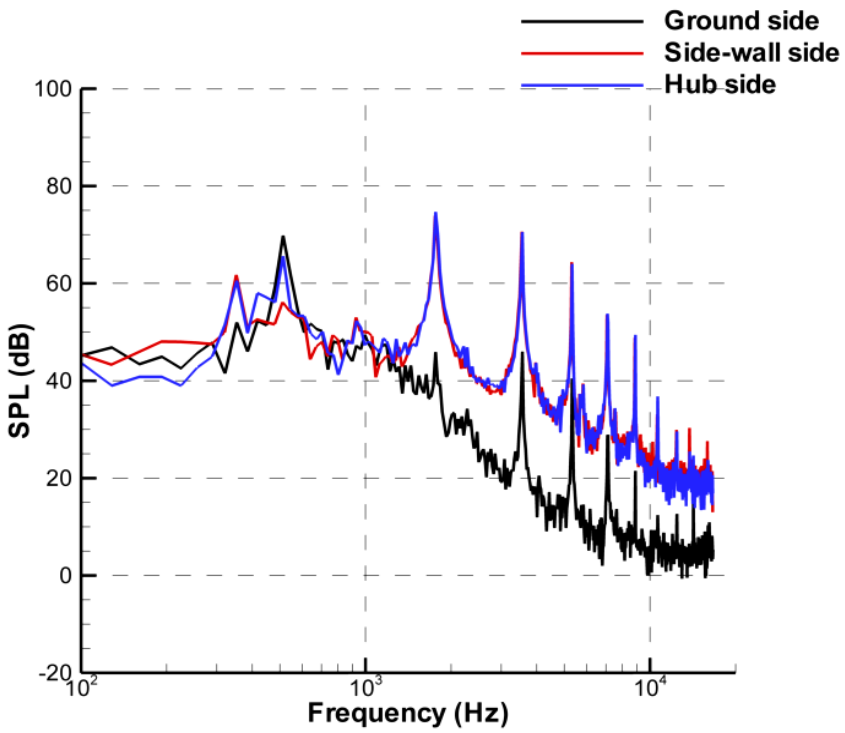

Figure 6.26: SPL spectra at far field locations.

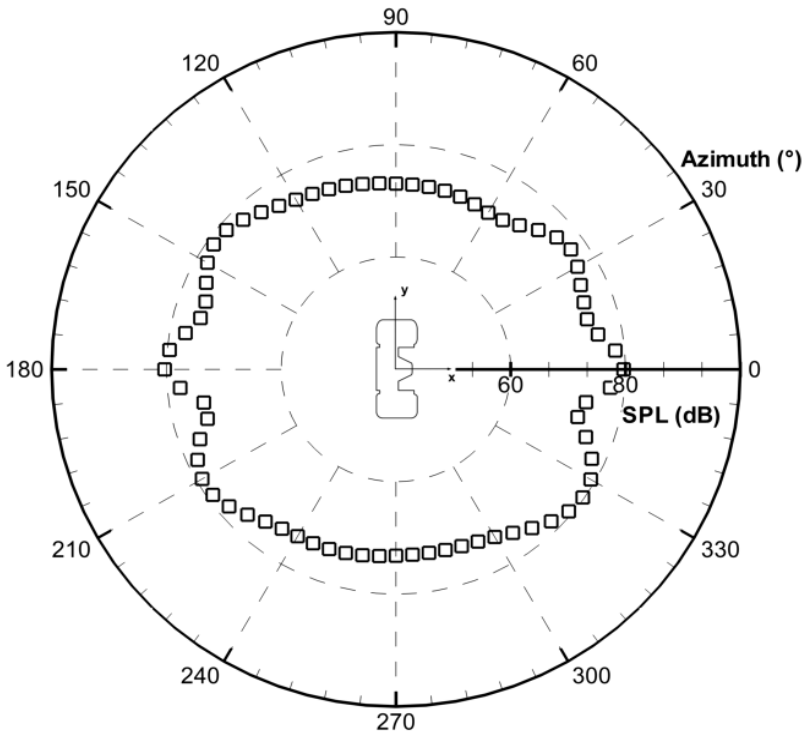

Figure 6.27: The directivity pattern of the far field noise from the isolated wheel.

6.5. Summary

The numerical study of the isolated wheel noise generation using FLUENT is presented in this chapter. The patched grid strategy is adopted in building the structured mesh for the 1:3 scaled isolated undercarriage wheel with detailed hub configuration. The hybrid approach is performed to predict the radiated far field noise from the wheel, combining the second-order Navier-Stokes solver which computes the unsteady flow in the near field and the FLUENT built-in FW-H solver which calculates the sound radiation in the far field. The mean flow asymmetry is realized in the wake region of the wheel, and is believed to be relative to the existence of the asymmetric hub configuration. The monitored near field pressure fluctuations and the far field noise predictions show that tonal noise is generated from the isolated wheel and is strongly associated with the aerodynamic forces. The vortex shedding off the wheel front shoulder is believed to be responsible for the tonal noise of 1780 Hz and the flow-body interactions within the hub configuration is likely to contribute the tonal noise of 522 Hz. The far field noise directivity pattern on the vertical plane suggests that the isolated wheel radiates

relatively stronger noise to the sides compared to the ground, which could be related to the thin wheel shape and the hub configuration.

Chapter 7
Conclusions

In this final chapter the main results of current work are summarized and suggestions for future studies are made.

7.1. Summary

The aim of current research is to assess the application of the SotonCAA code with high-order finite difference schemes to a 1:2.5 two-wheel generic A320 nose landing gear, and to investigate the generation and radiation of noise from such a complex geometry at the industrial level. The main achievements of this work are summarized below.

High-order finite difference CAA code has been successfully applied in the computations of noise prediction from highly complex landing gear geometries. Building a fully structured mesh which is required by the finite difference CAA code, over the complex landing gear architecture, has proved to the first challenge of current research. The complete mesh consists of 1604 hexahedral blocks, which was built up manually from segments and surfaces. The grid distributions and stretching ratios are optimized in each block to satisfy the DES requirement for the grids, which prefers cubic cells in the LES region. The CAA methods are normally attempted with uniform grids of simple geometries, and highly sensitive with curvilinear grids of complex geometries. Therefore, the second challenge is how to maintain numerical stability when applying high-order CAA methods to highly complex geometries. Multi-block structured meshes make the CAA application even more challenging, because singularity problems occur at the mesh-size-change interfaces. The characteristics-based multi-block interface treatment was implemented in the code, and successfully avoids the discontinuity problems associated with the high-order finite difference schemes. Artificial damping technique as well as explicit filtering method was also implemented to remove the numerical errors caused by non-uniform grids, and to stabilize the

numerical algorithms in the long-run computations. An interim interpolation code was developed to cast the unsteady flow quantities onto a three-dimensional user defined integration surface with arbitrary shape, so that the extracted flow data coupled with integration surface coordinate information could be directly imported to the FW-H solver for the far field noise calculations.

The high-order CAA application to the realistic landing gear geometry has achieved reliable aeroacoustic solutions up to 4 kHz, employing relatively cheaper structured grid compared to most large unstructured mesh (tens of millions cells) of similar geometries. Both aerodynamic and acoustic results compare well with the existing wind tunnel measurement data. Narrow band acoustic PSD spectra are well predicted in a frequency range up to 4 kHz for this particular landing gear model. The grid refinement study suggested that the energy fall-off in high frequency was grid density related and could be improved by finer mesh. The far field overall sound pressure levels are in good agreement between prediction and the measurement with 2 dB deviation. By investigating the noise contribution from individual components, we find that the landing gear wheels are the major noise sources in general. The axle is the second primary noise source, and contributes significant noise energy in overhead direction (2-3 dB higher than wheels), which is recognized to be associated with the strong flow-body interaction around the axle.

A comparison study using conventional CFD method Fluent is performed with the same landing gear model. Although conventional CFD can obtain good results on the time-averaged aerodynamic field, its ability of predicting sound radiation is limited by the inherent low-order numerical discretizations which under-predict the far field noise by approximately 4 dB. The conventional CFD method is still helpful in the noise source investigations, which has a good agreement with the high-order CAA method on the noise source identifications.

The isolated wheel computation is also performed using FLUENT to investigate the noise generation mechanism from the major part of the landing gear. The asymmetric phenomenon in the mean flow realized in the wake region of the wheel, is believed to be relevant to the asymmetry of the wheel geometry in the spanwise direction. Because of the thin shape and the detailed geometry, the isolated wheel radiates relatively higher sound energy to the sides than that to the ground, with several strong tonal noises associated with strong flow alterations. The vortex shedding off the wheel front shoulder is believed to be responsible for the tonal noise of 1780 Hz and the

flow-body interactions within the hub configuration is likely to contribute the tonal noise of 522 Hz.

7.2. Suggestions for Future Work

The high-order SotonCAA code is highly sensitive to the grid quality, especially with high level of geometrical complexity. Therefore, the artificial dissipation and filtering schemes and low-order wall boundary treatments must be used to maintain the numerical stability of the algorithms, which possibly induces strong numerical dissipation in the highly complex flow regions. It would be desirable to design and examine a stable high-order no-slip wall boundary condition for current high-order schemes. The filtering schemes should be improved especially at the block boundaries with less dissipation errors. Patched grid technique would also be desirable, not only to make the mesh construction easier for complex geometry, but also to effectively reduce the number of unnecessary grid points in the computational domain.

The comparison in term of methodology (Finite Difference/ Finite Volume) and schemes orders (2/4) has been studied in current research based on the same grid (multi-block structured). It is interesting to investigate the effect of mesh methodology (structured/unstructured) on the same numerical method. The straightforward way is to conduct FLUENT (Finite Volume) computations with both fully structured grid and fully unstructured grid of approximately the same resolution, and compare their performances on the landing gear computation.

The phenomenon discovered in the isolated wheel simulation, which the mean flow asymmetry in the spanwise direction causes the mean flow asymmetry in the vertical direction, might be further investigated using a more generic model, such as a circular cylinder with a cavity. Both numerical and experimental studies would be expected to investigate the mean flow features in the wake region.

Appendix A
Characteristic Interface Boundary Condition

In this appendix, the characteristic interface boundary condition [104] implemented in the SotonCAA Navier-Stokes equation solver is validated by the computation of the 2D Gaussian pulse propagation on the 3-blocks structured mesh where abrupt changes in the slope of grid lines happen at the interface.

A.1 Computational Setup

In this case, an acoustic pulse is generated by an initial Gaussian pressure distribution, and converted downstream with a freestream velocity. The computational domain consists of three quadrilateral blocks with 200×200 uniform grids of each block, shown in Fig. A.1. All the variables in the computation are nondimensionalized by the following scales: $L_{ref} = 1$, $U_{ref} = a_0$, $T_{ref} = 1/a_0$, and $P_{ref} = \rho_0 a_0^2$. When released at t =0, the Gaussian pulse is generated at (0, 0) by the pressure distribution

$$p = \varepsilon_1 e^{-\alpha_1 r^2}, \tag{A.1}$$

where ε_1=0.01 is the pressure pulse amplitude. The parameter α_1 is determined by the half width b of the Gaussian pulse by $\alpha_1 = \ln 2/b^2$, where b = 3.0 in this case. r denotes the distance between the observer and the source. The Gaussian pulse is propagated downstream with the velocity 0.5 (freestream Mach number) following the x axis. The numerical simulations employ the 6th-order Hixon scheme [30] in space discretizations and 4-6 LDDRK scheme [33] in the time integrations. The time step size is 0.05, which corresponds to the CFL number of about 0.14. Two interface boundary conditions are tested in this case: traditional interface boundary conditions employing explicit central schemes, and characteristic interface conditions with biased schemes. Their performances in the 3-blocks Gaussian pulse propagation computations are discussed in the next section.

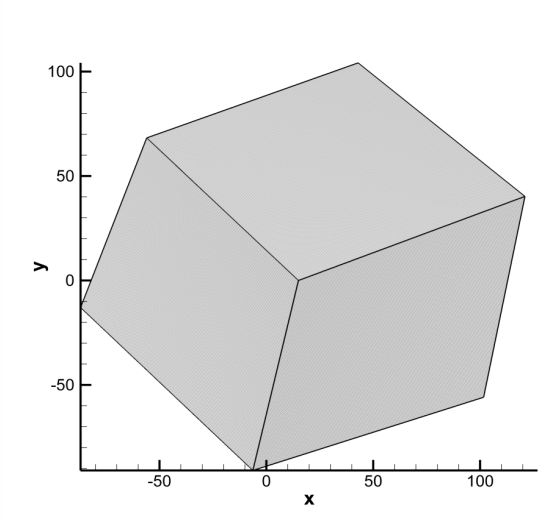

Figure A.1: The computational domain of the 2D Gaussian pulse propagation case.

A.2 Results and Discussions

Figure A.2 shows the initial pressure distribution of the Gaussian pulse at t = 0.

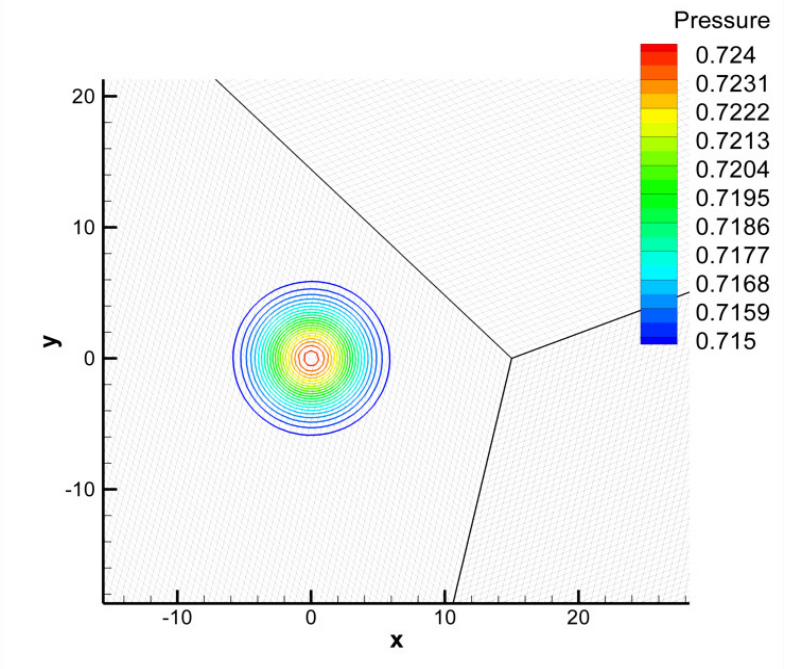

Figure A.2: The initial pressure contours of the Gaussian pulse at t = 0.

The abrupt changes in the slope of the grid lines at the block interface of the 3-blocks mesh, lead to the discontinuity of the grid matrices along the interface, which is known

as the singularity problem. In conventional interface conditions, the grid matrices at the singular points are often approximated to single values by averaging the left- and the right-hand limits, which certainly induces numerical errors. Figure A.3 depicts the Gaussian pulse propagation employing the conventional interface conditions, just before the occurrence of the computation blow-up. The computation blows up after 31 time steps, and the pressure field is contaminated by the numerical errors accumulated along the singular grid interface.

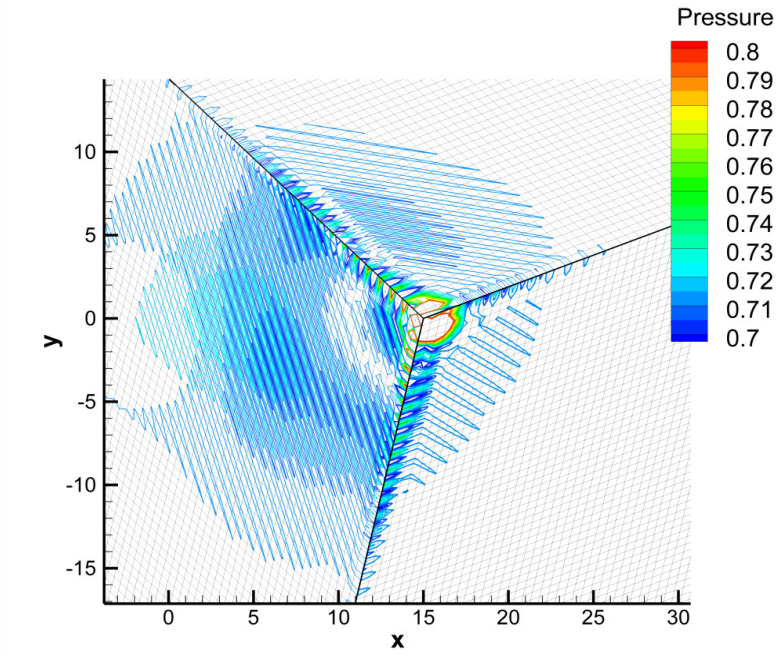

Figure A.3: A demonstration of the singular problem using conventional interface conditions.

The grid singularity can be successfully avoided by employing the characteristic interface boundary conditions. Figures A.4 and A.5 show the Gaussian pulse propagation after 300 and 900 time steps. We can see that the wave front of the Gaussian pulse expands radically with the freestream convection speed 0.5, and passes the grid interface lines smoothly.

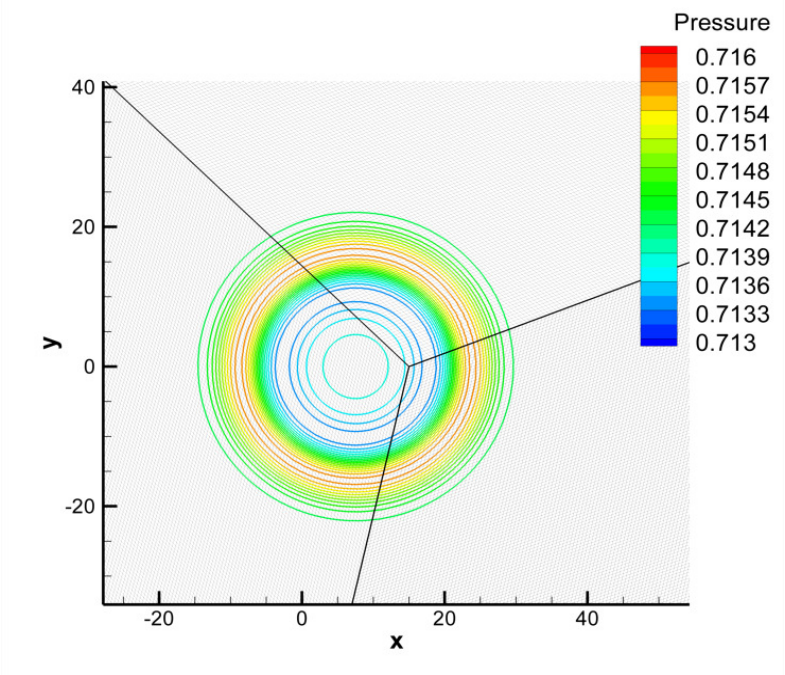

Figure A.4: The pressure contours of Gaussian pulse after 300 time steps.

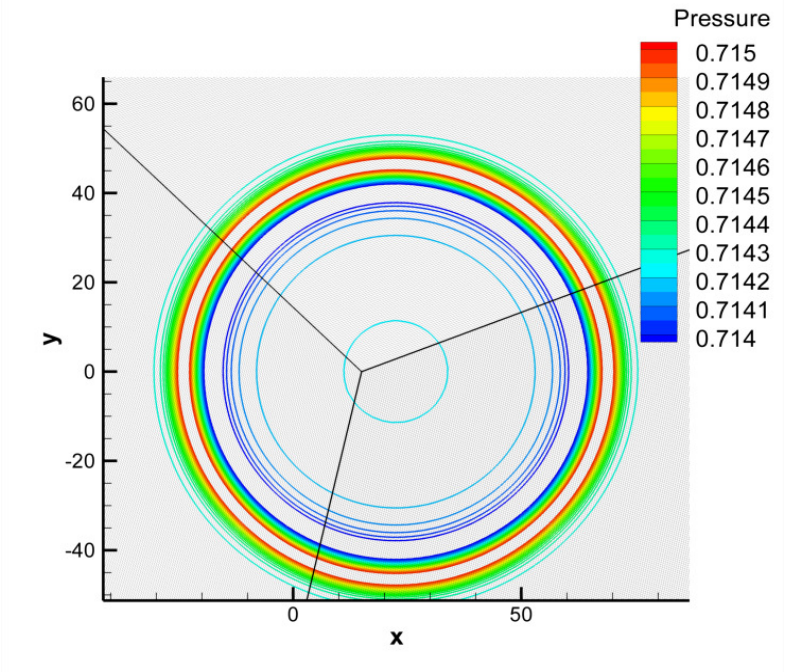

Figure A.5: The pressure contours of Gaussian pulse after 900 time steps.

The pressure distribution in the Gaussian pulse propagation can be analytically calculated by solving the linearized Euler equations, and the solution is given by

$$p(x, y, t) = \frac{\varepsilon_1}{2\alpha_1} \int_0^\infty e^{-\xi^2/4\alpha_1} \cos(\xi \cdot t) J_0(\xi \cdot \eta) \xi d\xi \,, \qquad \text{(A.2)}$$

where $\eta = [(x - Mt)^2 + y^2]^{1/2}$, M is the freestream Mach number, and J_0 is the Bessel function of order one. Figure A.6 compares the pressure fluctuation ($p - p_{ref}$) between the numerical solution and the analytical solution at the observation point (15, 0). The excellent agreement between the numerical results and the exact solution confirms that the characteristic interface treatment is valid and performs well on complex multi-block structured grids with singular interfaces.

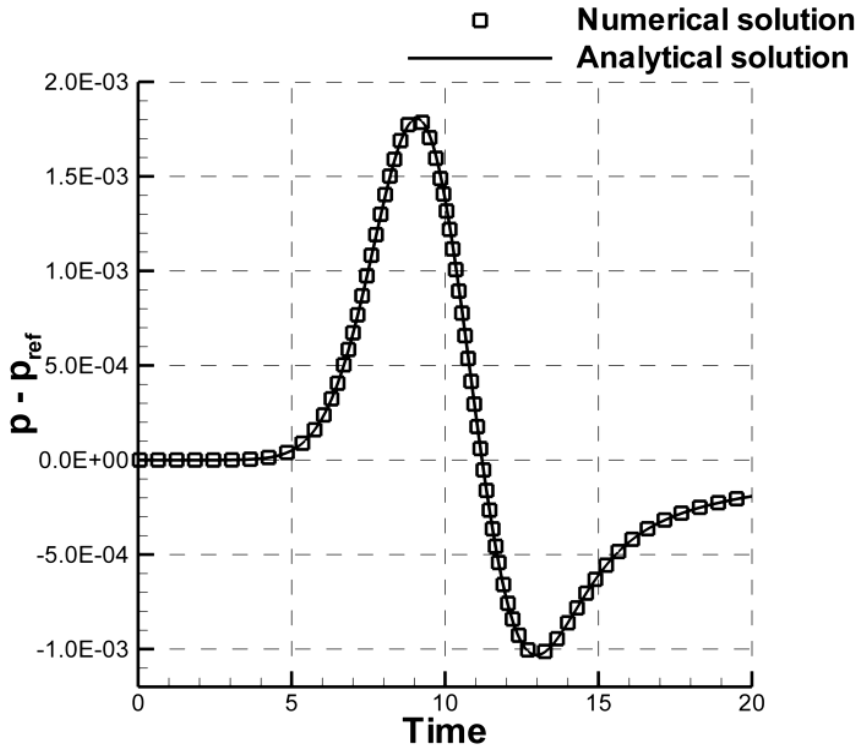

Figure A.6: Comparison of the pressure fluctuation at the observation point (15, 0).

Appendix B

Implementation of the Artificial Selective Damping Method

In this appendix, the source Fortran code of the artificial selective damping function in x-direction is provided.

```
C*****************************************************************
C Compute artificial dissipation in x-direction
C*****************************************************************
Subroutine dissipation_dx(blk, var)

      USE constants
      USE coefficients
        USE num_params
        USE grid_vars
        USE working_vars
        USE bc_vars
        USE dissipation_vars
        USE conserved_vars

        IMPLICIT NONE

        INTEGER (KIND=4)  :: blk, var
        REAL    (KIND=8)  :: lamda_max, lamda_min, lamda_hat_max, lamda_hat_min
        REAL    (KIND=8)  :: P_max, P_min, sigmma, alffa, betta, expo
        REAL    (KIND=8)  :: alffa_hat, betta_hat, niu_max
        REAL    (KIND=8)  :: slope_backward, slope_forward

C*****************************************************************
C extrapolate con_var out of boundary using 4th order standard scheme
C*****************************************************************

        Do k = kmin(blk), kmax(blk)
        Do j = jmin(blk), jmax(blk)

          slope_backward = 3/2*con_var(2,j,k)-3/10*con_var(3,j,k)+
     &                     1/30*con_var(4,j,k)-37/30*con_var(1,j,k)

          con_var(0,j,k) = con_var(1,j,k) - slope_backward
          con_var(-1,j,k)= con_var(1,j,k) - 2*slope_backward
```

```
          con_var(-2,j,k)= con_var(1,j,k) - 3*slope_backward

          slope_forward = 37/30*con_var(imax(blk),j,k)-
     &                             3/2*con_var(imax(blk)-1,j,k)+
     &                            3/10*con_var(imax(blk)-2,j,k)-
     &                            1/30*con_var(imax(blk)-3,j,k)

        con_var(imax(blk)+1,j,k)=con_var(imax(blk),j,k)+ slope_forward
        con_var(imax(blk)+2,j,k)=con_var(imax(blk),j,k)+ 2*slope_forward
          con_var(imax(blk)+3,j,k)=con_var(imax(blk),j,k)+ 3*slope_forward


      End do
      End do

C*********************************************************************
C     Calculate lamda and lamda_hat(lamda over metrics) at each point
C     in x direction
C*********************************************************************
      Do k = kmin(blk), kmax(blk)
        Do j = jmin(blk), jmax(blk)
        Do i = imin(blk), imax(blk)
         If (dims.eq.3) then
       lamda(i,j,k)=Dabs(U(blk)%at(i,j,k))+Dsqrt(gamma*P(blk)%at(i,j,k)/
     &              rho_temp(blk)%at(i,j,k)*
     &              (metrics(blk)%at(i,j,k,1)*metrics(blk)%at(i,j,k,1)+
     &               metrics(blk)%at(i,j,k,2)*metrics(blk)%at(i,j,k,2)+
     &               metrics(blk)%at(i,j,k,3)*metrics(blk)%at(i,j,k,3)))
        lamda_hat(i,j,k)=lamda(i,j,k)/
     &         Dsqrt(metrics(blk)%at(i,j,k,1)*metrics(blk)%at(i,j,k,1)+
     &               metrics(blk)%at(i,j,k,2)*metrics(blk)%at(i,j,k,2)+
     &               metrics(blk)%at(i,j,k,3)*metrics(blk)%at(i,j,k,3))
         Else
        lamda(i,j,k)=Dabs(U(blk)%at(i,j,k))+Dsqrt(gamma*P(blk)%at(i,j,k)/
     &              rho_temp(blk)%at(i,j,k)*
     &              (metrics(blk)%at(i,j,k,1)*metrics(blk)%at(i,j,k,1)+
     &               metrics(blk)%at(i,j,k,2)*metrics(blk)%at(i,j,k,2)))
        lamda_hat(i,j,k)=lamda(i,j,k)/
     &         Dsqrt(metrics(blk)%at(i,j,k,1)*metrics(blk)%at(i,j,k,1)+
     &               metrics(blk)%at(i,j,k,2)*metrics(blk)%at(i,j,k,2))
       End if
          End do
          End do
          End do


C*************************************************************
C     Calculate lamda stencil plus in x direction
C*************************************************************
      Do k = kmin(blk), kmax(blk)
```

```
        Do j = jmin(blk), jmax(blk)
C-----------------------------------------------------------------------
          Do i = 3, imax(blk)- 3
             lamda_max = 0.0d0
             lamda_min = 1.0d9
                Do m = -2, 3
                 If (lamda(i+m,j,k) .GE. lamda_max) lamda_max=lamda(i+m,j,k)
                 If (lamda(i+m,j,k) .LE. lamda_min) lamda_min=lamda(i+m,j,k)
                End do
             lamda_all_plus(i,j,k)=lamda_max-lamda_min
        End do
C-----------------------------------------------------------------------
        i = 1
         lamda_max = 0.0d0
         lamda_min = 1.0d9
           Do m = 0, 3
            If (lamda(i+m,j,k) .GE. lamda_max) lamda_max=lamda(i+m,j,k)
            If (lamda(i+m,j,k) .LE. lamda_min) lamda_min=lamda(i+m,j,k)
           End do
         lamda_all_plus(i,j,k)=lamda_max-lamda_min
C-----------------------------------------------------------------------
        i = 2
         lamda_max = 0.0d0
         lamda_min = 1.0d9
           Do m = -1, 3
            If (lamda(i+m,j,k) .GE. lamda_max) lamda_max=lamda(i+m,j,k)
            If (lamda(i+m,j,k) .LE. lamda_min) lamda_min=lamda(i+m,j,k)
           End do
         lamda_all_plus(i,j,k)=lamda_max-lamda_min
C-----------------------------------------------------------------------
        i = imax(blk) - 2
         lamda_max = 0.0d0
         lamda_min = 1.0d9
           Do m = -2, 2
            If (lamda(i+m,j,k) .GE. lamda_max) lamda_max=lamda(i+m,j,k)
            If (lamda(i+m,j,k) .LE. lamda_min) lamda_min=lamda(i+m,j,k)
           End do
         lamda_all_plus(i,j,k)=lamda_max-lamda_min
C-----------------------------------------------------------------------
        i = imax(blk) - 1
         lamda_max = 0.0d0
         lamda_min = 1.0d9
           Do m = -2, 1
            If (lamda(i+m,j,k) .GE. lamda_max) lamda_max=lamda(i+m,j,k)
            If (lamda(i+m,j,k) .LE. lamda_min) lamda_min=lamda(i+m,j,k)
           End do
         lamda_all_plus(i,j,k)=lamda_max-lamda_min
C-----------------------------------------------------------------------
        i = imax(blk)
         lamda_max = 0.0d0
```

```
        lamda_min = 1.0d9
          Do m = -2, 0
           If (lamda(i+m,j,k) .GE. lamda_max) lamda_max=lamda(i+m,j,k)
           If (lamda(i+m,j,k) .LE. lamda_min) lamda_min=lamda(i+m,j,k)
          End do
        lamda_all_plus(i,j,k)=lamda_max-lamda_min
C-------------------------------------------------------------------
        End do
        End do


C*****************************************************************
C     Calculate lamda stencil minus in x direction
C*****************************************************************
      Do k = kmin(blk), kmax(blk)
        Do j = jmin(blk), jmax(blk)
C-------------------------------------------------------------------
       Do i = 4, imax(blk) - 2
        lamda_max = 0.0d0
        lamda_min = 1.0d9
          Do m = -3, 2
           If (lamda(i+m,j,k) .GE. lamda_max) lamda_max=lamda(i+m,j,k)
              If (lamda(i+m,j,k) .LE. lamda_min) lamda_min=lamda(i+m,j,k)
            End do
          lamda_all_minus(i,j,k)=lamda_max-lamda_min
         End do
C-------------------------------------------------------------------
       i = 3
        lamda_max = 0.0d0
        lamda_min = 1.0d9
          Do m = -2, 2
           If (lamda(i+m,j,k) .GE. lamda_max) lamda_max=lamda(i+m,j,k)
              If (lamda(i+m,j,k) .LE. lamda_min) lamda_min=lamda(i+m,j,k)
            End do
          lamda_all_minus(i,j,k)=lamda_max-lamda_min
C-------------------------------------------------------------------
       i = 2
        lamda_max = 0.0d0
        lamda_min = 1.0d9
          Do m = -1, 2
           If (lamda(i+m,j,k) .GE. lamda_max) lamda_max=lamda(i+m,j,k)
              If (lamda(i+m,j,k) .LE. lamda_min) lamda_min=lamda(i+m,j,k)
            End do
          lamda_all_minus(i,j,k)=lamda_max-lamda_min
C-------------------------------------------------------------------
       i = 1
        lamda_max = 0.0d0
        lamda_min = 1.0d9
          Do m = 0, 2
           If (lamda(i+m,j,k) .GE. lamda_max) lamda_max=lamda(i+m,j,k)
```

```
            If (lamda(i+m,j,k) .LE. lamda_min) lamda_min=lamda(i+m,j,k)
           End do
         lamda_all_minus(i,j,k)=lamda_max-lamda_min
C-------------------------------------------------------------------
       i = imax(blk) - 1
        lamda_max = 0.0d0
        lamda_min = 1.0d9
          Do m = -3, 1
           If (lamda(i+m,j,k) .GE. lamda_max) lamda_max=lamda(i+m,j,k)
            If (lamda(i+m,j,k) .LE. lamda_min) lamda_min=lamda(i+m,j,k)
           End do
         lamda_all_minus(i,j,k)=lamda_max-lamda_min
C-------------------------------------------------------------------
       i = imax(blk)
        lamda_max = 0.0d0
        lamda_min = 1.0d9
          Do m = -3, 0
           If (lamda(i+m,j,k) .GE. lamda_max) lamda_max=lamda(i+m,j,k)
            If (lamda(i+m,j,k) .LE. lamda_min) lamda_min=lamda(i+m,j,k)
           End do
         lamda_all_minus(i,j,k)=lamda_max-lamda_min
C-------------------------------------------------------------------
     End do
     End do

C*************************************************************
C     Calculate Jacobian plus
C*************************************************************
        Do k = kmin(blk), kmax(blk)
        Do j = jmin(blk), jmax(blk)
          Do i = 1, imax(blk) - 1
           Jacobian_plus(i,j,k) = 0.5d0*(metrics(blk)%at(i+1,j,k,10)+
    &                            metrics(blk)%at(i,j,k,10))
       End do
C-------------------------------------------------------------------
       i = imax(blk)
        Jacobian_plus(i,j,k) = metrics(blk)%at(i,j,k,10)
     End do
     End do

C*************************************************************
C     Calculate Jacobian minus
C*************************************************************
        Do k = kmin(blk), kmax(blk)
        Do j = jmin(blk), jmax(blk)
          Do i = 2, imax(blk)
           Jacobian_minus(i,j,k) = 0.5d0*(metrics(blk)%at(i-1,j,k,10)+
    &                            metrics(blk)%at(i,j,k,10))
       End do
C-------------------------------------------------------------------
```

```
      i = 1
       Jacobian_minus(i,j,k) = metrics(blk)%at(i,j,k,10)
     End do
     End do

C*************************************************************
C     Calculate shock detector: niu
C*************************************************************
     Do k = kmin(blk), kmax(blk)
       Do j = jmin(blk), jmax(blk)
         Do i = 2, imax(blk) - 1
            niu(i,j,k)=Dabs(P(blk)%at(i-1,j,k)*metrics(blk)%at(i-1,j,k,11)
    &               -2.0d0*P(blk)%at(i,j,k)*metrics(blk)%at(i,j,k,11)
    &               +P(blk)%at(i+1,j,k)*metrics(blk)%at(i+1,j,k,11))
    &               /(P(blk)%at(i-1,j,k)*metrics(blk)%at(i-1,j,k,11)
    &               +2.0d0*P(blk)%at(i,j,k)*metrics(blk)%at(i,j,k,11)
    &               +P(blk)%at(i+1,j,k)*metrics(blk)%at(i+1,j,k,11))
       End do
C-------------------------------------------------------------------
      i = 1
       niu(i,j,k)=Dabs(P(blk)%at(i+1,j,k)*metrics(blk)%at(i+1,j,k,11)
    &                  -P(blk)%at(i,j,k)*metrics(blk)%at(i,j,k,11))
    &              /(3.0d0*P(blk)%at(i,j,k)*metrics(blk)%at(i,j,k,11)
    &               +P(blk)%at(i+1,j,k)*metrics(blk)%at(i+1,j,k,11))
      i = imax(blk)
       niu(i,j,k)=Dabs(P(blk)%at(i-1,j,k)*metrics(blk)%at(i-1,j,k,11)
    &                  -P(blk)%at(i,j,k)*metrics(blk)%at(i,j,k,11))
    &               /(P(blk)%at(i-1,j,k)*metrics(blk)%at(i-1,j,k,11)
    &              +3.0d0*P(blk)%at(i,j,k)*metrics(blk)%at(i,j,k,11))
     End do
     End do

C*************************************************************
C     Calculate kapa(j,k)
C*************************************************************
     Do k = kmin(blk), kmax(blk)
       Do j = jmin(blk), jmax(blk)
C-------------------------------------------------------------------
      P_max = 0.0d0
      P_min = 1.0d9
      lamda_max = 0.0d0
      lamda_min = 1.0d9
      lamda_hat_max = 0.0d0
      lamda_hat_min = 1.0d9
      Do i = imin(blk), imax(blk)
        If (P(blk)%at(i,j,k)*metrics(blk)%at(i,j,k,11).GE.P_max) then
            P_max=P(blk)%at(i,j,k)*metrics(blk)%at(i,j,k,11)
        End if
        If (P(blk)%at(i,j,k)*metrics(blk)%at(i,j,k,11).LE.P_min) then
            P_min=P(blk)%at(i,j,k)*metrics(blk)%at(i,j,k,11)
```

```
          Endif
              If (lamda(i,j,k).GE.lamda_max) lamda_max=lamda(i,j,k)
              If (lamda(i,j,k).LE.lamda_min) lamda_min=lamda(i,j,k)
              If (lamda_hat(i,j,k).GE.lamda_hat_max) Then
                 lamda_hat_max=lamda_hat(i,j,k)
              End if
              If (lamda_hat(i,j,k).LE.lamda_hat_min) Then
                 lamda_hat_min=lamda_hat(i,j,k)
              End if
         End do
            sigmma = P_max/P_min
            alffa  = lamda_max/lamda_min
        if (alffa .eq. 1) alffa = 1.00000001
            betta  = lamda_hat_max/lamda_hat_min
        if (betta .eq. 1) betta = 1.00000001
            expo   = 0.5d0*(alffa + betta)/(alffa * betta)
            alffa_hat=(alffa+1.0d0)/(alffa-1.0d0)*Dtanh(alffa-1.0d0)
            betta_hat=(betta+1.0d0)/(betta-1.0d0)*Dtanh(betta-1.0d0)
c        kapa(j,k)=5
        kapa(j,k)= (1.0d0+(sigmma-1.0d0)*Dtanh(alffa/betta-1.0d0))*
     &  (Dsqrt(alffa_hat*betta_hat))**(1.0d0+Dtanh(sigmma-1.0d0))/
     &  (sigmma**expo)


       End do
       End do

C*************************************************************
C     Calculate epsilon2_plus, epsilon4_plus
C*************************************************************
      Do k = kmin(blk), kmax(blk)
        Do j = jmin(blk), jmax(blk)
C-----------------------------------------------------------------------
        Do i = 3, imax(blk) - 3
         niu_max = 0.0d0
           Do m = -2, 3
              If (niu(i+m,j,k) .GE. niu_max) niu_max=niu(i+m,j,k)
           End do
         epsilon2_plus(i,j,k)=kapa(j,k)*niu_max
        End do
C-----------------------------------------------------------------------
        i = 2
         niu_max = 0.0d0
           Do m = -1, 3
                 If (niu(i+m,j,k) .GE. niu_max) niu_max=niu(i+m,j,k)
           End do
         epsilon2_plus(i,j,k)=kapa(j,k)*niu_max
C-----------------------------------------------------------------------
        i = 1
        niu_max = 0.0d0
```

```
          Do m = 0, 3
                If (niu(i+m,j,k) .GE. niu_max) niu_max=niu(i+m,j,k)
          End do
        epsilon2_plus(i,j,k)=kapa(j,k)*niu_max
C-------------------------------------------------------------------------
        i = imax(blk) - 2
        niu_max = 0.0d0
          Do m = -2, 2
                If (niu(i+m,j,k) .GE. niu_max) niu_max=niu(i+m,j,k)
          End do
        epsilon2_plus(i,j,k)=kapa(j,k)*niu_max
C-------------------------------------------------------------------------
       i = imax(blk) - 1
        niu_max = 0.0d0
          Do m = -2, 1
                If (niu(i+m,j,k) .GE. niu_max) niu_max=niu(i+m,j,k)
          End do
        epsilon2_plus(i,j,k)=kapa(j,k)*niu_max
C-------------------------------------------------------------------------
       i = imax(blk)
        niu_max = 0.0d0
          Do m = -2, 0
                If (niu(i+m,j,k) .GE. niu_max) niu_max=niu(i+m,j,k)
          End do
        epsilon2_plus(i,j,k)=kapa(j,k)*niu_max
C-------------------------------------------------------------------------
     End do
     End do

     Do k = kmin(blk), kmax(blk)
        Do j = jmin(blk), jmax(blk)
        Do i = imin(blk), imax(blk)
          epsilon4_plus(i,j,k)=Dmax1((kapa(j,k)-epsilon2_plus(i,j,k)), 0.0d0)
        End do
        End do
        End do

C*************************************************************
C     Calculate epsilon2_minus epsilon4_minus
C*************************************************************
     Do k = kmin(blk), kmax(blk)
        Do j = jmin(blk), jmax(blk)
C-------------------------------------------------------------------------
       Do i = 4, imax(blk) - 2
          niu_max = 0.0d0
          Do m = -3, 2
             If (niu(i+m,j,k) .GE. niu_max) niu_max=niu(i+m,j,k)
          End do
        epsilon2_minus(i,j,k)=kapa(j,k)*niu_max
       End do
```

```
C-------------------------------------------------------------------
      i = 3
         niu_max = 0.0d0
         Do m = -2, 2
            If (niu(i+m,j,k) .GE. niu_max) niu_max=niu(i+m,j,k)
         End do
       epsilon2_minus(i,j,k)=kapa(j,k)*niu_max
C-------------------------------------------------------------------
      i = 2
         niu_max = 0.0d0
         Do m = -1, 2
            If (niu(i+m,j,k) .GE. niu_max) niu_max=niu(i+m,j,k)
         End do
       epsilon2_minus(i,j,k)=kapa(j,k)*niu_max
C-------------------------------------------------------------------
      i = 1
         niu_max = 0.0d0
         Do m = 0, 2
            If (niu(i+m,j,k) .GE. niu_max) niu_max=niu(i+m,j,k)
         End do
       epsilon2_minus(i,j,k)=kapa(j,k)*niu_max
C-------------------------------------------------------------------
      i = imax(blk) - 1
         niu_max = 0.0d0
         Do m = -3, 1
            If (niu(i+m,j,k) .GE. niu_max) niu_max=niu(i+m,j,k)
         End do
       epsilon2_minus(i,j,k)=kapa(j,k)*niu_max
C-------------------------------------------------------------------
      i = imax(blk)
         niu_max = 0.0d0
         Do m = -3, 0
            If (niu(i+m,j,k) .GE. niu_max) niu_max=niu(i+m,j,k)
         End do
       epsilon2_minus(i,j,k)=kapa(j,k)*niu_max
C-------------------------------------------------------------------
     End do
     End do

     Do k = kmin(blk), kmax(blk)
       Do j = jmin(blk), jmax(blk)
       Do i = imin(blk), imax(blk)
        epsilon4_minus(i,j,k)=Dmax1((kapa(j,k)-epsilon2_minus(i,j,k)), 0.0d0)
       End do
       End do
       End do

C*************************************************************
C     Calculate artificial damping term in x direction
C*************************************************************
```

```
        Do k = kmin(blk), kmax(blk)
        Do j = jmin(blk), jmax(blk)
        Do i = imin(blk), imax(blk) !mihero
          d_plus_dx(i,j,k)=lamda_all_plus(i,j,k)*Jacobian_plus(i,j,k)*
     &      (epsilon2_plus(i,j,k)*(con_var(i+1,j,k)-con_var(i,j,k))+
     &     epsilon4_plus(i,j,k)*(b1*(con_var(i+1,j,k)-con_var(i,j,k))+
     &                    b2*(con_var(i+2,j,k)-con_var(i-1,j,k))+
     &                    b3*(con_var(i+3,j,k)-con_var(i-2,j,k))))

        d_minus_dx(i,j,k)=lamda_all_minus(i,j,k)*Jacobian_minus(i,j,k)*
     &      (epsilon2_minus(i,j,k)*(con_var(i,j,k)-con_var(i-1,j,k))+
     &     epsilon4_minus(i,j,k)*(b1*(con_var(i,j,k)-con_var(i-1,j,k))+
     &                    b2*(con_var(i+1,j,k)-con_var(i-2,j,k))+
     &                    b3*(con_var(i+2,j,k)-con_var(i-3,j,k))))
      End do

      End do
      End do
C*************************************************************
C     aritificial dissipation term addition in x direction
C*************************************************************
        DO k=1,nz(blk)
        DO j=1,ny(blk)
        DO i=1,nx(blk) !mihero
       dF_by_dT(blk)%at(i,j,k,var) =
     &  dF_by_dT(blk)%at(i,j,k,var)-d_plus_dx(i,j,k)+d_minus_dx(i,j,k)

        END DO
        END DO
        END DO



      End subroutine dissipation_dx
```

Bibliography

[1] Busquin, M, A., "European Aeronautics: A Vision for 2020, Meeting Society's Needs and Winning Global Leadership," Rept. Of the Group of Personalities, KI-34-01-827-EN-C, Advisory Council for Aeronautics Research in Europe, Office for Official Publications of the European Communities, Luxembourg, Jan. 2001.

[2] Dobrzynski, W., "Almost 40 Years of Airframe Noise Research: What Did We Achieve?" *Journal of Aircraft*, Vol. 47(2), pp. 353-367, 2010.

[3] Dobrzynski, W., Pott-Pollenske, M., Foot, D., Goodwin, M., "Landing Gears Aerodynamic Interaction Noise," European Congress on Computational Methods in Applied Sciences and Engineering (ECCOMAS), 2004.

[4] Hedges, L. S., Travin, A. K., and Spalart, P. R., "Detached-Eddy Simulations over a Simplified Landing Gear," *Journal of Fluids Engineering*, Vol. 124, pp. 413-423, 2002.

[5] Van de Ven, T., "Computational and Aeroacoustic Analysis of A ¼ Scale G550 Nose Landing Gear and Comparison to NASA & UFL Wind Tunnel Data," AIAA Paper 2009-3359, 2009.

[6] Vatsa, V., lockard, D., and Khorrami, M. R., "Application of FUN3D Solver for Aeroacoustics Simulation of a Nose Landing Gear Configuration," AIAA Paper 2011-2820, 2011.

[7] Manoha, E., Bulté, J., Ciobaca, V., and Caruelle, B., "Lagoon: further analysis of aerodynamic experiments and early aeroacoustic results," AIAA Paper 2009-3277, 2009.

[8] Ma, Z. K., "Experimental Data Base for a Single Landing Gear Wheel," CADWIE report, University of Southampton, 2007.

[9] Spalart, P., and Allmaras, S., "A One Equation Turbulence Model for Aerodynamic Flows," AIAA Paper, 92-0439, 1992.

[10] Wilcox, C. D., "Turbulence Modeling for CFD," 2nd edition, DCW Industries, 1998.

[11] Menter, F. R., "Two-Equation Eddy-Viscosity Turbulence Models for Engineering Applications," *AIAA Journal*, Vol. 32(8), pp. 1598-1605, 1994.

[12] Rizzetta, D. P., Visbal, M. R., and Blaisdell, G. A., "A time-implicit high-order compact differencing and filtering scheme for large-eddy simulation," *International Journal for Numerical Methods in Fluids*, Vol. 42, pp. 665-693, 2003.

[13] Lockard, D. P., Khorrami, M. R., and Li, F., "High Resolution Calculation of a Simplified Landing Gear," AIAA Paper 2004-2887, 2004.

[14] Spalart, P. R., Deck, S., Shur, M. L., Squires, K. D., Strelets, M. K., and Travin, A., "A New Version of Detached-Eddy Simulation, Resistant to Ambiguous Grid Densities," *Theoretical and Computational Fluid Dynamics*, Vol. 20, pp. 181-195, 2006.

[15] Lighthill, M. J., "On Sound Generated Aerodynamically," *Proceedings of the Royal Society of London*, Vol. 211, pp. 564-587, 1951.

[16] Kerebrock, J. L., "Aircraft Engines and Gas Turbines," MIT Press Ltd, 1992.

[17] Ffowcs Williams, J. E. and Hawkings, D. L., "Sound Generation by Turbulence and Surfaces in Arbitrary Motion," *Philosophical Transactions of the Royal Society of London*, Vol. 246, pp. 321-342, 1969.

[18] Curle, N., "The Influence of Solid Boundaries upon Aerodynamic Sound," *Proceedings of the Royal Society of London*, Vol. 231, pp. 505-514, 1955.

[19] Brentner, K. S., and Farassat, F., "An Analytical Comparison of the Acoustic Analogy and Kirchhoff Formulation for Moving Surfaces," *AIAA Journal*, Vol. 36, pp. 1379-1386, 1998

[20] Lockard, D. P., "A Comparison of Ffowcs Williams-Hawkings Solvers for Airframe Noise Application," AIAA Paper, 2002-2580, 2002.

[21] Brentner, K. S, "An Efficient and Robust Method for Predicting Helicopter Rotor High-Speed Impulsive Noise," *Journal of Sound and Vibration*, Vol. 203, pp. 87-100, 1997.

[22] Tam, C. K. W., "Computational Aeroacoustics: Issues and Methods," *AIAA Journal*, Vol. 33(10), pp. 1788-1796, 1995.

[23] Tam, C. K. W., "Computational Aeroacoustics: An Overview of Computational Challenges and Applications," *International Journal of Computational Fluid Dynamics*, Vol. 18(6), pp. 547-567, 2004.

[24] Singer, B. A., and Guo, Y. P., "Development of Computational Aeroacoustics Tools for Airframe Noise Calculations," *International Journal of Computational Fluid Dynamics*, Vol. 18, pp. 455-469, 2004.

[25] Singer, B. A., Lockard, D. P., and Lilley, G. M., "Hybrid Acoustic Predictions," *Computers & Mathematics with Applications*, Vol. 46(4), pp. 647-669, 2003.

[26] Bailly, C., and Juvé, D., "Numerical Solution of Acoustic Propagation Problems Using Linearized Euler Equations," *AIAA Journal*, Vol. 38(1), pp. 22-29, 2000.

[27] Ewert, R., and Schroder, W., "Acoustic Perturbation Equations Based on Flow Decomposition via Source Filtering," *Journal of Computational Physics*, Vol. 188, pp. 365-398, 2003.

[28] Ewert, R., and Schroder, W., "On the simulation of trailing edge noise with a hybrid LES/APE method," *Journal of Sound and Vibration*, Vol. 270, pp. 509-524, 2004.

[29] Farassat, F., "The Kirchhoff Formulas for Moving Surfaces in Aeroacoustics-The Subsonic and Supersonic Cases," NASA Technical Memorandum 110285, 1996.

[30] Zingg, D.W., "A Review of High-Order and Optimized Finite-Difference Methods for Simulating Linear Wave Phenomena," AIAA Paper 97-2088, 1997.

[31] Tam, C. K. W., and Webb, J. C., "Dispersion Relation Preserving Finite Difference Schemes for Computational Acoustics," *Journal of Computational Physics*, Vol. 107, pp. 262-281, 1993.

[32] Lele, S. K., "Compact finite difference schemes with spectral-like resolution," *Journal of Computational Physics*, Vol. 103, pp. 16-42, 1992.

[33] Hixon, R., "A New Class of Compact Schemes," AIAA Paper 98-0367, 1998.

[34] Hixon, R., "Prefactored small-stencil compact schemes," *Journal of Computational Physics*, Vol. 165(2), pp. 522-541, 2000.

[35] Ashcroft, G., and Zhang, X., "Optimized Prefactored Compact Schemes," *Journal of Computational Physics*, Vol. 190, pp. 459-477, 2003.

[36] J. C. Butcher, "Numerical methods for ordinary differential equations," Second edition.

[37] Hu, F. Q., Hussaini, M. Y., and Manthey, J, "Low-dissipation and -dispersion Runge-Kutta schemes for computational acoustics," *Journal of Computational Physics*, Vol. 124, pp. 177-191, 1996.

[38] Visbal, M.R. and Gaitonde, D. V., "High-Order-Accurate Methods for Complex Unsteady Subsonic Flows," *AIAA Journal*, Vol. 37(10), pp.1231-1239, 1999.

[39] Visbal, M.R. and Gaitonde, D. V., "On the Use of Higher-Order Finite-Difference Schemes on Curvilinear and Deforming Meshes," *Journal of Computational Physics*, Vol. 181, pp. 155-185, 2002.

[40] Yoon S, Jameson A. "Lower-upper symmetric-Gauss–Seidel method for the Euler and Navier–Stokes equations," AIAA Paper 87-0600, 1987.

[41] Singer, B. A., and Brentner, K. S., "Simulation of Acoustic Scattering from a Trailing Edge," *Journal of Sound and Vibration*, Vol. 230, pp. 541-560, 2000.

[42] Tam, C. K. W., "Advances in Numerical Boundary Conditions for Computational Aeroacoustics," AIAA Paper 97-1774, 1997.

[43] Thompson, K. W., "Time Dependent Boundary Conditions for Hyperbolic Systems," *Journal of Computational Physics*, Vol. 68, pp. 1-24, 1987.

[44] Thompson, K. W., "Time Dependent Boundary Conditions for Hyperbolic Systems, II," *Journal of Computational Physics*, Vol. 89, pp. 439-461, 1990.

[45] Poinsot, T. J., and Lele, S. K., "Boundary Conditions for Direct Simulations of Compressible Viscous Flows," *Journal of Computational Physics*, Vol. 101, pp. 104-129, 1992.

[46] Kim, J. W., and Lee, D. J., "Generalized Characteristic Boundary Conditions for Computational Aeroacoustics," *AIAA Journal*, Vol. 38, pp. 2040-2049, 2000.

[47] Kim, J. W., and Lee, D. J., "Generalized Characteristic Boundary Conditions for Computational Aeroacoustics, Part 2," *AIAA Journal*, Vol. 42, pp. 47-55, 2004.

[48] Bayliss, A., and Turkel, E. "Far Field Boundary Conditions for Compressible Flows," *Journal of Computational Physics*, Vol. 48, pp. 182-199, 1982.

[49] Bayliss, A., and Turkel, E. "Radiation boundary conditions for wave-like equations," *Communications on Pure and Applied Mathematics*, Vol.33, pp. 707-725, 1980.

[50] Hagstrom, T., and Hariharan, S. I., "Accurate Boundary Conditions for Exterior Problems in Gas Dynamics," *Mathematics of Computation*, Vol. 51, pp. 581-597, 1988.

[51] Higdon, R. L., "Numerical Absorbing Boundary Conditions for the Wave Equation," *Mathematics of Computation*, Vol. 49, pp. 65-90, 1987.

[52] Kosloff, R, and Kosloff, D. "Absorbing boundaries for wave propagation problems," *Journal of Computational Physics*, Vol. 63, pp. 363-376, 1986.

[53] Freund, J. B., "Proposed Inflow/Outflow Boundary Condition for Direct Computation of Aerodynamic Sound," *AIAA Journal*, Vol. 35, pp. 740-742, 1997.

[54] Farassat, F. and Casper, H. "Towards an Airframe Noise Prediction Methodology: Survey of Current Approaches," AIAA Paper 2006-0210, 2006.

[55] Cox, J. S., Brentner, K. S., and Rumsey, C. L., "Computation of Vortex Shedding and Radiated Sound for a Circular Cylinder: Subcritical to Transcritical Reynolds Numbers," *Theoretical and Computational Fluid Dynamics*, Vol. 12, pp. 233-253, 1998.

[56] Souliez, F. J., Long, L. N., Morris, P. J., and Sharma, A., "Landing Gear Aerodynamic Noise Prediction Using Unstructured Grids," *International Journal of Aeroacoustics*, Vol. 1(2), pp. 115-135, 2002.

[57] Lockard, D. P., and Casper, J. H., "Permeable Surface Corrections for Ffowcs Williams and Hawkings Integrals," AIAA Paper, 2005-2995, 2005.

[58] Heller, H., and Dobryznski, W., "Sound Radiation from Aircraft Wheel-well/Landing-gear Configurations," *Journal of Aircraft*, Vol. 8, pp. 768-774, 1977.

[59] Dobrzynski, W., Chow, L. C., Guion, P., and Shiells, D., "A European Study on Landing Gear Airframe Noise Sources," AIAA Paper 2000-1971, 2000.

[60] Chow, L., Mau, K., and Remy, H., "Landing Gears and High Lift Devices Airframe Research," AIAA Paper 2002-2408, 2002.

[61] Pott-Pollenske, M., Dobrzynski, W., Buchholz, H., Guérin, S., Saueressig, G., and Finke, U., "Airframe Noise Characteristics from Flyover Measurements and Predictions," AIAA Paper 2006-2567, 2006.

[62] Smith, M. G., Chow, L. C., Molin, N., Piet, J. F., and Carrilho, J., "Landing Gear Noise with Installation Effects," AIAA Paper 2007-3472, 2007.

[63] Guo, Y. P., "A Study on Local Flow Variations for Landing Gear Noise Research," AIAA Paper 2008-2915, 2008.

[64] Carrilho, J., and Smith, M. G., "Scattering of landing Gear Noise by a Wing," AIAA Paper 2008-2965, 2008.

[65] Dobrzynski, W., and Buchholz, H., "Full-Scale Noise Testing on Airbus Landing Gears in the German-Dutch Wind Tunnel," AIAA Paper 1997-1597, 1997.

[66] Stoker, R. W., "Landing Gear Noise Test Report," NASA Report, NAS1-97040, 1997.

[67] Ravetta, P. A., Burdisso, R. A. and Ng, W. F., "Wind Tunnel Aeroacoustic Measurements of a 26% Scale 777 Main Landing Gear Model," AIAA Paper 2004-2885, 2004.

[68] Smith, M. G., Fenech, B., Chow, L. C., Molin, N., Dobrzynski, W., and Seror, C., "Control of Noise Sources on Aircraft Landing Gear Bogies," AIAA Paper 2006-2626, 2006.

[69] Guo, Y., Yamamoto, K., and Stoker, R. W., "Experimental Study on Aircraft Landing Gear Noise," *Journal of Aircraft*, Vol. 43(2), pp. 306-317, 2006.

[70] Guo, Y., "A Semi-Empirical Model for Aircraft Landing Gear Noise Prediction," AIAA Paper 2006-2627, 2006.

[71] Manoha, E., Bulté, J., and Caruelle, B., "Lagoon: An Experimental Database for the Validation of CFD/CAA Methods for Landing Gear Noise Prediction," AIAA Paper 2008-2816, 2008.

[72] Khorrami, M., "Towards Establishing a Realistic Benchmark for Airframe Noise Research: Issues and Challenges," IUTAM Symposium on Computational Aero-Acoustics for Aircraft Noise Prediction, 2010.

[73] Neuhart, D. H., Khorrami, M. R., and Choudhari, M. M., "Aerodynamics of a Gulfstream G550 Nose Landing Gear Model," AIAA Paper 2009-3152, 2009.

[74] Zawodny, N. S., Liu, F., Yardibi, T., Cattafeta, L. N., Khorrami, M. R., Neuhart, D. H., and Van de Ven, T., "A Comparative Aeroacoustic Study of a ¼-Scale Gulfstream G550 Aircraft Nose Landing Gear Model," AIAA Paper 2009-3153, 2009.

[75] Yokokawa, Y., Imamura, T., Ura, H., Kobayashi, H., Uchida, H., and Yamamoto, K., "Experimental Study on Noise Generation of a Two-Wheel Main Landing Gear," AIAA Paper 2009-3277, 2009.

[76] Lazos, B. S., "Mean Flow Features Around the Inline Wheels of Four-Wheel Landing Gear," *AIAA Journal*, Vol. 40, pp. 193-198, 2002.

[77] Lazos, B. S., "Surface Topology of the Wheels on a Generic Four-Wheel Landing Gear," *AIAA Journal*, Vol. 40, pp. 2402-2411, 2002.

[78] Ringshia, A. K., Ng, W., and Burdisso, R. A., "Aerodynamic Measurements in a Wind Tunnel of the Scaled Models of a 777 Main Lading Gear," NASA Grant, NAG-1-02084, 2006.

[79] Fink, M. R., "Airframe Noise Prediction Method," Federal Aviation Administration RD-77-29, 1977.

[80] Smith, M. G., and Chow, L. C., "Validation of a Prediction Model for Aerodynamic Noise from Aircraft Landing Gears," AIAA Paper 2002-2581, 2002.

[81] Molin, N., Piet, J. F., Chow, L. C., Smith, M. G., Dobrzynski, W., and Seror, C., "Prediction of Low Noise Aircraft Landing Gears and Comparison with Test Results," AIAA Paper 2006-2623, 2006.

[82] Guo, Y. P., Yamamoto, K. J., and Stocker, R. W., "An Empirical Model for Landing Gear Noise Prediction," AIAA Paper 2004-2888, 2004.

[83] Burley, C. L., Brooks, T. F., Humphreys, W. M., and Rawls, J. W., "ANOPP Landing Gear Noise Prediction Comparisons to Model-Scale Data," AIAA Paper 2007-3459, 2007.

[84] Imamura, T., Hirai, T., Amemiya, K., Yokokawa, Y., Enomoto, S., and Yamamoto, K., "Aerodynamic and Aeroacoustic Simulations of a Two-wheel Landing Gear," IUTAM Symposium on Computational Aero-Acoustic for Aircraft Noise Prediction, 2009.

[85] Pointwise, http://www.pointwise.com.

[86] Dethioux, P., Bres, G., Noelting, S., Van de Ven, T., and Vieto, R., "BANC-I Partially-Dressed Cavity Closed Nose Landing Gear," BANC-I conference presentation, 2009.

[87] Ueno, Y., Ochi, A., Isotani, K., and Hayama, K., "Validation of High-order Accuracy Method using Cartesian Grid," BANC-I conference presentation, 2009.

[88] Li, F., Khorrami, M., and Malik, M., "Unsteady Simulation of Landing-Gear Flow Field," AIAA Paper 2002-2411, 2002.

[89] Lockard, D. P., Khorrami, M. R., and Li, F., "Aeroacoustic Analysis of a Simplified Landing Gear," AIAA paper, 2003-3111, 2003.

[90] Spalart, P. R., Shur, M. L., Strelets, M. K., and Travin, A. K, "Towards Noise Prediction for Rudimentary Landing Gear Model," IUTAM Symposium on Computational Aero-Acoustics for Aircraft Noise Prediction, 2010.

[91] Khorrami, M. R., and Lockard, D. P., "A Landing Gear Noise Reduction Study based on Computational Simulations," Inter-Noise Conference, 2006.

[92] Dobrzynski, W. M, Schoning, B., Chow, L. C., Wood, C., Smith, M., and Seror, C., "Design and Testing of Low Noise Landing Gears," *International Journal of Aeroacoustics*, Vol. 5(3), pp. 233-262, 2006.

[93] CENTAURSOFT, http://www.centaursoft.com, 2010.

[94] Dobrzynski, W., Chow, L. C., Guion, P., and Shiells, D., "Research into Landing Gear Airframe Noise Reduction," AIAA Paper 2002-2409, 2002.

[95] Remillieux, M. C., Camargo, H. E., Ravetta, P. A., Burdisso, R. A., and Ng, W. F., "Noise Reduction of a Model-Scale Landing Gear Measured in the Virginia Tech Aeroacoustic Wind Tunnel," AIAA Paper 2008-2818, 2008.

[96] Ravetta, P. A., Burdisso, R. A., and Ng, W. F., "Noise Control of Landing Gears Using Elastic Membrane-Based Fairings," AIAA Paper 2007-3466, 2007.

[97] Boorsma, K., Zhang, X., and Molin, N., "Perforated Fairings for Landing Gear Noise," AIAA Paper 008-2961, 2008.

[98] Spiteri, M., Zhang, X., Molin, N., and Chow, L. C., "The Use of a Fairing and Split Plate for Bluff Body Noise Control," AIAA Paper 2008-2817, 2008.

[99] Kopiev, V. F., Zaitsev, M. Y., and Ostrikov, N. N., "New Noise Source Mechanism of Flow/Surface Interaction as Applied to Airframe Noise Reduction," AIAA Paper 2006-2717, 2006.

[100] Thomas, F. O., Kozlov, A., and Corke, T. C., "Plasma Actuators for Landing Gear Noise Reduction," AIAA Paper 2005-3010, 2005.

[101] Huang, X., Zhang, X., and Gabriel, S., "Bluff Body Noise and Flow Control with Atmospheric Plasma Actuators," AIAA Paper 2008-3044, 2008.

[102] Jameson, A., "Time Dependent Calculations using Multigrid with Applications to Unsteady Flows Past Airfoils and Wings," AIAA Paper 91-1956, 1991.

[103] Ma, Z. K., Zhang, X., Smith, M. G., Molin, N., and Chow, L. C., "Broadband Slat Noise Attenuation Potential with Acoustic Liner Treatment," AIAA Paper 2008-2964, 2008.

[104] Kim, J. W., and Lee, D. J., "Characteristic Interface Conditions for Multiblock High-Order Computation on Singular Structured Grid," *AIAA Journal*, Vol. 41, pp. 2341-2348, 2003.

[105] Piomelli, U., and Chasnov, J. R., "Large-Eddy Simulations: Theory and Applications," Transition and Turbulence Modeling, 1996.

[106] Tecplot, http://www.tecplot.com.

[107] Kim, J. K., and Lee, D. J., "Optimized compact finite difference schemes with maximum resolution," *AIAA Journal*, Vol. 34, pp. 887-893, 1996.

[108] Hixon, R., and Turkel, E., "High-accuracy compact MacCormack-type schemes for computational aeroacoustics," NASA CR, 1998.

[109] Li, J., Li, F. and E, Q., "A Fully Implicit Method for Steady and Unsteady Viscous Flow Simulations," *International Journal for Numerical Methods in Fluids*, Vol. 43, pp. 147-163, 2003.

[110] Visbal, M.R., and Rizzetta, D.P., "Large-Eddy Simulation on Curvilinear Grids using Compact Differencing and Filtering Schemes," *Journal of Fluids Engineering*, Vol. 124(4), pp. 836-847, 2003.

[111] Hixon, R., "Prefactored Compact Filters for Computational Aeroacoustics," AIAA Paper 99-0358, 1999.

[112] Tam, C. K. W., Webb, J. C., and Dong, Z., "A Study of the Short Wave Components in Computational Acoustics," *Journal of Computational Acoustics*, Vol. 1(1), pp. 1-30, 1993.

[113] Kim, J. W., and Lee, D. J., "Adaptive Nonlinear Artificial Dissipation Model for Computational Aeroacoustics," *AIAA Journal*, Vol. 39(5), pp. 810-818, 2001.

[114] Jameson, A., Schmidt, W., and Turkel, E., "Numerical Simulation of the Euler Equations by Finite Volume Methods Using Runge-Kutta Time Stepping Schemes," AIAA Paper 81-1259, 1981.

[115] Lyrintzis, S. A. "Review: The Use of Kirchhoff's Method in Computational Aeroacoustics," *Journal of Fluid Engineering*, Vol. 116, pp. 665-676, 1994.

[116] Farassat, F. "Theory of noise generation from moving bodies with an application to helicopter rotors," NASA TR R451, 1975.

[117] Brentner, K. S. "Prediction of Helicopter Discrete Frequency Rotor Noise - A Computer Program Incorporating Realistic Blade Motions and Advanced Acoustic Formulation," NASA TM 87721, 1986.

[118] Oppenheim, A. V., and Schafer, R. W., "Discrete-Time Signal Processing," Prentice-Hall, 1989.

[119] ONERA, "Acoustic Tests in CEPRA19 Description of Measurements," LAGOON Deliverable R11, 2010.

[120] FLUENT, http://www.ansys.com.